Computational Investigations into the Structure and Reactivity of Small Transition Metal Clusters

by

Matthew Addicoat

B.Sc(Hons),
University of Adelaide, 2003

Thesis submitted for the degree of

Doctor of Philosophy

in

Chemistry
University of Adelaide

2009

Chapter 1

Reactivity of TM Trimers with Carbon Monoxide: M_3CO

DENSITY functional calculations were performed to determine equilibrium geometric structures, transition states and relative energies for M_3 clusters (M = Nb, Mo, Tc, Ru, Rh, Pd, Ag) reacting with CO, leading to proposed reaction pathways. For the Nb_3, Mo_3 and Tc_3 clusters, the lowest energy structure correlates to dissociated CO, with the C and O atoms bound on opposite sides of the metal triangle. For all other trimers, the lowest energy structures maintain the CO moiety. In the case of Pd_3 and Ag_3 the dissociated geometries lie higher in energy than the sum of the separated reactants. In most cases, several multiplicities were found to be similar in energy and minimum energy crossing points were identified for Mo_3CO, Rh_3CO and Pd_3CO. The electron density of pertinent M_3CO species was investigated using Natural Bond Order calculations. It was found that the effect of the metal trimer on the energy of the pure p-type π* anti-bonding orbital of carbon monoxide directly correlates with the occurrence of CO dissociation.

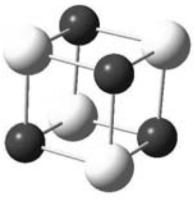

1.1 Introduction

The observation of both molecular and dissociative adsorption on transition metal clusters has led cluster scientists to adopt the double-well model as a generic description of the potential energy profile of reaction paths followed on these surfaces [18]. The presence of two potential energy wells, representing the molecular and dissociative analogues of adsorbates, an energy barrier to dissociation, and a reaction path between the molecular and dissociated states, seems to contain the essence of the chemistry observed in many cluster-molecule systems. The model has the advantage that it can be directly compared with transition-metal surface data where double-well models are also used frequently [52, 53].

The well-established sensitivity of the C-O stretching frequency to the nature of transition metal surfaces has made CO an attractive probe molecule. In cluster science, most CO-related work has involved reactivity studies. In this regard, CO has been ineffective as a probe with reaction rates showing little sensitivity to cluster structure or temperature. In the Co_n, Nb_n, Co_n^- , Pt_n^-, Cu_n^-, Au_n^-, Ag_n^-, Nb_n^- , Ni_n^-, and Pd_n^-, -CO systems examined, reaction rates are found to have a near-monotonic dependence on cluster size and seemingly little dependence on cluster electronic and geometric structure [54–60]. One exception may be Au_n [61]. Since dissociative adsorption processes are considered to be extremely sensitive to cluster electronic and geometric structure, the lack of structure-sensitivity for CO has been thought to reflect a near-barrierless molecular adsorption process. For Rh_n-CO, this is certainly the case; recent IR-depletion experiments on the Rh_n^+-CO, Rh_n-CO, and Rh_n^--CO systems establish the presence of molecularly-bound CO [62, 63]. Here, the CO is found to bind predominantly in a μ^1 (atop) mode with μ^2 (bridge) bound and μ^3 (hollow-site) bound CO observable only in select cases. Moreover, near monotonic trends in CO stretching frequencies, as a function of the number of constituent atoms in the cluster, are observed, characteristic of a structure-insensitive adsorption process. No evidence of dissociatively-bound CO was found. Spectra of Au_nCO_m clusters also establish the presence of molecularly-bound CO with a C-O stretching frequency that increases smoothly as cluster size increases [64]. The reactivity studies and the IR-depletion data therefore form a self-consistent picture. On late transition metal clusters, CO is molecularly adsorbed via a barrierless adsorption process. There is no evidence of dissociative adsorption suggesting that, in the context of a double-well model, the height of the potential energy barrier to dissociation is substantial or that dissociative adsorption is endothermic, in which case the potential energy well associated with the dissociated species lies higher in energy than the energy of the cluster + CO reagents.

However, formation of dissociatively-bound CO is thought to be the dominant adsorption process for CO on early transition metals [65]. The strength of metal-oxygen (hence the ubiquitous presence of metal-oxide species in mass spectra of clusters of early transition metals) and metal-carbon bonds [66], all establish the formation of transition metal oxides and carbides as a thermodynamically favoured processes. The bond strengths of the diatomics Nb-O and Nb-C, for example, are 7.53 and 5.39 eV, respectively [67, 68]. By comparison the bond strength of C-O is $\approx$11 eV, suggesting that dissociative adsorption of CO on Nb clusters is exothermic. Despite the generally accepted likelihood of dissociative adsorption of CO on clusters of early transition metals, there is little supporting evidence. Nb_n clusters are known to abstract O from CO_2 at room temperature [69]. Insertion into the C-O bond has been observed in reactions between Nb and Nb^+ atoms and CO2 [70, 71]. Extensive fragmentation observed when Nb_n clusters react with CO has been suggested to reflect highly exothermic adsorption processes consistent with the occurrence of dissociative adsorption of CO [60]. Nb_3CO has been intensely scrutinized with photoionization, IR-depletion, and DFT methods and the cumulative data indicate that CO is dissociatively adsorbed in the complex [72].

Overall, the experimental metal cluster + CO reactivity data can be divided into two camps: systems where CO is dissociatively adsorbed and those with molecularly adsorbed CO. To date, the computational studies lag the experiments. Although there are several studies involving niobium, rhodium and palladium clusters, many have not allowed cluster geometry to relax

[73] or have only considered one metal atom [74]. Salahub et al. undertook a comparative study of carbon monoxide binding on rhodium and palladium tetramers [75] but fixed the bond lengths of their tetramers to the interatomic distances of the bulk metal. Mineva et al. [76] undertook the first relaxed study on Rh_nCO_m (n=1-4, m=1,2) and for Rh_3CO they discovered nearly degenerate doublet, quartet and sextet states of a μ^1 geometry. Mavridis *et al.* [77] calculated the binding of CO to four $3d$ transition metal atoms, Sc, Ti, V and Cr using a coupled cluster approach and attribute the bonding to conjugation effects between the M and CO π electrons accompanied by weak σ transfer from the CO to M.

In the present study, we use DFT to explore the potential energy surfaces of the M_3 + CO reaction, for a series of $4d$ transition metal trimers from Nb_3 to Ag_3. In particular, we focus on the relative energies of associative and dissociative structures and the reaction barriers separating them using no constraints on geometry. All possible interactions are explored; associative binding (atop, bridging, side-on, planar) and dissociative binding were considered and relative energies of stable structures are presented. Reaction pathways are proposed based upon Intrinsic Reaction Coordinate calculations.

1.2 Computational Method

Density functional calculations were carried out using the Gaussian03 [78] suite of programs, employing the B3P86 hybrid exchange-correlation functional. All atoms were described using the Stuttgart/Dresden (SDD) basis set.

Geometry optimisations and frequency calculations were undertaken for the lowest four multiplicities for each metal cluster, M_3. In some cases, such as Tc_3 and Ru_3 systems, further investigations were made at higher multiplicities. Spin multiplicity is ill-defined within DFT as the Kohn-Sham orbitals represent non-interacting particles, therefore the Slater determinant generated from these orbitals is not a true many-electron wavefunction, therefore there is no function on which the spin operator (S^2) can operate. In practice it is routine to calculate a density corresponding to a doublet, triplet etc. Results are presented using the expectation value of S^2 to indicate multiplicity, however these values are not intended to indicate a true expectation value and are not quoted.

All calculations were undertaken without restraint on geometric parameters i.e. no symmetry constraints were imposed. Vibrational frequencies of the optimised structures were computed to confirm whether they were transition states or minima. The transition states linking minima were initially located using quasi-synchronous transit (QST) calculations and confirmed by IRC, from which we were able to connect key parts of the potential energy surface. To gain insight into the bonding interactions between the metal trimers and the CO unit, Natural Bond (Order) analyses were also computed.

The structure of carbon monoxide was optimised by the same method and basis set, yielding an absolute energy of -113.5163078 hartree. The optimised bond length is 1.164Å, which yields an harmonic vibrational frequency of 2046 cm^{-1} (cf. the experimental value of 2169.8 cm^{-1} [79]).

Structures consisting of the metal trimer and carbon monoxide were calculated at multiple starting geometries including end-on, side-on, planar and dissociative CO structures. Structures that did not maintain a metal trimer unit were disregarded. To distinguish different associative binding sites on the metal trimer, the Greek letter μ is used with M_3-CO to describe structures where the CO is associatively bound to either one (μ^1), two (μ^2) or three metal atoms (μ^3).

Geometries where the carbon monoxide unit bound to the trimer by the oxygen atom were also sought but only one such stationery point of this type was found for Ag_3-OC, which is a weakly bound ($\approx$0.2 eV) local minimum structure.

The *zero energy* for each cluster is defined as the sum of the energies of the metal trimer and carbon monoxide. Thus structures with an energy below the zero energy are more stable than the separated reactants; structures that have energy higher than the zero energy are unstable with respect to the infinitely separated reactants. Basis Set Superposition Error (BSSE) was determined to be minimal and was disregarded in all calculations.

The Minimum Energy Crossing Point (MECP) calculations for the $Mo_3 + CO$, $Rh_3 + CO$ and $Pd_3 + CO$ surfaces were performed using the program of Harvey [80].

In all figures, metal atoms are shaded pale, carbon atoms are represented by a middle shade and oxygen atoms are dark shaded. A bond is drawn between two atoms when the distance between them is less than the sum of their covalent radii.

1.3 Results and Discussion

The energies of the stable structures for each second row transition metal trimer are presented in Tables 1.1-1.7. For each M_3 and M_3-CO cluster, at least four multiplicities were considered although only the lowest energy structures are presented here. The bulk of the results will be discussed in three sections, firstly those metals for which dissociation of carbon monoxide is thermodynamically favourable (Nb_3, Mo_3 and Tc_3), secondly those metals for which an associative structure is the global minimum (Ru_3 and Rh_3), and finally, those metals where dissociation of carbon monoxide is not thermodynamically favourable i.e. the dissociated geometry lies higher in energy than the zero energy (Pd_3 and Ag_3).

1.3.1 Niobium, Molybdenum and Technetium

The electronic configuration of the niobium atom is $4d^4 5s^1$, thus, Nb_3 is an odd-electron species and we consider doublet, quartet, sextet and octet multiplicities. The minimum energy geometry for Nb_3 was found to be a doublet scalene triangle with bond lengths of 2.457Å, 2.390Å and 2.291Å. No C_{2v} minima were found although two transition states were identified. This is in contrast to earlier DFT calculations of Salahub *et al.* [81] and Grönbeck *et al.* [82] who both predict a doublet C_{2v} structure to be the minimum. Fowler *et al.* report a doublet ground state but differs from the previous predictions by having a geometry with two short sides and one long [83]. This is further contrasted with Raman spectra obtained by Lombardi *et al.* which suggest a D_{3h} ground state [84].

For Nb_3CO, numerous starting geometries yielded several stable minima and transition states which are shown in Figure 1.1. Energies of these structures are tabulated in Table 1.1. We have presented part of this work previously in conjunction with experimental work [72] where we used the Lanl2dz basis set. As before, the doublet state is the lowest in energy for all structures shown with higher multiplicities (quartet, sextet and octet) lying significantly higher in energy. Figure 1.1 shows that both associative (**1** and **2**) and dissociative (**3**) minima, with the latter being lowest in energy. These are linked by two transition states (**4** and **5**). The key result presented here is that although the associative structure is strongly bound by 2.55 eV, the dissociative structure is a further 1.96 eV lower in energy. The dissociative fate of the CO shown in Figure 1.1 is completely compatible with the experimental data [72]. The study of Grönbeck *et al.* also examined Nb_3CO and they found two minima corresponding to atop (μ^1) and three-fold hollow (μ^3) binding, with the latter being more energetically favourable.

	$S = \frac{1}{2}$	
Nb_3	-171.6135536	
Nb_3 + CO	-285.1304548	
1	-285.2241614	-2.55
4	-285.2169652	-2.35
2	-285.2193049	-2.42
5	-285.2090726	-2.14
3	-285.2962505	-4.51

Table 1.1: Absolute energies (in hartree) and relative energies (in eV) of the doublet multiplicity for the Nb_3 and Nb_3-CO complex structures.

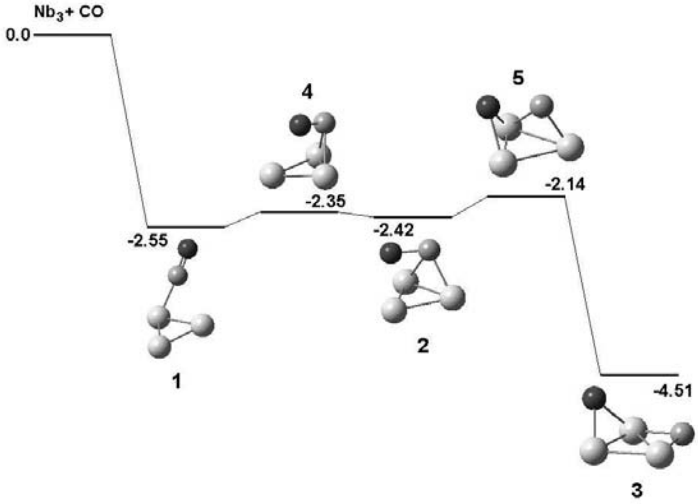

Figure 1.1: Stationary points on the Nb_3 + CO potential energy surface for the doublet multiplicity. Relative energies are given in eV.

However, no structures corresponding to dissociated CO were reported.

The Mo_3 cluster is an even-electron species and we consider singlet, triplet, quintet and septet multiplicities. For Mo_3, we find the lowest energy isomer to be a triplet with C_{2v} symmetry. This is slightly different to that found by Diez *et al.* [85], who only calculated a D_{3h} constrained (equilateral) triangle. Experimentally, Lombardi *et al.* have observed the resonance Raman spectrum of Mo_3 and find it to be consistent with a C_{2v} structure [86].

For the reaction with CO, similar structures to the Nb_3-CO system were found on the singlet and triplet surfaces: associative minima (**6** and **7**), a dissociative minimum (**8**) and transition

	$S = 0$		$S = 1$	
Mo_3	-205.3759151		-205.3993063	
Mo_3 + CO	-318.8928163		-318.9162075	
6	-318.9796842	-2.364	-319.0041196	-2.392
9	-318.9109036	-0.492	-318.9388563	-0.616
7	-318.9155427	-0.618	-318.9411873	-0.680
10	-318.9150446	-0.605	-318.9366859	-0.557
8	-319.0465778	-4.184	-319.0344684	-3.218
MECP	-319.0218	-3.51		

Table 1.2: Absolute energies (in hartree) and relative energies (in eV) of various multiplicities for the Mo_3 and Mo_3-CO complex structures. The relative energies are reported with respect to the zero energy for that multiplicity. Also shown is the energy calculated for the MECP structure, relative to the zero energy of the singlet.

states (**9** and **10**) are presented in Figure 1.2. The quintet and septet states lay much higher in energy. As seen in Figure 1.2, the triple state is ≈0.7 eV lower in energy for all structures except the global minimum (**8**), where the singlet state drops below the triplet state to -4.18 eV. This means that at some point on the surface, the spin states cross-over each other. In order to investigate this further we have performed minimum energy crossing point (MECP) calculations, the energy for which is listed in Table 1.2. The MECP calculation shows that these two surfaces cross-over at a geometry quite close to the global minimum with energy -3.51 eV (i.e. 0.67 eV above the global minimum). For both the singlet and triplet states, the relative energies of the associative structure (**6**) and the final product (**8**) are quite similar to the Nb_3-CO system. However, the energy of the first transition state (**9**) and the intermediate minimum (**7**) are relatively higher in energy by ≈1.5 eV. Looked at from another perspective, they are only ≈0.5 lower than zero energy. This is quite different to the reaction pathway for the Nb_3 + CO system where it is the second transition state that indicates the ”barrier” to dissociation.

The Tc_3 cluster is an odd-electron species and we initially considered the doublet, quartet, sextet, and octet multiplicities. Finding these to be similar in energy we extended our calculations to include the decet and dodecet multiplicities. The dodecet energies were found to be significantly higher and are not considered further. The lowest energy structure for Tc_3 is a

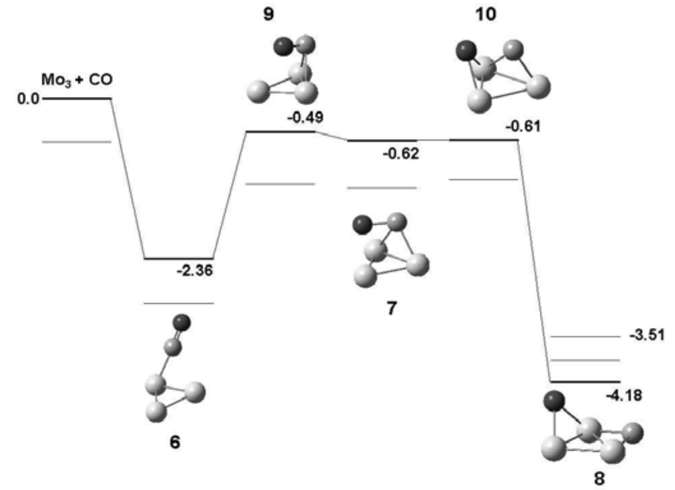

Figure 1.2: Stationary points on the Mo_3 + CO potential energy surface for the multiplicities discussed in the text. The bold lines represent the singlet state and the fine lines represent the triplet state. The dashed line above structure 8 represents the energy where the singlet and triplet surfaces cross. Reported energies are relative to the zero energy of the singlet state and are given in eV.

sextet state with C_{2v} symmetry (obtuse triangle), whilst the quartet state lies only 0.025 eV higher in energy and the other multiplicities lie clustered together ≈0.35 eV higher in energy. No previous studies have been reported for this species.

For the Tc_3-CO system, we find similar minima and transition states for each of the five multiplicities which are all relatively close in energy as shown in Figure 1.3. Table 1.3 shows that there are μ^1 (**11**) and μ^2 (**12**) associative structures that are 2.3-3.1 eV and 1.9-3.0 eV, respectively, lower than their corresponding zero energies. However, the global minimum is the sextet dissociative structure with a relative energy of -3.1 eV. A notable difference to the Nb_3-CO and Mo_3-CO systems is that the μ^2 associative structure (**12**) has the CO group oriented perpendicular to, rather than parallel with, the Tc_3 face. Furthermore, the energy of this geometry is similar to that of the μ^1 structure (**11**).

	$S = \frac{1}{2}$	$S = \frac{3}{2}$	$S = \frac{5}{2}$	$S = \frac{7}{2}$	$S = \frac{9}{2}$
Tc_3	-243.293876	-243.307625	-243.308539	-243.295771	-243.295693
Tc_3 + CO	-356.810777	-356.824526	-356.825440	-356.812672	-356.812594
11	-356.928113	-356.909237	-356.918072	-356.925691	-356.922434
14	-356.895531	-356.901955	-356.907829	-356.901157	-356.895026
12	-356.898923	-356.894144	-356.903979	-356.913587	-356.922434
15	-356.845078	-356.825275	-356.838846	-356.842441	-356.838839
13	-356.937047	-356.938811	-356.940559	-356.919335	-356.896758
11	-3.19	-2.31	-2.52	-3.08	-2.99
14	-2.31	-2.11	-2.24	-2.41	-2.24
12	-2.40	-1.89	-2.41	-2.75	-2.99
15	-0.93	-0.02	-0.36	-0.81	-0.71
13	-3.44	-3.11	-3.13	-2.90	-2.29

Table 1.3: Absolute energies (in hartree) and relative energies (in eV) of various multiplicities for the Tc_3 and Tc_3-CO complex structures. The relative energies are reported with respect to the zero energy for that multiplicity.

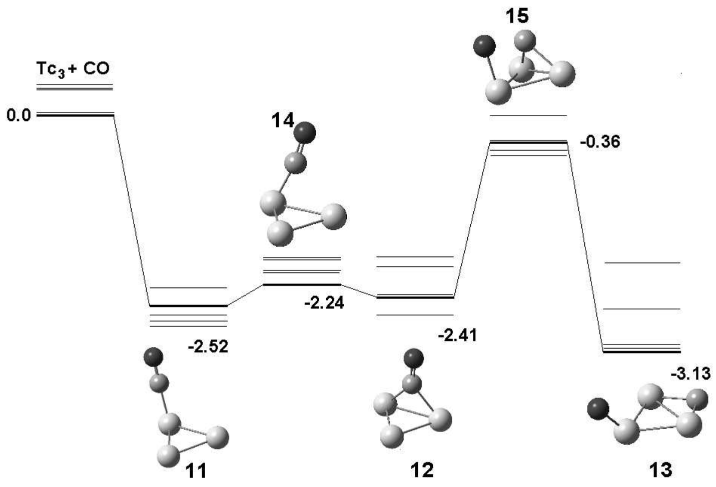

Figure 1.3: Stationary points on the Tc_3 + CO potential energy surface for the energetically competitive multiplicities. The bold lines represent the sextet state and the fine lines represent all other multiplicities. Reported energies are relative to the zero energy of the sextet state and are given in eV.

1.3.2 Ruthenium and Rhodium

The Ru_3 cluster has an even number of electrons and thus we consider singlet, triplet, quintet, septet, nonet and undecet multiplicities. We find the septet and nonet multiplicities to be the lowest energy (listed in Table 1.4) with other multiplicities being much higher. The Ru_3 minimum is a nonet with D_{3h} symmetry. Balasubramanian and Guo [87] investigated this species at DFT, CASSCF and MRCI levels of theory. Their DFT results are similar to ours in that they find the lowest energy structure to be a nonet with D_{3h} symmetry. However, their MRCI calculations show the lowest state to be an undecet obtuse triangle with a nonet state 0.53 eV higher in energy. Again, Lombardi *et al.* have presented experimental Raman data [88] but were unable to infer molecular geometry from it.

For the Ru_3CO system, we again find the septet and nonet to be the only competitive multiplicities, for which the energies and structures are shown in Table 1.4 and Figure 1.4, respectively. Now we find that there are three different associative structures: μ^1 (**16**), μ^2 (**17**) and μ^3 (**18**). For the lower energy septet surface, these three minima all have energies 2.3-2.7 eV below the zero energy. There are two relatively low-energy transition states, **19** and **20**, that link these structures. The dissociative structure (**21**) now lies higher in energy than the associative structures, although it is still below zero energy at -1.51 eV. We have not found a transition state that connects to this structure. The nonet surface essentially has the same features as the septet and highlights the same key result - that the global minimum structure involves an associatively bound CO, which is in contrast to that found for the Nb_3CO, Mo_3CO and Tc_3CO surfaces.

For Rh_3 we considered doublet, quartet, sextet and octet multiplicities and we find the lowest energy structure to be a sextet with D_{3h} symmetry (see Table 1.5). The doublet and quartet states were found to be only slightly higher in energy; 0.11 and 0.28 eV, respectively and the octet was much higher in energy. Previous MRCI calculations by Balasubramanian on both

	$S = 3$		$S = 4$	
Ru_3	-285.7036967		-285.7165033	
Ru_3 + CO	-399.2205979		-399.2334045	
16	-399.3196537	-2.70	-399.3104123	-2.10
19	-399.3021966	-2.22	-399.3053172	-1.96
17	-399.3159881	-2.60	-399.3069913	-2.00
20	-399.3034328	-2.25	-399.2857784	-4.43
18	-399.3046521	-2.29	-399.2858340	-1.43
21	-399.2761398	-1.51	-399.2703694	-1.01

Table 1.4: Absolute energies (in hartree) and relative energies (in eV) of various multiplicities for the Ru_3 and Ru_3-CO complex structures. The relative energies are reported with respect to the zero energy for that multiplicity.

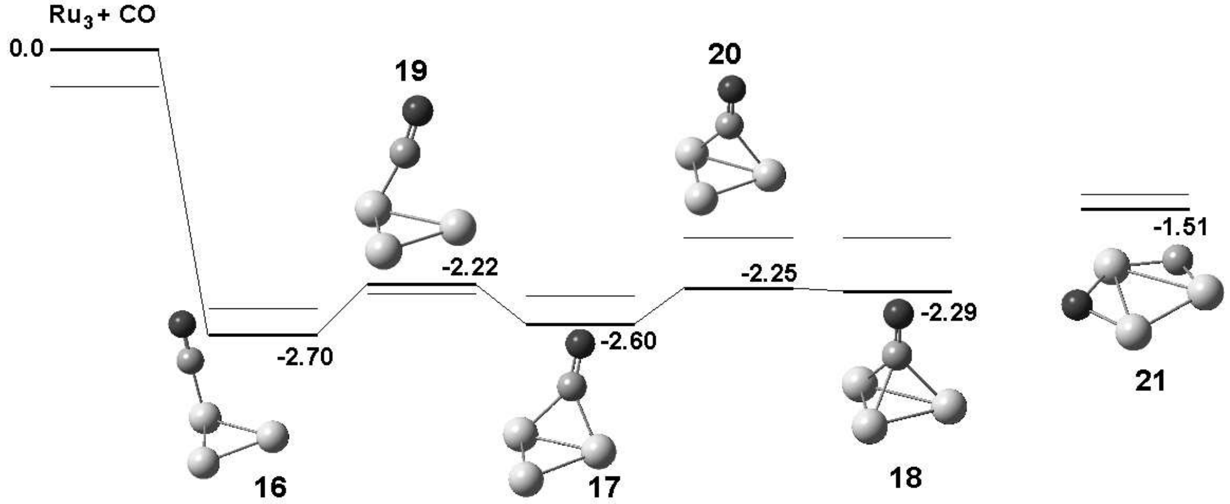

Figure 1.4: Stationary points on the Ru_3 + CO potential energy surface for the energetically competitive multiplicities. The bold lines represent the septet state and the fine lines represent the nonet state. Reported energies are relative to the zero energy of the septet state and are given in eV.

the low spin [20] and high spin [89] states of the rhodium trimer indicate that the lowest state is a sextet but that the geometry deviates substantially from D_{3h}. They do report, however, several other sextet states within 0.02 - 0.08 eV and suggest that these geometries are Jahn-Teller distorted geometries that together comprise the D_{3h} state. ESR experiments completed by Van Zee *et al.* [90] indicate a D_{3h} structure that is either a quartet or sextet.

	$S = \frac{1}{2}$		$S = \frac{3}{2}$		$S = \frac{5}{2}$	
Rh_3	-332.7962052		-332.7897758		-332.8001691	
Rh_3 + CO	-446.3131064		-446.3066770		-446.3170703	
22	-446.3964705	-2.27	-446.4052398	-2.68	-446.4051190	-2.40
25	-446.3962819	-2.26	-446.4052191	-2.68	-446.3955213	-2.13
23	-446.4239999	-3.02	-446.4289551	-3.33	-446.3976765	-2.19
26			-446.4248204	-3.21	-446.3810208	-1.74
24			-446.4279447	-3.30		
27	-446.3597954	-1.27	-446.3561855	-1.35	-446.3477488	-0.83
MECP						
Doublet-Quartet			-446.4233	-3.17		
Doublet-Sextet			-446.3964	-2.44		
Quartet-Sextet			-446.4032	-2.63		

Table 1.5: Absolute energies (in hartree) and relative energies (in eV) of various multiplicities for the Rh_3 and Rh_3-CO complex structures. The relative energies are reported with respect to the zero energy for that multiplicity. Also shown are the energies calculated for the MECP structures, relative to the zero energy of the quartet.

Optimisation of Rh_3CO yielded several minima and transition states for doublet, quartet and sextet multiplicities, which are represented in Figure 1.5. Octet states were investigated but were all found to be significantly higher in energy and not considered further. Overall, the lowest energy structure was found to be a quartet species and we will begin discussion for this surface. Three minima corresponding to μ^1 (**22**), μ^2 (**23**) and μ^3 (**24**) structures have relative energies of -2.68, -3.33 and -3.30 eV, respectively. Two transition states (**25** and **26**) were found that link the three minima. A minimum with a dissociated CO group (**27**) is much higher but still negative with respect to zero energy, -1.35 eV.

The doublet surface has the next lowest energy structure, although only μ^1 and μ^2 geometries were identified, with energies of -2.27 and -3.02 eV, respectively (relative to the zero energy of the doublet state). A dissociative state was found, again much higher in energy. The sextet surface was also found to contain μ^1 and μ^2 structures with energies -2.40 and -2.19 eV relative to zero energy (of the sextet state).

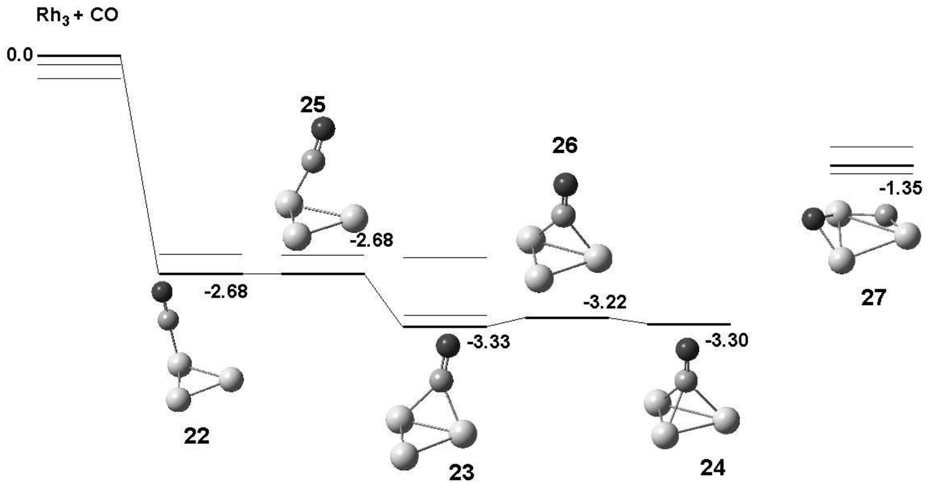

Figure 1.5: Stationary points on the Rh_3 + CO potential energy surface for the energetically competitive multiplicities. The bold lines represent the quartet state and the fine lines represent the doublet and sextet states. Reported energies are relative to the zero energy of the quartet state and are given in eV.

What is interesting here is that for Rh_3, the energy ordering of the spin states ($2S+1$) is $6 < 2 < 4$ yet for the lowest energy μ^2 structure it is $4 < 2 < 6$. This means that at some point on each surface, each spin state must cross over the others. The energies of the MECPs for the quartet-doublet, sextet-quartet and sextet-doublet surfaces are listed in Table 1.5. The crossing point for the sextet-quartet and sextet-doublet surfaces are both μ^1 structures (both are very similar to **22**) and lie 0.70 eV and 0.89 eV, respectively, above the global minimum. However, they are only 0.05 and 0.24 eV higher in energy relative to the sextet-μ^1 minimum, where the small value of the former number reflects the fact that the energies of the sextet and quartet μ^1 structures are essentially identical. Given the similarity of the energies of the quartet and sextet μ^1 structures, it seems surprising that there is no crossing point found for the quartet-doublet surface with μ^1 geometry. Indeed, we find the MECP for the quartet-doublet crossing to have a μ^2 structure, which is structurally quite similar to the minimum for the doublet-μ^2 and quartet-μ^2 states (**23**). This cross-over energy is only 0.16 eV above the global minimum.

Owing to the industrial importance of rhodium, particularly as a catalyst for hydrogenation reactions, the reaction between rhodium clusters and carbon monoxide has been previously studied by several groups. A DFT study by Salahub *et al.* in 1992 on rhodium dimers and tetramers, investigated the site selection of carbon monoxide [91]. Balasubramanian *et al.* undertook a multireference study on $Rh_3 + CO$ [73] but both these studies used constrained geometries. In particular, the Balasubramanian study constrained their μ^1 geometry to be planar. This latter study predicts the lowest energy states of μ^1 and μ^2 geometries to be quartets but finds the global minimum to be a doublet μ^3 structure. A more recent DFT study undertaken by Mineva [76] predicts a quartet μ^2 structure to be the global minimum, similar to our work. Recent experimental work on Rh_n-CO clusters using IR free electron lasers [92] have shown the presence in molecular beam expansions of only μ^3 structures for cationic and neutral Rh_4-CO, whereas the anionic system has a μ^1 structure. For Rh_3CO, only the cation was studied and the results are consistent with a μ^2 structure. Based upon these computational and experimental results, it is clear that rhodium cluster-CO complexes possess a variety of near-degenerate states of differing multiplicities and structures.

1.3.3 Palladium and Silver

We have investigated singlet, triplet, quintet and septet states of Pd_3. Photoelectron spectroscopy undertaken by Ervin et al. revealed some sixteen low lying electronic states [93]. Balasubramanian reports an energy separation between the lowest energy singlet and lowest energy triplet of 0.28 eV, favouring the singlet [94]. More recent DFT calculations by Seminario et al. report either the singlet [95] or the triplet [96] to be the ground state. Our calculations predict a C_{2v} triplet state that is 0.17 eV lower in energy than a D_{3h} singlet state.

Optimisation of Pd_3CO yielded four minima and two transition states on the triplet surface, the energies of which are listed in Table 1.6. Figure 1.6 shows three minima that correspond

	$S=0$		$S=1$	
Pd_3	-384.9636970	-384.9699756		
Pd_3 + CO	-498.4805982	-498.4868768		
28	-498.5603527	-2.17	-498.5622836	-2.05
31			-498.5574971	-1.92
29			-498.5659250	-2.15
32			-498.5541355	-1.83
30	-498.6165348	-3.70	-498.5565679	-1.90
33	-498.4512131	0.80	-498.4504638	1.00
MECP				
34			-498.55548	-1.87

Table 1.6: Absolute energies (in hartree) and relative energies (in eV) of various multiplicities for the Pd_3 and Pd_3-CO complex structures. The relative energies are reported with respect to the zero energy for that multiplicity. Also shown is the energy calculated for the MECP structure, relative to the zero energy of the triplet.

to μ^1 (**28**), μ^2 (**29**) and μ^3 (**30**) geometries. All three structures are quite similar in energy although **29** has the greatest binding energy at -2.15 eV. The transition state **31** links the μ^1 and μ^2 minima (**28** and **29**) and the μ^2 and μ^3 minima (**29** and **30**) are bridged by the transition state **32**. A fourth minimum (**33**) having a dissociated CO group lies much higher in energy, 1 eV above the zero energy. We have located a singlet-triplet MECP structure (**34**) that is intermediate between a μ^1 and a μ^2 structure (one of the Pd-C bond lengths is slightly longer). Further study on the singlet surface reveals two minima with μ^1 and μ^3 geometries, the latter being the global minimum at -3.70 eV. We could not locate a transition state connecting these two minima.

For Ag_3 we considered doublet, quartet, sextet and octet multiplicities with the doublet state being significantly lower in energy than the higher multiplicities. The minimum has C_{2v} symmetry, in agreement with the recent DFT calculations by Zhou *et al.* [97]. Ag_3 is one of the few triatomic metal clusters that have been observed via gas phase electronic spectroscopy. Cheng and Duncan [98] produced a resonance ionization spectrum that was consistent with a ^{2}E' ground state with dynamic Jahn-Teller distortion. Subsequent re-recording and analysis of the same spectrum led Wallimann *et al.* to the same conclusion [99].

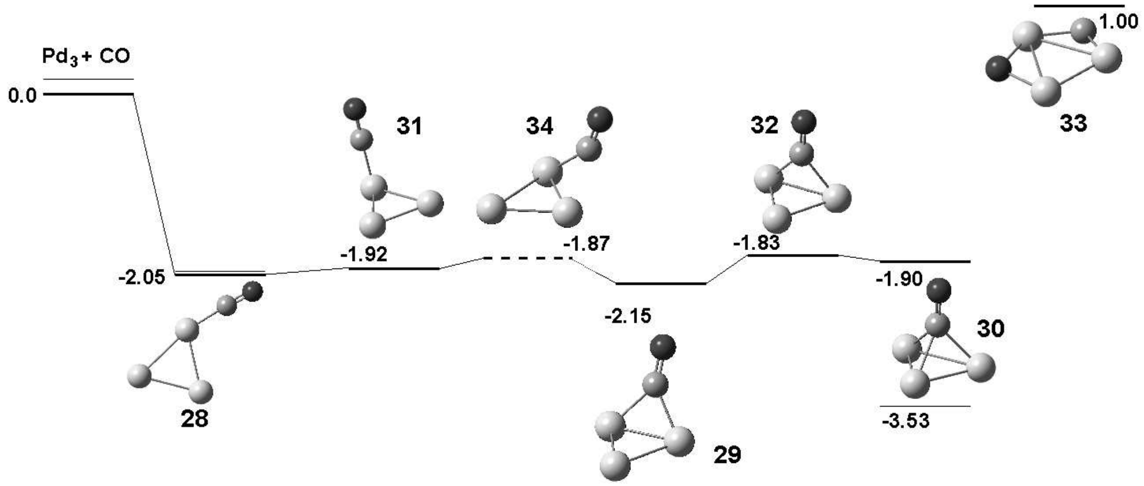

Figure 1.6: Stationary points on the Pd_3 + CO potential energy surface for the energetically competitive multiplicities. The bold lines represent the triplet state and the fine lines represent the singlet state. The dashed line (structure 34) represents the energy where the singlet and triplet surfaces cross. Reported energies are relative to the zero energy of the triplet state and are given in eV.

Upon addition of CO, our calculations yielded three minima that are only weakly bound as shown in Figure 1.7. Again, doublet states were found to be much lower in energy than other multiplicities and these are reported in Table 1.7. The lowest energy structure has a planar μ^1 geometry (**35**) that is bound by -1.07 eV. A planar μ^2 structure (**36**) has a slightly weaker bonding energy of -0.76 eV. A very weakly bound (-0.24 eV) third minimum (**37**) has a planar μ^1 structure in which the O atom approaches the Ag_3 moiety. The transition state (**38**) at -0.12 eV has an unusual structure where the CO moiety is side bound to a silver atom. This transition state is the link between **35** and **36**. However, this structure must also be involved in any reaction pathway leading to **37** where the CO group can be thought of as undergoing internal rotation relative to, and within the plane of, Ag_3. Indeed, inspection of the imaginary frequency of this transition state shows just this. The lowest energy structure in which the CO was dissociated (**39**) lies +4.25 eV above the zero energy. The relatively weak binding energy exhibited by structures **35** and **36** is conspicuous compared with the other metal trimers in this study, being significantly less than even Pd_3. However, as noted in previous work by Jellinek *et al.* [100] and Rayner *et al.* [101], this is expected owing to the $d^{10}s^1$ configuration being unable to undergo the sd hybridization necessary for strong bonding. In the DFT study by

	$S = \frac{1}{2}$	
Ag_3	-442.3482359	
Ag_3 + CO	-555.8651371	
35	-555.9044273	-1.07
37	-555.8694464	-0.12
36	-555.8931679	-0.76
38	-555.8727945	-0.24
39	-555.7089384	4.25

Table 1.7: Absolute energies (in hartree) and relative energies (in eV) of the doublet multiplicity for the Ag_3 and Ag_3-CO complex structures.

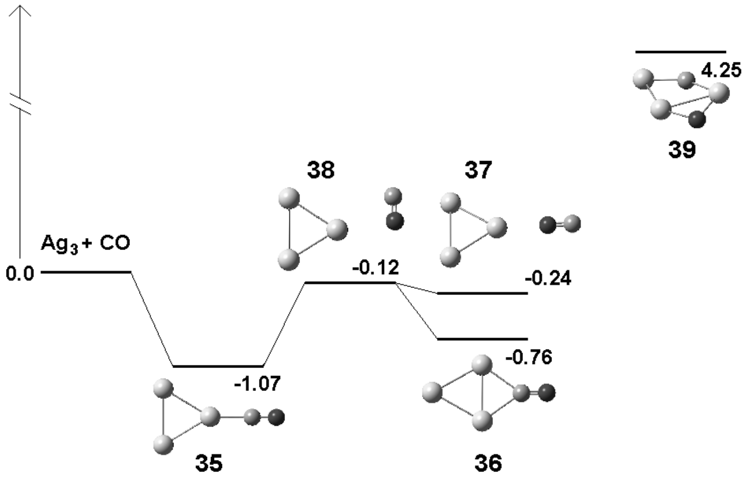

Figure 1.7: Stationary points on the Ag_3 + CO potential energy surface for the doublet multiplicity. Relative energies are given in eV.

Zhou *et al.* [97], only one structure was found for Ag_3CO, having a binding energy of -0.87 eV, slightly less than our value of -1.07 eV.

1.3.4 From Nb_3 to Ag_3: Periodic Trends

For each potential energy surface, the first structure shown is a μ^1-bound species; it has the least interaction with the M_3 cluster and thus the highest CO vibrational frequency. We call this the "capture" species. This structure then has the opportunity to relax to a lower energy structure that may be either dissociative or associative. Therefore, we can consider three types of M_3-CO species, namely capture, associative and dissociative. Figure 1.8 shows the energies

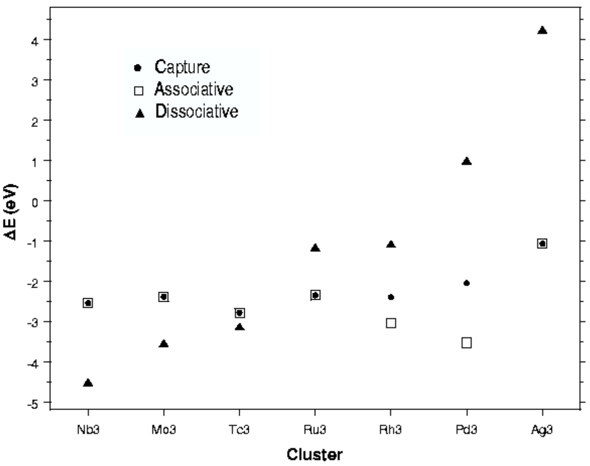

Figure 1.8: Plot of the binding energy of the capture species (●), lowest energy associative structure (□) and lowest energy dissociative structure (▲) for each metal trimer, regardless of multiplicity.

for these structures as a function of the metal cluster (effectively the group number) relative to the zero energy of the separated M_3 + CO, regardless of multiplicity. There are several interesting features to note. First, the energies of all the capture species (with the exception of Ag_3) are very similar, ranging from -2.80 to -2.05 eV. The Ag_3CO capture species is weakly bound (as discussed above) with a binding energy of only -1.07 eV. For Nb_3, Mo_3, Tc_3 and Ru_3, the capture species is the lowest energy associative species (i.e. the ● and □ data points lie on top of one another in Figure 1.8). Lower energy associative structures exist for Rh_3 and Pd_3, bound by at least -3 eV. For Ag_3, the capture and associative species are the same. Perhaps the most striking feature of the figure is the energy of the dissociative species (▲), which increases non-linearly from -4.51 eV for Nb_3 to +4.25 eV for Ag_3. It is immediately seen that the early transition metal clusters (Nb_3, Mo_3 and Tc_3) have global energy minima in which the CO is dissociated, in contrast to the late transition metal clusters where the CO remains intact.

One possible way to rationalize the relative energies (as one moves across the Periodic table) of the various dissociative structures is to consider the thermodynamic stabilities of the M-C and M-O bonds. The difference in energy between the associative and dissociative structures can be approximated by the gain in energy upon formation of metal-carbide and metal-oxide

	D°_{298} (kJmol^{-1})		D°_{298} (kJmol^{-1})	M-C+M-O (kJmol^{-1})	M-C+M-O (eV)
Nb-O	772 ± 25	Nb-C	569 ± 13	1341	13.90
Mo-O	560 ± 21	Mo-C	481 ± 16	1041	10.79
Tc-O	543	Tc-C	565 ± 29	1108	11.48
Ru-O	528 ± 42	Ru-C	616 ± 11	1144	11.86
Rh-O	405 ± 42	Rh-C	580 ± 4	985	10.21
Pd-O	381 ± 84	Pd-C	296	677	7.02
Ag-O	220 ± 21	Ag-C	160	380	3.94

Table 1.8: Literature bond strengths,D°_{298}, for the transition metal oxides and carbides (Ref [101–103]). The final two columns show the sum of the two energies (in kJmol^{-1} and eV, respectively

bonds. The bond strengths,D°_{298} , for the individual M-C and M-O bonds are mostly known from the literature [102] apart from an estimated value for Tc-O [103] and two values which we have calculated for Pd-C and Ag-C: [Energy calculations and geometry optimization for diatomics performed at B3P86/SDD level of theory: C ($2S$+1=3, E= -37.948984 a.u), Pd ($2S$+1=1, E= -128.2898262 a.u), PdC($2S$+1=3, r_e = 1.80Å, E = -166.3513966 a.u.), Ag ($2S$+1=2, E= -147.4204955 a.u), AgC ($2S$+1=4, r_e =2.04Å E = -185.4303893 a.u.]. These bond strengths are listed in Table 1.8. It is important to realize that these values reflect the difference in energy from the lowest electronic states of each molecule to the lowest states of the separated atoms. For the oxides, this is the lowest energy state of the metal atom and the ^{3}P state of oxygen; however, this is not the case for the carbides. Here, the lowest energy states of the metal carbides tend to have low spin (relative to their oxygen analogues), which correlates with excited electronic states of the metal atom [104, 105]. For example, the $^3\Sigma^-$ ground state of MoC arises from the ^{3}P state of C and the ^5S state of Mo, which is 1.335 eV higher in energy than the ^7S ground state [104]. Therefore, to determine the intrinsic bond strength for a particular state of the molecule this promotional energy needs to be added to the experimentally derived energies. However, the dissociative energies plotted in Figure 1.8 (▲) are regardless of multiplicity, and so can be compared simply with the sum of the M-C and M-O energies shown in the final two columns of Table 1.8.

From Table 1.8, it can be seen that there is a general trend in decreasing bond strength from niobium to silver. Certainly, niobium is predicted to form the strongest carbide + oxide bonds, in accord with Figure 8 (▲). Rhodium, palladium and silver are predicted to form progressively weaker bonds, again in agreement with Figure 8. The intermediate metals (molybdenum, technetium and ruthenium) are predicted to have carbide + oxide bonds of quite similar strength (within 1.1 eV) and do not follow the trends in Figure 8. Considering that every dissociated structure contains μ^2-bound carbon and oxygen atoms and the added complexity of the metal-metal bonding, it is surprising that treating their bonding as a simple sum of isolated diatomic bonds works as well as it does.

Although knowledge of the bond enthalpies for metal-carbide and metal-oxide formation can approximate the relative binding energies of the dissociated structures across the series, it does not serve to predict whether the associative or dissociative structure will be the global minimum. When considering the requirements of a cluster to dissociate the CO molecule, the classic Blyholder picture for CO interactions with a metal centre is a useful starting point [106]. Donation of CO σ density into the metal centre precedes back-donation into the CO π^* orbitals. The extent of this back-bonding determines how much the CO bond will be weakened, which may be measured by its vibrational frequency. The greater the extent of this back-donation, the weaker the carbon monoxide bond, until at some threshold carbon monoxide dissociates.

The capture species is the stationary point that corresponds to the initial interaction between the reactants. In all cases, this structure has the CO μ^1-bound to the metal trimer and is shown as the first structure in each of the potential energy surfaces in Figures 1-7. This capture species also has the highest CO vibrational frequency on any given M_3CO potential energy surface. For each of these capture species, the calculated vibrational frequencies, shown in Table 1.9, are seen to be significantly reduced from the value for free CO, calculated to be 2046 cm^{-1}. Further, these frequencies decrease steadily from Pd_3 to Nb_3 (although the value

	$\nu_{(CO)}$ of capture species (cm^{-1})	ΔE CO π* orbital (a.u.)
Nb_3	1649	0.02153
Mo_3	1767	0.02781
Tc_3	1848	0.03911
Ru_3	1905	0.00704
Rh_3	1949	0.00012
Pd_3	1999	-0.00565
Ag_3	1967	-0.02675
CO	2046	0.00000

Table 1.9: CO vibrational frequencies (including free CO), together with the change in energy (relative to E = -0.04482 a.u) for the CO π* orbital, calculated for each M_3CO capture species. See text for discussion of these data.

for Ag_3 is slightly less than for Pd_3). Consistent with the underlying premise of Blyholder's model, this indicates that there is more back-bonding occurring from palladium to niobium.

To further explore the extent of back-bonding, an NBO analysis was performed on the π* CO orbitals into which this back-donation occurs. This analysis shows that of the two formerly degenerate CO π* orbitals (E = -0.04482 a.u), one undergoes significant sp mixing whereas the other completely retains its p-type character. We find that the energy of the latter orbital undergoes changes with different M_3 species and this relative energy change is also tabulated in Table 1.9. For Nb_3, Mo_3 and Tc_3, the orbital energy increases by +0.02153, +0.02781 and +0.03911 a.u., respectively. For these species, the global minimum is a dissociative structure. For Ru_3, the orbital energy increases slightly by +0.00704 a.u. and for Rh_3 the energy change is negligible at -0.00012 a.u. For these species, the global minimum is an associative structure, however, a dissociative structure exists that is below zero energy. For Pd_3 and Ag_3, the orbital energy is reduced by -0.00565 and -0.02675 a.u., respectively. For both these species, an associative structure is the global minimum and the dissociative state is above zero energy. Therefore, it seems that the sign of this orbital energy is a barometer to determine whether CO will dissociate or not.

1.3.5 Conclusion

We have explored the chemistry of the reaction of CO with the $4d$ transition metal trimers, Nb_3 to Ag_3, using density functional theory. Several minima, at a range of multiplicities, were found for each system and these were linked by IRC calculations, leading to proposed reaction pathways containing associatively and dissociatively bound structures. In those cases where two or more multiplicities cross, Minimum Energy Crossing Points were calculated.

The relative energies of the dissociative structures were found to increase from Nb_3 to Ag_3. The left-most metal trimers (Nb_3, Mo_3 and Tc_3) were found to have global minima in which the CO molecule dissociates. All other trimers were found to have associative structures at their global minima. Pd_3 and Ag_3 do not possess dissociative structures lying below the energy of the separated moieties.

Natural Bond Order analyses on the μ^1 M_3CO capture species, examining the effect of the metal trimer on the energy of the pure p-type CO π^* orbital, serve to differentiate those species that thermodynamically dissociate CO, from those that did not.

Chapter 2

Better than DFT? Multireference calculations on TM clusters.

TRANSITION metal clusters are characterised by a high density of states which complicates both experimental and computational investigation. Computationally, the density of states hampers the ability of single-reference methods to accurately capture the desired chemistry and multireference methods are therefore indicated. In this chapter, CASSCF and MRCI methods are used to investigate Nb_3N_2 and Nb_3C_2 which have both been spectroscopically characterised, in order to determine the agreement between multireference methods, DFT and experiment. These two clusters are ideal candidates to study as the known spectroscopy can serve to validate the computational results, yet there is still room for the calculations to inform further spectroscopy.

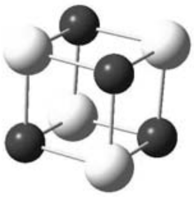

2.1 Nb_3

2.1.1 Nb_3

Transition metal clusters are characterised by a high density of states, which hampers both spectroscopic and computational elucidation of their structure and properties. Computationally, the high density of states suggests that multireference techniques may be necessary for accurate determination of cluster properties. The large number of electrons that need to be treated however, means that even the smallest of clusters are expensive to model. Consequently, very few transition metal clusters, larger than diatomic species, have been examined using multireference methods. Those that have been investigated include Nb_{3-5} [107–109], Ru_3 [110], Rh_3 [20, 89], Pd_3 [94] and Ag_3 [111]. The purpose of this study is to investigate the structures of neutral and cationic Nb_3C_2 and Nb_3N_2 clusters using DFT, CASSCF and MRCI methods.

In order to test the proposed computational method, a known system was required. The Nb_3 sub-unit common to both Nb_3N_2 and Nb_3C_2 has previously been investigated using DFT, CASSCF and MRCI methods and its Ionisation Potential (IP) has been experimentally determined. Balsubramanian *et al.* investigated the first four multiplicities of Nb_3 and Nb_3^- in C_{2v} symmetry [107]. The current work seeks to re-examine the doublet states of neutral Nb_3, whose geometry is shown in Figure 2.1. DFT calculations were undertaken using Gaussian03 [78], CASSCF and MRCI calculations were carried out using Molpro [112, 113]. All calculations used the Stuttgart RSC (srsc) basis set and corresponding quasi-relativistic ECP which replaces the first 28 electrons. The Stuttgart RSC basis set for niobium has $8s$, $7p$ and $6d$ functions which are contracted to $(6s,5p,3d)$. This is in contrast to the work of Balasubramanian, who used the ECP and basis of LaJohn and co-workers [114]. This basis set has $5s$, $5p$ and $4d$ functions which were contracted to $(5s,3p,2d)$.

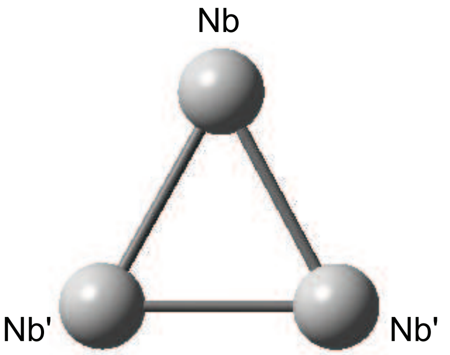

Figure 2.1: Geometry of Nb_3 in C_{2v} symmetry.

Firstly, the cluster was re-examined using B3LYP/srsc. The results, shown in Table 2.1, are in good agreement with those of Balasubramanian, reproduced in Table 2.2, with the ground state being predicted to be a $^2B_1$ state and $E(^2B_1) < E(^2A_2) < E(^2A_1) < E(^2B_2)$. However some discrepancies do exist; the $^2B_1$ state, which is the ground state at B3LYP/srsc was found to have to equal bond lengths of 2.348Å rather than the 2.527Å presented by Balasubramanian. The geometry presented by Balasubramanian for this state (viz. Nb-Nb$'$ $=$ 2.527Å, Nb$'$-Nb$'$ bondlength of 2.468Å and Nb$'$-Nb-Nb$'$ of 63.4°), is inconsistent with the model geometry used (as Nb-Nb$'$ $>$ Nb$'$-Nb$'$ $\iff$ Nb$'$-Nb-Nb$'$ $< 60°$) . In addition, the $^2A_2$ and the $^2A_1$ states, 0.01 and 0.64 eV above the global minimum respectively, were identified as transition states in this study, rather than minima as reported previously. A lower energy $^2A_1$ minimum was located and is shown in Table 2.1, however no lower energy $^2A_2$ minimum was located in C_{2v} symmetry.

Secondly the CASSCF and MRCI wavefunctions for the doublet states of C_{2v} Nb_3 were re-examined. The previous study of Balasubramanian *et* al. [107] cited a complete valence active space of $11a_1$, $5a_2$, $6b_1$, $8b_2$ orbitals from which they define a core of $5a_1$, a_2, $2b_1$ and $4b_2$ orbitals and a restricted active space of $5a_1$, a_2, $3b_1$ and $2b_2$ orbitals. However a symmetry adapted linear combination of $4s$, $4p$, $4d$ and $5s$ orbitals for a C_{2v} configuration of Nb_3, yields a complete valence active space comprised of $12a_1$, $4a_2$, $5b_1$ and $9b_2$ orbitals (depicted in Appendix A), so it is unclear how the orbitals in the complete active space of Balasubramanian *e*t al. were generated. It is additionally unclear, from their description, which 15 orbitals were chosen as the restricted active space as they do not account for all orbitals, nor do they specify how they ensured that no other (external) orbitals intruded on their valence active space.

State	Nb-Nb′ (Å)	Nb′-Nb′ (Å)	Nb′-Nb-Nb′ (°)	ΔE (eV)	$\bar{\nu}$ (cm^{-1})
$^2B_1$	2.35	2.47	63.5	0.00	63,228,360
$^2A_2$	2.44	2.29	55.9	0.01	213i,233,360
$^2A_1$	2.45	2.47	61.1	0.52	127,215,313
$^2B_2$	2.51	2.32	55.0	0.58	43,213,361
$^2A_1$	2.56	2.22	51.3	0.64	66i,225,384

Table 2.1: Geometric parameters, relative energies and vibrational frequencies of doublet states of Nb_3 at the B3LYP/srsc level.

State	Nb-Nb′ (Å)	Nb′-Nb′ (Å)	Nb′-Nb-Nb′ (°)	ΔE (eV)	$\bar{\nu}$ (cm^{-1})
$^2B_1$	2.527	2.468	63.4	0.00	67,230,366
$^2A_2$	2.439	2.286	56.0	0.01	231,280,376
$^2A_1$	2.391	2.390	60.0	0.21	232,232,373
$^2A_1$	2.565	2.226	51.4	0.69	76,118,427
$^2B_2$	2.508	2.321	55.1	0.63	36,215,365

Table 2.2: Geometric parameters, relative energies and vibrational frequencies of doublet states of Nb_3 at the B3LYP/srsc level taken from reference [107].

In the present work, to select the restricted active space from the symmetry adapted orbitals, all linear combinations of $4s$ and $4p$ orbitals ($5a_1$, a_2, $2b_1$, $4b_2$) were defined as core orbitals, these orbitals were always doubly occupied, but they were allowed to relax. A first attempt, defined the same active space as the previous work (defining the remaining valence orbitals as always unoccupied), however in these calculations, the lowest two a_1, the a_2 and the lowest b_1 orbitals were always doubly occupied. Therefore a new active space was chosen, incorporating these orbitals into the core. This led to the lowest active a_2 and b_1 orbitals always being unoccupied. The final active space consisted of a core of $8a_1$, a_2, $2b_1$, $4b_2$ orbitals and an active space of $3a_1$, $2a_2$, $3b_1$ and $3b_2$ orbitals. The remaining orbitals were always unoccupied. 9 electrons were inserted into the active space resulting in up to 19000 Configuration Spin Functions (CSFs) being included. Geometric parameters and ΔE at the CASSCF and MRCI

State	Nb-Nb′ (Å)	Nb′-Nb′ (Å)	Nb′-Nb-Nb′ (°)	ΔE_{CASSCF} (eV)	ΔE_{MRCI} (eV)	ΔE_{MRCI+Q} (eV)
$^2A_1$	2.74	2.29	49.4	0.00	0.45	0.67
$^2A_2$	2.67	2.30	51.0	0.56	1.11	1.39
$^2B_1$	2.38	2.54	64.5	0.61	0.00	0.00
$^2B_2$	2.34	2.71	70.7	0.86	0.39	0.37

Table 2.3: CASSCF geometric parameters and relative energies of doublet electronic states of Nb_3 at the CASSCF and MRCI levels.

State	Nb-Nb′ (Å)	Nb′-Nb′ (Å)	Nb′-Nb-Nb′ (°)	ΔE_{CASSCF} (eV)	ΔE_{MRCI} (eV)	ΔE_{MRCI+Q} (eV)
$^2A_1$	2.770	2.246	47.8	0.00	0.21	0.00
$^2A_2$	2.559	2.445	57.1	0.54	0.60	0.92
$^2B_1$	2.339	2.577	66.8	0.66	0.00	0.55
$^2B_2$	2.496	2.468	59.2	0.99	0.83	1.43

Table 2.4: CASSCF geometric parameters and relative energies of doublet electronic states of Nb_3 at the CASSCF and MRCI levels taken from reference [107].

levels are shown in Table 2.3.

Given that the present work uses a different active space to the work of Balasubramanian *et* al., it is surprising that the results agree as well as they do. The literature results for the doublet states are reproduced in Table 2.4. At the CASSCF level, both the previous study and this find $E(^2A_1) < E(^2A_2) < E(^2B_1) < E(^2B_2)$. Geometric parameters for the $^2A_1$ and $^2B_1$ states are in reasonable agreement, however, the geometries of the $^2A_2$ and $^2B_2$ states, do not agree with those of Balasubramanian, despite having similar ΔE.

Photoelectron Spectra

Keitzmann *et al.* measured the photoelectron spectrum of the niobium trimer anion [115]. The spectrum shows a peak at 1.1 eV corresponding to the electron affinity of Nb_3 and further peaks at 1.45 (small) , 1.8 and 2.1 eV. The ΔE between these peaks and the peak at 1.1 eV (i.e. 0.35, 0.7 and 1.0 eV respectively) correspond to excited states of the neutral trimer. Balasubramanian *et al.* proposed an assignment of this spectrum using their MRCI results as they felt these were more accurate than their MRCI+Q results. They assign their $^2A_2$ state

This work		Ref [107]		Expt	
State	ΔE	State	ΔE (MRCI+Q)	Peak position	ΔE
$^2B_1$	0.00	$^2B_1$	0.00 (0.55)	1.1	0.00
		$^2A_1$	0.21 (0.00)		
$^2B_2$	0.37			1.45	0.35
$^2A_1$	0.67	$^2A_2$	0.60 (0.92)	1.8	0.7
$^2A_2$	1.39	$^2B_2$	0.83 (1.43)	2.1	1.0

Table 2.5: Assignment of the photoelectron spectrum of Nb_3 [115]. All energies are in eV. The relative energies used from this work are the MRCI+Q energies. Both MRCI and MRCI+Q (in parentheses) ΔE are quoted from reference [107], they used the MRCI energies in their assignment of the spectrum.

to the peak at 1.8 eV and their $^2B_2$ state to the 2.1 eV peak. In addition they gave possible quartet and sextet assignments for the peaks at 1.8 and 2.1 eV, they do not consider the peak at 1.45 eV.

Considering the MRCI+Q results obtained in this work (Table 2.3), the $^2B_2$ state corresponds well with the experimental 0.35 eV ΔE. The $^2A_1$ state, calculated to be 0.67 eV above the ground state is a good candidate for the second excited state in the photoelectron spectrum, 0.7 eV above the ground state. The $^2A_2$ state calculated in this study is a less likely candidate for the 2.1 eV peak, with a ΔE of 1.39 eV vs. 1.0 eV in the photoelectron spectrum. It is probable that this peak corresponds to a quartet (or higher) spin state. The assignment of the spectrum along with Balasubramanian's assignment and the experimental data is tabulated in Table 2.5.

2.1.2 Nb_3^+

Prior to their publication on Nb_3 and Nb_3^-, the same authors also published an investigation into Nb_3^+ [109] at DFT, CASSCF and MRCI levels. In this paper, Balasubramanian proposed a strongly acute $^5A_2$ geometry with two equal bond lengths of 3.315Å, and an angle between them of only 39.3° but this state would be inaccessible from the $^2A_1$ ground state of the

State	Nb-Nb′ (Å)	Nb′-Nb′ (Å)	Nb′-Nb-Nb′ (°)	ΔE (eV)	$\bar{\nu}$ (cm^{-1})
^{1}B$_2$	2.45	2.40	58.6	0.00	141,194,314
^{1}A$_1$	2.49	2.29	54.5	0.29	81,270,379
^{1}A$_1$	2.34	2.59	67.0	0.31	139i,216,378
^{1}B$_1$	2.54	2.49	58.6	0.81	225,261,317
^{1}A$_2$	2.47	2.62	63.9	1.20	192,194,314

Table 2.6: Geometric parameters, relative energies and vibrational frequencies of singlet states of Nb$_3^+$ at the B3LYP/srsc level.

neutral. However, in their later paper on the neutral and anionic niobium trimer, they report that MRCI+Q calculations undertaken on the ^{5}A$_2$ and ^{1}A$_2$ geometries result in the ^{1}A$_2$ being lower than the ^{5}A$_2$ by 0.81 eV. At the MRCI level, they found the ^{3}A$_2$ state to be only 0.19 eV above the ^{5}A$_2$ state, yet they did not calculate this state at the MRCI+Q level. DFT studies by Fowler and co-workers [83] predict a ^{3}A$_1'$ cation with D_{3h} symmetry.

As it was not the intent of this work to re-investigate all possible states for Nb$_3$ and Nb$_3^+$, only the singlet species were re-examined. Calculations on the singlet species were undertaken at the DFT, CASSCF, MRCI and MRCI+Q levels of theory.

B3LYP/srsc geometries, frequencies and relative energies are presented in Table 2.6. It is difficult to compare these states to those of Balasubramanian as his work only presents a ^{1}A$_1$ transition state at this level of theory. A search for this transition state located it 0.31 eV above the lowest energy singlet structure (^{1}B$_2$) found in this work.

The CASSCF geometries and MRCI wavefunctions of the singlet states of Nb$_3^+$ were optimised, beginning from the previously published geometries and are presented in Table 2.7. These geometries bear little resemblance to those presented by Balasubramanian (Table 2.8), perhaps highlighting the importance of the choice of active space. In particular, the lowest energy singlet state identified by Balasubramanian was a ^{1}A$_2$ geometry with two long sides and one short, whereas in this work the ^{1}A$_2$ state identified had three nearly equal bondlengths

State	Nb-Nb′ (Å)	Nb′-Nb′ (Å)	Nb′-Nb-Nb′ (°)	$\Delta E_{\mathrm{CASSCF}}$ (eV)	ΔE_{MRCI} (eV)	$\Delta E_{\mathrm{MRCI+Q}}$
$^1A_1$	2.38	2.74	70.2	0.00	0.00	0.00
$^1B_2$	2.52	2.42	57.4	0.66	0.18	0.18
$^1B_1$	2.43	2.56	63.7	0.89	0.46	0.49
$^1A_2$	2.54	2.53	59.7	1.38	1.36	1.29

Table 2.7: CASSCF geometric parameters and relative energies of doublet electronic states of Nb_3^+ at the CASSCF and MRCI levels.

State	Nb-Nb′ (Å)	Nb′-Nb′ (Å)	Nb′-Nb-Nb′ (°)	$\Delta E_{\mathrm{CASSCF}}$ (eV)	ΔE_{MRCI} (eV)	$\Delta E_{\mathrm{MRCI+Q}}$ (eV)
$^1A_2$	2.654	2.457	55.2	0.23	0.11	0.00
$^1B_1$	2.536	2.650	63.0	0.96	0.42	
$^1A_1$	2.448	2.701	67.0	0.63	0.47	
$^1B_2$	2.588	2.578	59.8	2.24	1.82	

Table 2.8: CASSCF geometric parameters and relative energies of doublet electronic states of Nb_3^+ at the CASSCF and MRCI levels taken from reference [109].

and an apex angle of 59.7° and was the highest in energy of all the singlet states.

The leading configuration of the $^1A_1$ state is
$1a_1^2\cdots 9a_1^2 1b_1^2\cdots 4b_1^2 1b_2^2\cdots 5b_2^2 1a_2^2$,
which agrees with the configuration of the B3LYP minimum. However this leading configuration comprises only 69% of the total wavefunction at the CASSCF level and this contribution decreases to 60% at the MRCI level. The configuration of the B3LYP transition state is
$1a_1^2\cdots 9a_1^2 1b_1^2\cdots 3b_1^2 1b_2^2\cdots 5b_2^2 1a_2^2 2a_2^2$.
Likewise, the leading configuration of the $^1B_2$ state agrees with the B3LYP configuration of
$1a_1^2\cdots 9a_1^2 1b_1^2\cdots 3b_1^2 4b_1^1 1b_2^2\cdots 5b_2^2 1a_2^2 2a_2^1$
but comprises only 66% of the CASSCF wavefunction. It is clear that minor configurations have strong influence on the geometry. Despite the difference in geometries between the B3LYP and CASSCF calculations, both sets of calculations agree that the $^1A_1$ and $^1B_2$ states are low in energy (0.0 - 0.3 eV) followed by the $^1B_1$ state and all calculations place the $^1A_2$ state approximately 1.25 eV above the lowest energy singlet geometry.

2.1.3 IP Calculations

The (adiabatic) Ionisation Potential (IP) of a cluster is the difference in energy between the neutral and cationic ground states and is a parameter that is readily measured by experiment. The IP of Nb_3 has been measured by Knickelbein and Yang [116] and has a value of 5.81 ± 0.05 eV. It was expected that the MRCI calculation of the IP would be sensitive to the quality of the basis set, in particular, it is expected that f functions would be required to accurately describe the correlation of the d electrons. Therefore, in addition to the Stuttgart RSC basis set employed to determine the geometries (which is of double-ζ quality), single point energy calculations were undertaken on the CASSCF geometries using basis sets of triple-ζ ($10s9p8d2f1g//5s5p4d2f1g$)and quadruple-ζ ($14s11p10d3f2g1h//6s6p5d3f2g1h$) quality [117]. The calculated IPs are presented in Table 2.9. Adiabatic IPs are presented relative to the lowest energy neutral and cationic species. Therefore, the MRCI and MRCI+Q IPs refer to the $^2A_1 \rightarrow ^1A_1$ transition, whereas the B3LYP IP refers to the $^2B_1 \rightarrow ^1B_2$ transition.

Using a ($5s5p4d//5s3p2d$) basis set, the study of Balasubramanian predicts the IP of Nb_3 to be 4.50 eV at the MRCI level of theory, inclusion of unlinked quadruples (MRCI+Q) improves this result to 5.09 eV. Single point energies using a larger ($6s6p5d1f//6s4p4d1f$) basis predict IPs of 5.42 eV and 5.61 eV at the MRCI and MRCI+Q levels of theory respectively.

Consistent with the work of Balasubramanian, the smallest basis used in this work, while providing useful geometric parameters, underestimates the IP by over 1 eV at the MRCI level and ≈ 1 eV using MRCI+Q. Owing to the different states considered by this study and that of Balasubramanian, exact comparison of IPs is not possible, however some broad comparisons can be made.

The IPs predicted at the MRCI and MRCI+Q levels of theory in this study fall within a narrower range than those of Balasubramanian (4.7-5.2 eV vs. 4.5-5.6 eV) and all predictions fall short

	Calculated Transition	IP
srsc		
MRCI	$^2A_1 \rightarrow ^1A_1$	4.720
MRCI+Q		4.860
cc-pVTZ		
MRCI		4.930
MRCI+Q		5.180
cc-pVQZ		
MRCI		4.966
MRCI+Q		5.231
B3LYP/srsc	$^2B_1 \rightarrow ^1B_2$	5.691
Experiment		5.81 ± 0.05

Table 2.9: Ionisation Potential of Nb_3 calculated using basis sets of increasing quality. All values are in eV. Experimental IP taken from reference [116].

of the experimental value of 5.81 eV. The inclusion of unlinked quadruple excitations raises the predicted IP, however, in this study, the improvement was only of the order of 0.15-0.25 eV rather than the 0.21-0.59 eV observed by Balasubramanian. It is also apparent in this work that little improvement in IP is gained by increasing the basis set beyond triple-ζ level, and hence this basis set was used on niobium atoms in subsequent single point energy calculations.

It is possible that the larger active space used by Balasubramanian allows greater improvement in IP implying that correlation of d electrons in doubly occupied orbitals has a significant effect that is only captured when large basis sets are used. Despite these difficulties, it was felt that the choice of active space and basis set used in this study provided more consistent results and so this methodology was used to investigate two clusters that have previously only been studied at the DFT level: Nb_3N_2 and Nb_3C_2.

2.2 Nb_3N_2

2.2.1 Nb_3N_2

Nb_3N_2 and $Nb_3N_2^+$ have been studied by Yang *et al.* using a combination of PFI-ZEKE and DFT [23]. This study predicts similar geometries for both the neutral and cationic species. DFT calculations considered both doubly and triply bridging structures (Figure 2.2) and found a doubly bridging geometry with overall C_{2v} symmetry for the structure of both the neutral and cation.

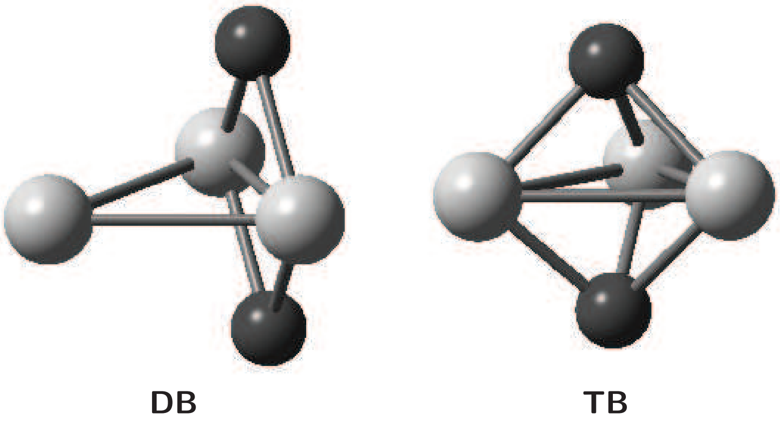

Figure 2.2: Doubly (DB) and triply bridged (TB) Nb_3X_2 structures. In both structures, the unique niobium atom is the leftmost atom.

The full valence active space of Nb_3N_2 and $Nb_3N_2^+$ includes 40 orbitals in C_{2v} symmetry, ($16a_1$, $5a_2$, $6b_1$, $13b_2$). These orbitals are depicted in Appendix A. Using this complete active space leads to an excessive number of Configuration Spin Functions (CSFs). Therefore, in order to make the calculations tractable, a reduced active space was employed. The niobium $4s$ and $4p$ and nitrogen $1s$ orbitals ($6a_1$, $1a_2$, $4b_1$, $3b_2$) were considered to be always doubly occupied (closed). The active space of the remaining 26 orbitals was still too large to be tractable so to determine the optimal reduced active space, preliminary CASSCF calculations were undertaken with a large active space. Orbitals that were doubly occupied in all configurations were considered closed and high energy orbitals that were not occupied in any configurations were removed from the active space. The resultant active space considered the lowest $9a_1$, $2a_2$, $5b_1$

and $5b_2$ orbitals to be closed and included the next $3a_1$, $2a_2$, $3b_1$ and $2b_2$ orbitals as the active space. 11 electrons, (10 in the case of $Nb_3N_2^+$) electrons were placed in the active space. No excitations were allowed from the closed orbitals, however, they were allowed to relax. This approach led to a total of 7000 CSFs being included.

Full geometry optimisations of each electronic state up to the octet were undertaken at the CASSCF level using the Werner-Meyer-Knowles [112, 113] technique. For electronic states up to and including quartet states, the CASSCF calculations were followed by single point MRCI calculations [118, 119]. All CASSCF configurations with absolute coefficients of $\geq$0.05 were included as reference configurations. To estimate the effect of unlinked quadruple excitations, the Davidson correction [120], was employed. The niobium atoms were treated with the Stuttgart basis set and had the first 28 electrons replaced with a quasi-relativistic ECP. Nitrogen atoms were treated with Dunning's correlation-consistent valence double-ζ (i.e. cc-pVDZ). All calculations were undertaken in the C_{2v} point group.

Single point MRCI and MRCI+Q calculations were undertaken on all states of the lowest two multiplicities for both the neutral and cationic species (i.e. neutral doublets and quartets and cationic singlets and triplets). These calculations included up to 125 million configurations. In order to investigate the effect of basis set on the MRCI predicted IP, several single point MRCI calculations employing different basis set combinations, were undertaken on the neutral and cationic ground states.

Frequency calculations were undertaken using DFT optimised geometries of each electronic symmetry. DFT calculations were undertaken using Gaussian 03 [78] and employed the B3LYP functional with the Stuttgart (srsc) basis set and associated ECPs for niobium atoms and D95V for carbon atoms. As in the CASSCF calculations, all geometries were constrained to C_{2v} symmetry.

The CASSCF calculated geometries and relative energies for electronic states of $\mathrm{Nb_3N_2}$ are shown in Table 2.10. The CASSCF ground state is predicted to be a $^2\mathrm{B}_1$ state with a doubly bridging geometry. All other states are $\geq$ 1 eV higher in energy. The MRCI wavefunction of the $^2\mathrm{B}_1$ state is:
$(63\% \mid 1a_1^2 \cdots 11a_1^2 1b_1^2 \cdots 6b_1^2 7b_1^1 1b_2^2 \cdots 6b_2^2 1a_2^2 \cdots 3a_2^2\rangle$
$+\, 2.2\% \mid 1a_1^2 \cdots 12a_1^2 1b_1^2 \cdots 6b_1^2 7b_1^1 1b_2^2 \cdots 6b_2^2 1a_2^2 3a_2^2\rangle$
$+\, 1.9\% \mid 1a_1^2 \cdots 10a_1^2 12a_1^2 1b_1^2 \cdots 6b_1^2 7b_1^1 1b_2^2 \cdots 6b_2^2 1a_2^2 \cdots 3a_2^2\rangle$
$+\, 1\% \mid 1a_1^2 \cdots 11a_1^2 1b_1^2 \cdots 5b_1^2 7b_1^1 8b_1^2 1b_2^2 \cdots 6b_2^2 1a_2^2 \cdots 3a_2^2\rangle$
$+\, 1\% \mid 1a_1^2 \cdots 10a_1^2 11a_1^1 12a_1^1 1b_1^2 \cdots 6b_1^2 7b_1^1 1b_2^2 \cdots 6b_2^2 1a_2^2 2a_2^1 3a_2^1\rangle)$.
At the CASSCF level, the next three states ($^2\mathrm{A}_1$, $^4\mathrm{B}_1$ and $^2\mathrm{A}_2$) all lie $1.0 \leq \Delta\mathrm{E} \leq 1.2$ eV above the ground state energy, at the MRCI level, these states rise sharply in energy, with only the $^4\mathrm{B}_1$ state possessing a ΔE less than 2 eV at the MRCI and MRCI+Q levels. The leading configuration of this state makes up only 54% of the MRCI wavefunction for this state:
$(\ 54\% \mid 1a_1^2 \cdots 10a_1^2 11a_1^1 12a_1^1 1b_1^2 \cdots 6b_1^2 7b_1^1 1b_2^2 \cdots 6b_2^2 1a_2^2 \cdots 3a_2^2\rangle$
$+\, 6.5\% \mid 1a_1^2 \cdots 11a_1^2 1b_1^2 \cdots 6b_1^2 7b_1^1 1b_2^2 \cdots 6b_2^2 1a_2^2 2a_2^2 3a_2^1 4a_2^1\rangle$
$+\, 4.3\% \mid 1a_1^2 \cdots 10a_1^2 11a_1^1 12a_1^1 1b_1^2 \cdots 6b_1^2 7b_1^1 1b_2^2 \cdots 6b_2^2 1a_2^2 3a_2^2\rangle$
$+\, 1.3\% \mid 1a_1^2 \cdots 11a_1^2 1b_1^2 \cdots 5b_1^2 6b_1^1 7b_1^1 8b_1^1 1b_2^2 \cdots 6b_2^2 1a_2^2 \cdots 3a_2^2\rangle$
$+\, 1.2\% \mid 1a_1^2 \cdots 10a_1^2 11a_1^1 12a_1^1 1b_1^2 \cdots 5b_1^2 7b_1^1 8b_1^2 1b_2^2 \cdots 6b_2^2 1a_2^2 \cdots 3a_2^2\rangle)$.
At the MRCI and MRCI+Q levels of theory, the third lowest energy state a triply bridging the $^2\mathrm{B}_2$ state, 2.105 eV above the ground state. The leading configuration of this state is an excited configuration: 70% $\mid 1a_1^2 \cdots 11a_1^2 12a_1^1 1b_1^2 \cdots 6b_1^2 7b_1^1 1b_2^2 \cdots 6b_2^2 1a_2^2 2a_2^2 3a_2^1\rangle$.

State	Nb-Nb (Å)	Nb-Nb′ (Å)	Nb-C (Å)	Nb′-N (Å)	Nb′-Nb-Nb-N (°)	ΔE_{CASSCF} (eV)	ΔE_{MRCI} (eV)	ΔE_{MRCI+Q} (eV)
$^2B_1$	2.82	2.48	1.92	2.46	92.2	0.000	0.000	0.000
$^4B_1$	2.84	2.62	1.91	2.52	88.5	1.125	1.272	1.336
$^2B_2$	2.61	2.66	1.97	2.12	63.3	2.655	2.305	2.105
$^4A_1$	2.88	2.85	1.92	2.76	89.8	1.716	2.449	2.527
$^4A_2$	2.84	2.79	1.92	2.59	83.4	2.094	2.505	2.527
$^4B_2$	2.48	2.86	1.96	2.38	65.1	2.450	2.618	2.527
$^2A_1$	2.92	2.55	1.93	2.39	87.3	1.048	2.924	3.356
$^2A_2$	2.84	2.54	2.92	2.40	86.6	1.152	3.242	3.820
$^6A_1$	2.73	2.79	1.88	2.90	97.5	1.657		
$^8A_2$	2.87	2.84	2.06	2.08	57.7	1.885		
$^6A_2$	2.76	3.17	1.87	3.20	93.8	1.941		
$^6B_1$	2.77	3.02	1.89	3.04	93.2	2.170		
$^6B_2$	2.89	2.77	1.93	2.50	81.0	2.199		
$^8A_1$	2.87	2.84	1.93	2.59	81.3	2.636		
$^8B_1$	2.81	2.94	1.90	2.85	88.2	3.036		
$^8B_2$	2.76	3.36	1.89	3.42	94.9	4.750		

Table 2.10: CASSCF geometric parameters and relative energies of electronic states of Nb_3N_2 at the CASSCF, MRCI and MRCI+Q levels.

B3LYP/srsc geometries and relative energies are presented in Table 2.11. The ground state was found to be a ^{2}B$_2$ state, however, the geometry and harmonic vibrational frequencies of this state closely match those of the ^{2}B$_1$ ground state calculated by Yang. These two representations are interchangeable by swapping the x and y axes, subsequently the different labelling of these two states is due to differing molecule orientation with respect to the cartesian axes. Other states lie significantly higher in energy.
The configuration of the ^{2}B$_2$ state is
$1a_1^2 \cdots 11a_1^2 1b_1^2 \cdots 5b_1^2 1b_2^2 \cdots 6b_2^2 7b_2^1 1a_2^2 \cdots 3a_2^2$.
The ^{2}B$_1$ state found in this study is a transition state 1.18 eV above the ground state with an excited electronic configuration of
$1a_1^2 \cdots 11a_1^2 12a_1^1 1b_1^2 \cdots 6b_1^2 1b_2^2 \cdots 6b_2^2 7b_2^1 1a_2^2 2a_2^2 3a_2^1$.
These configurations equal the MRCI leading configurations of the ^{2}B$_1$ and ^{2}B$_2$ states respectively, supporting the assertion that the DFT calculations used an axis system with the x and y axes reversed.

Given this caveat, the B3LYP calculations produce the same picture as the CASSCF and MRCI calculations, with a doubly bridged ^{2}B ground state with a large ΔE separating it from the ^{2}A$_1$, next lowest energy state. Both DFT and CASSCF predict the ^{6}A$_1$ state to be relatively low in energy (cf. 1.657 eV CASSCF and 1.18 eV B3LYP). Overall, the DFT calculations predict ΔE figures within a lower range than that of the CASSCF calculations (2.75 vs. 4.750 eV), this could be partially explained as an artifact of the small restricted active space used permiting only limited excitations from the leading configurations of high-spin states.

Other notable features from both levels of theory are that all states with ΔE ≤ 1 eV have Nb$'$-Nb-Nb-N dihedral angles $\approx 90^\circ$ or greater and there are very few triply bridging geometries predicted. The lowest energy triply bridging state at the B3LYP/srsc level is the ^{4}A$_1$ state, some 1.16 eV above the ground state, at the CASSCF level the ^{8}A$_2$, ^{4}B$_2$ and ^{2}B$_2$ states possess triply bridging geometries , though only the ^{2}B$_2$ state was investigated at MRCI level yielding a ΔE of 2.105 eV.

State	Nb-Nb (Å)	Nb-Nb′ (Å)	Nb-N (Å)	Nb′-N (Å)	Nb′-Nb-Nb-N (°)	ΔE (eV)	$\bar{\nu}$ (cm^{-1})
$^2B_2$	2.84	2.42	1.95	2.46	94.9	0.00	143,236,245,321,371,436,610,669,760
$^2A_1$	3.00	2.46	1.96	2.29	87.9	0.64	232,263,309,353,387,387,628,669,767
$^4B_2$	2.62	2.68	1.92	3.11	109.3	0.85	82,123,205,287,336,410,598,741,796
$^4B_1$	2.74	2.58	1.93	2.84	103.8	0.94	413i,129,203,295,304,387,590,706,780
$^4A_1$	2.84	2.56	2.04	2.00	64.6	1.16	140i,183,211,285,351,414,457,584,790
$^6A_1$	2.76	2.73	1.92	2.94	101.9	1.18	40,140,196,265,393,432,607,710,813
$^2B_1$	2.40	2.75	2.07	1.97	52.3	1.18	89i,14,271,274,342,350,492,568,751
$^2A_2$	2.74	2.52	1.94	2.73	101.0	1.22	127i,186,212,317,374,375,546,699,765
$^4A_2$	2.50	2.76	1.94	3.30	111.3	1.24	101i,147,262,287,320,394,526,746,758
$^6A_2$	2.94	2.63	1.94	2.44	85.4	1.44	309i,169,179,244,339,473,487,632,779
$^6B_2$	3.08	2.55	2.05	2.04	71.0	1.50	148i,96,187,215,357,371,381,573,763
$^6B_1$	2.39	2.91	2.13	1.94	46.7	1.76	93i,127,218,220,358,409,484,622,740
$^8B_2$	2.73	3.01	1.91	3.23	101.8	2.29	102i,81,135,198,389,501,717,739,800
$^8B_1$	2.82	2.83	2.05	2.05	56.6	2.50	182,182,318,338,338,347,348,570,736
$^8A_1$	2.45	2.99	2.07	2.06	49.1	2.65	65i,98,185,237,288,304,381,564,722
$^8A_2$	2.86	2.74	2.01	2.13	63.5	2.75	215,266,273,314,345,424,437,599,757

Table 2.11: Geometric parameters, relative energies and vibrational frequencies of Nb_3N_2 at the B3LYP/srsc level.

2.2.2 $Nb_3N_2^+$

Using the same active space, cationic states of $Nb_3N_2^+$ up to the septet were investigated. CASSCF geometries and relative energies are presented in Table 2.12. The ground state is predicted to be the $^1A_1$ state. The MRCI wavefunction of this state is highly multireference with three major configurations:

$(59\% \mid 1a_1^2 \cdots 11a_1^2 1b_1^2 \cdots 6b_1^2 1b_2^2 \cdots 6b_2^2 1a_2^2 \cdots 3a_2^2\rangle$
$+ 5\% \mid 1a_1^2 \cdots 10a_1^2 1b_1^2 \cdots 7b_1^2 1b_2^2 \cdots 6b_2^2 1a_2^2 \cdots 3a_2^2\rangle$
$+ 2\% \mid 1a_1^2 \cdots 11a_1^2 1b_1^2 \cdots 6b_1^2 1b_2^2 \cdots 6b_2^2 1a_2^2 2a_2^2 4a_2^2\rangle)$

and several minor configurations resulting from double excitations of the leading wavefunction.

At this level, the assignment of the ground state is unambiguous with the next lowest energy states being the $^3B_1$ and $^1B_1$ states lying 0.623 and 0.633 eV respectively above the $^1A_1$ ground state. Similar to the neutral species, the majority of states have a doubly bridging geometry. The lowest energy triply bridging geometry is the $^5A_1$, 1.504 eV above the ground state at CASSCF level.

State	Nb-Nb (Å)	Nb-Nb′ (Å)	Nb-C (Å)	Nb′-N (Å)	Nb′-Nb-Nb-N (°)	ΔE_{CASSCF} (eV)	ΔE_{MRCI} (eV)	ΔE_{MRCI+Q} (eV)
$^1A_1$	2.81	2.49	1.91	2.44	90.8	0.000	0.000	0.000
$^3B_1$	2.86	2.50	1.92	2.37	87.9	0.599	0.619	0.623
$^1B_1$	2.88	2.61	1.91	2.40	84.4	0.741	0.673	0.633
$^3B_2$	2.72	2.60	1.96	2.12	67.3	1.592	1.401	1.274
$^3A_1$	2.77	2.82	1.87	2.71	86.8	1.364	1.405	1.392
$^1B_2$	2.80	2.60	1.91	2.50	87.4	1.472	1.409	1.368
$^3A_2$	2.86	2.68	1.90	2.51	86.0	1.742	1.702	1.679
$^1A_2$	2.93	2.55	1.98	2.14	74.0	2.621	2.523	2.394
$^5B_1$	2.84	2.73	1.90	2.57	85.9	1.504		
$^5A_1$	2.99	2.61	2.09	1.95	62.3	1.509		
$^5B_2$	2.79	2.98	1.89	2.98	92.7	2.123		
$^7B_1$	2.54	3.26	1.92	2.74	65.7	2.175		
$^5A_2$	2.87	2.65	1.95	2.25	73.4	2.736		
$^7B_2$	2.65	2.89	2.00	2.17	57.5	3.190		
$^7A_1$	2.87	2.77	1.98	2.18	65.0	3.272		
$^7A_2$	2.78	3.26	1.89	3.28	93.2	4.269		

Table 2.12: CASSCF geometric parameters and relative energies of electronic states of $Nb_3N_2^+$ at the CASSCF, MRCI and MRCI+Q levels.

The ground state predicted by B3LYP/srsc is also a $^1A_1$ state. The geometry of this state is in agreement with both the CASSCF geometry and the B3P86/Lanl2dz geometry of Yang. The harmonic vibrational frequencies calculated for this state also agree closely with those of Yang. The electronic configuration of this state is
$1a_1^2 \cdots 11a_1^2 1b_1^2 \cdots 6b_1^2 1b_2^2 \cdots 6b_2^2 1a_2^2 \cdots 3a_2^2$,
which concurs with the leading configuration of the $^1A_1$CASSCF wavefunction.

As was observed for the neutral species, the DFT ΔE values are smaller than the ΔE values predicted at the CASSCF and MRCI levels with four states possessing ΔE values $<$ 0.5 eV. The second lowest energy state is a $^1B_2$ transition state at 0.10 eV, followed by $^3B_1$ and $^1B_1$ minima with ΔE values of 0.40 and 0.51 eV respectively.

State	Nb-Nb (Å)	Nb-Nb′ (Å)	Nb-N (Å)	Nb′-N (Å)	Nb′-Nb-Nb-N (°)	ΔE (eV)	$\bar{\nu}$ (cm^{-1})
$^1A_1$	2.79	2.44	1.94	2.50	94.2	0.00	97,218,226,309,377,474,629,698,789
$^1B_2$	2.94	2.50	1.95	2.33	86.7	0.10	137i,222,304,350,358,374,492,647,794
$^3B_1$	2.84	2.52	2.00	2.09	70.9	0.40	59,150,182,198,336,376,399,675,796
$^1B_1$	2.81	2.53	1.99	2.11	70.6	0.51	77,97,155,240,321,366,514,666,798
$^3A_2$	2.53	2.72	1.97	2.16	62.0	0.54	139i,206,253,285,345,387,498,668,803
$^3B_2$	2.71	2.61	2.03	1.99	60.8	0.63	77i,152,206,278,367,455,501,597,806
$^5A_1$	2.98	2.57	2.04	2.02	67.4	0.93	127i,198,215,332,366,378,441,621,787
$^5B_1$	2.86	2.64	1.94	2.30	76.1	0.96	147,201,208,222,349,442,545,654,773
$^1A_2$	2.36	2.85	2.11	1.90	47.2	1.10	124,277,371,386,514,522,650,777,964
$^5B_2$	2.71	2.81	1.90	3.02	101.6	1.12	87i,70,203,234,400,465,647,747,844
$^7B_2$	2.74	2.89	1.90	3.09	101.4	1.87	304i,96,170,232,386,399,542,727,837
$^7A_1$	2.44	2.98	2.04	2.09	50.1	1.92	92i,126,223,250,334,342,370,594,755
$^5A_2$	2.71	2.91	1.89	3.11	101.0	1.95	118i,110,154,235,268,396,580,743,849
$^7A_2$	2.93	2.69	2.02	2.12	66.4	2.19	379i,213,246,329,356,402,451,567,767
$^7B_1$	2.56	2.88	2.12	1.93	48.4	2.46	284i,234,239,305,371,409,519,763,890
$^3A_1$	3.67	2.53	2.04	2.29	117.5	3.64	170i,123,186,249,383,417,424,551,707

Table 2.13: Geometric parameters, relative energies and vibrational frequencies of $Nb_3N_2^+$ at the B3LYP/srsc level.

2.2.3 IP Calculations

Yang *et al.* conducted photoionisation efficiency experiments and ZEKE on Nb_3N_2, yielding an accurate IP of 5.44 ± 0.05 eV. The previous section (2.1.3) on the pure Nb_3 cluster indicated that a basis set including f functions on the niobium atoms improved the IP prediction by ≈0.25 eV, however little further improvement was seen on increasing the size of the basis set above triple-ζ quality. Therefore, a triple-ζ basis was chosen for the niobium atoms without further consideration and the effect of the nitrogen basis set was investigated. The only previous multireference studies undertaken on mixed metal / second row clusters have been undertaken on carbide species. In his study of low-lying electronic states of NbC [121], Balasubramanian used a $5s3p3d2f$ basis set for the niobium atom and a $4s4p2d1f$ basis set to describe the carbon atom. Using this as a guide to the quality of basis set required, single point calculations were undertaken on the neutral and cationic ground states using a triple-ζ basis $(12s,7p,3d,1f//6s,5p,3d,1f)$ [122] on the nitrogen atoms, with the previously established $(10s9p8d2f1g//5s5p4d2f1g)$ basis set used on the niobium atoms. The calculated IPs are presented in Table 2.14. IPs are calculated as the ΔE between the respective ground states of the neutral and cation (i.e. are adiabatic IPs). Thus, MRCI IPs are calculated as the $^2B_1 \rightarrow {}^1A_1$ transition, whereas the B3LYP/srsc IP is calculated as the $^2B_2 \rightarrow {}^1A_1$ transition.

The combinations of basis sets used had very little effect on the IP predicted. Similar to the bare Nb_3 case, the addition of unlinked quadruple excitations increased the calculated IP value by ≈ 0.3 eV to 4.8 eV, however the resultant values are still ≈0.6 eV below the experimental value. B3LYP/srsc predicts an IP of 5.672 eV.

	Calculated Transition	IP
srsc (Nb), cc-pVDZ (N)		
MRCI	$^2B_1 \rightarrow ^1A_1$	4.549
MRCI+Q		4.796
cc-pVTZ (Nb), cc-pVDZ (N)		
MRCI		4.511
MRCI+Q		4.800
cc-pVTZ (Nb), cc-pVTZ (N)		
MRCI		4.510
MRCI+Q		4.803
cc-pVTZ (Nb) aug-cc-pVTZ (N)		
MRCI		4.513
B3LYP/srsc	$^2B_2 \rightarrow ^1A_1$	5.672
Experiment		5.44 ± 0.05

Table 2.14: Ionisation Potential of Nb_3N_2 calculated using basis sets of increasing quality. All values are in eV. Experimental IP taken from reference [116].

2.3 Nb_3C_2

2.3.1 Nb_3C_2

Nb_3C_2 and $Nb_3C_2^+$ have had their vibrational spectra recorded using (PFI)-ZEKE [21]. DFT (B3P86/Lanl2dz) calculations undertaken in the same paper by Yang *et al.* proposed two possible structures for Nb_3C_2, a triply bridging (TB) and a doubly bridging structure (DB). Their DFT calculations suggested that these structures were degenerate in the neutral species, however, in the cationic species the trigonal bipyramid was almost 1 eV lower in energy. On this basis and by employing simulated spectra they suggest a D_{3h} singlet cation and a C_{2v} triply bridging doublet neutral. It was hoped that more detailed investigation at the CASSCF and MRCI levels of theory would support the assignment of Yang and provide more information on the low-lying excited states of these species.

The full valence active space of Nb_3C_2 and $Nb_3C_2^+$ includes 40 orbitals, ($16a_1$, $5a_2$, $6b_1$, $13b_2$). Using this complete active space leads to too large a number of Configuration Spin Functions (CSFs), therefore, in order to make the calculations tractable, a reduced active space was employed. The niobium $4s$ and $4p$ and carbon $1s$ orbitals ($6a_1$, $1a_2$, $4b_1$, $3b_2$) were considered to be always doubly occupied (closed). The active space of the remaining 26 orbitals was still too large to be tractable so to determine the optimal reduced active space, preliminary CASSCF calculations were undertaken with a large active space. Orbitals that were doubly occupied in all configurations were considered closed and high energy orbitals that were not occupied in any configurations were removed from the active space. The resultant active space considered the lowest $9a_1$, $2a_2$, $5b_1$ and $5b_2$ orbitals to be closed and included the next $4a_1$, $1a_2$, $3b_1$ and $2b_2$ orbitals as the active space. 9 electrons, (8 in the case of $Nb_3C_2^+$) electrons were placed in the active space. No excitations were allowed from the closed orbitals, however, they were allowed to relax. This approach led to a total of 7000 CSFs being included. All calculations were undertaken in C_{2v} symmetry using the Stuttgart RSC basis set and associated ECP on niobium atoms and cc-pVDZ on carbon atoms.

The same methodology used for investigation of the Nb_3N_2 cluster was followed . Briefly, full geometry optimisations of each electronic state up to the octet were undertaken at the CASSCF level and the lowest two multiplicities of the neutral and cation were followed by single point MRCI calculations. All CASSCF configurations with absolute coefficients of $\geq$0.05 were included as reference configurations. Calculations were undertaken in C_{2v} symmetry using the Stuttgart RSC basis set and associated ECP on niobium atoms and cc-pVDZ on carbon atoms.

Frequency calculations were undertaken using DFT optimised geometries of each electronic symmetry. DFT calculations were undertaken using Gaussian 03 [78] and employed the B3LYP functional with the Stuttgart basis set and associated ECPs for niobium atoms and D95V for carbon atoms. As in the CASSCF calculations, all geometries were constrained to C_{2v} symmetry.

The CASSCF calculated geometries and energy separations for electronic states of Nb_3C_2 are shown in Table 2.15. Structures with a Nb′-Nb-Nb-C dihedral angle less than 70° result in triply bridging carbon atoms, dihedral angles larger than 70° position the carbon atoms closer to the Nb-Nb bond (stretching the Nb′-C bond) and are subsequently doubly bridging structures. Both triply and doubly bridged structures were located for the $^2A_1$ state, the $^2A_2$ and $^2B_2$ states possess doubly bridging structures, while the $^2B_1$ state is triply bridging. All levels of theory agree in predicting the global minimum to be the triply bridging $^2A_1$ state. At the CASSCF level, the $^2B_1$ (triply bridging) and $^2A_2$ (doubly bridging) states lie a mere 0.048 and 0.072 eV respectively, above the ground state. The doubly bridging $^2A_1$ structure is 1.045 eV above the ground state at the CASSCF level, however at the MRCI level, the relative energy drops to 0.494 eV and at the MRCI+Q level it is only 0.287 eV above the ground state. Both the MRCI and MRCI+Q levels of theory suggest doubly bridging structures with energies $\approx$

0.3 and 0.5 eV above the ground state, however at MRCI level E(^{2}A$_2$) $<$ E(^{2}A$_1$) whereas MRCI+Q predicts the reverse.

The MRCI wavefunction of the triply bridging ^{2}A$_1$ state has three dominant configurations
$(68\% \mid 1a_1^2 \cdots 11a_1^2 12a_1^1 1b_1^2 \cdots 6b_1^2 1b_2^2 \cdots 6b_2^2 1a_2^2 2a_2^2\rangle$
$+ 1.6\% \mid 1a_1^2 \cdots 10a_1^2 12a_1^1 1b_1^2 \cdots 6b_1^2 8b_1^2 1b_2^2 \cdots 6b_2^2 1a_2^2 2a_2^2\rangle$
$+ 1.4\% \mid 1a_1^2 \cdots 11a_1^2 12a_1^1 1b_1^2 \cdots 5b_1^2 7b_1^2 1b_2^2 \cdots 6b_2^2 1a_2^2 2a_2^2\rangle)$.
The doubly bridging ^{2}A$_1$ state, on the other hand, has only two dominant configurations:
$(67\%| 1a_1^2 \cdots 10a_1^2 11a_1^1 1b_1^2 \cdots 6b_1^2 1b_2^2 \cdots 6b_2^2 1a_2^2 \cdots 3a_2^2\rangle$
$+ 3\% \mid 1a_1^2 \cdots 9a_1^2 11a_1^1 1b_1^2 \cdots 7b_1^2 1b_2^2 \cdots 6b_2^2 1a_2^2 \cdots 3a_2^2\rangle)$.
Both the ^{2}A$_2$ and ^{2}B$_1$ states are highly multireference, the wavefunction of the ^{2}B$_1$ being comprised of
$(67\% \mid 1a_1^2 \cdots 11a_1^2 1b_1^2 \cdots 6b_1^2 7b_1^1 1b_2^2 \cdots 6b_2^2 1a_2^2 2a_2^2\rangle$
$+ 1.2\% 1a_1 \cdots 10a_1^2 12a_1^2 1b_1^2 \cdots 6b_1^2 7b_1^1 1b_2^2 \cdots 6b_2^2 1a_2^2 2a_2^2\rangle$
$+ 1.1\% \mid 1a_1^2 \cdots 11a_1^2 1b_1^2 \cdots 5b_1^2 7b_1^1 8b_1^2 1b_2^2 \cdots 6b_2^2 1a_2^2 2a_2^2\rangle$
$+ 1\% \mid 1a_1 \cdots 9a_1^2 10a_1^1 11a_1^2 13a_1^1 1b_1^2 \cdots 6b_1^2 7b_1^1 1b_2^2 \cdots 6b_2^2 1a_2^2 2a_2^2\rangle)$,
the ^{2}A$_2$ wavefunction has eight configurations that contribute more than 1% to the total wavefunction. The contributions of these configurations, that represent excitations from the leading configuration, contribute to the high energy of this state at MRCI ad MRCI+Q levels. The ^{2}B$_2$ state is even higher in energy at the MRCI and MRCI+Q levels, the leading configuration of the wavefunction for this state is an excited state, with three unpaired electrons (two of which are of opposite spin):
$63\% \mid 1a_1^2 \cdots 10a_1^2 11a_1^1 1b_1^2 \cdots 6b_1^2 7b_1^1 1b_2^2 \cdots 6b_2^2 1a_2^2 2a_2^2 3a_2^1\rangle$.
Searches for a triply bridging ^{2}B$_2$ minimum were unsuccessful.

Sextet and octet structures were found to lie high in energy at the CASSCF level and were not investigated at the MRCI or MRCI+Q levels of theory.

State	Nb-Nb (Å)	Nb-Nb′ (Å)	Nb-C (Å)	Nb′-C (Å)	Nb′-Nb-Nb-C (°)	ΔE_{CASSCF} (eV)	ΔE_{MRCI} (eV)	ΔE_{MRCI+Q} (eV)
$^2A_1$ (TB)	2.52	2.62	2.06	2.02	59.1	0.000	0.000	0.000
$^2B_1$	2.70	2.54	2.02	2.14	68.8	0.048	0.056	0.102
$^2A_1$ (DB)	2.87	2.48	1.96	2.38	87.7	1.045	0.494	0.287
$^2A_2$	2.77	2.63	1.93	2.55	87.1	0.072	0.285	0.504
$^2B_2$	2.83	2.66	1.95	2.43	81.2	0.675	0.744	0.865
$^4B_1$	2.77	2.75	1.92	2.54	81.1	1.430	1.209	1.179
$^4A_1$	2.47	2.79	2.12	1.98	52.0	0.858	1.164	1.252
$^4A_2$	3.08	2.47	2.00	2.30	89.0	2.325	1.893	1.691
$^4B_2$	2.50	2.60	2.13	2.13	62.7	3.324	3.346	3.161
$^6A_2$	2.73	2.91	1.91	2.70	80.6	1.353		
$^6B_2$	2.87	2.62	2.10	2.04	63.6	1.911		
$^8A_2$	2.77	2.88	1.94	2.56	75.6	2.130		
$^6A_1$	2.76	2.72	2.01	2.25	68.1	2.564		
$^8B_1$	2.76	3.08	1.93	2.88	81.8	2.829		
$^8B_2$	2.66	2.84	2.10	2.01	53.2	3.617		
$^8A_1$	2.87	2.96	1.99	2.46	68.8	4.068		
$^6B_1$	2.90	3.08	1.97	2.56	69.1	4.246		

Table 2.15: CASSCF geometric parameters and relative energies of electronic states of Nb_3C_2 at the CASSCF, MRCI and MRCI+Q levels.

The B3LYP/sdd geometries of Nb_3C_2 are shown in Table 2.16. Like the previous B3P86/Lanl2dz calculations, doubly and triply bridging structures are found to be almost degenerate, with a triply bridging structure being lower in energy. In contrast to the previous calculations, the global minimum was found to have $^2B_2$ electronic symmetry. The geometry of this state, however, agrees very closely with the geometry presented by Yang *et al.* for their $^2A_1$ global minimum. Searching for a triply bridging $^2A_1$ state uncovered a transition state, whose geometry differs from the $^2B_2$ state by having one short Nb-Nb bond and two long. The energies of these two states are separated by only 1×10^{-5} hartree, suggesting that they represent Jahn-Teller components of a D_{3h} structure. The harmonic frequencies of these states are very similar, further supporting this assertion. It is possible that the use of a different functional and basis set could change the assignment of these two species. The doubly bridging $^2A_1$ structure was found to be a minimum and lies 0.08 eV above the $^2B_2$ global minimum, which is comparable with the ΔE of 0.02 eV quoted by Yang.

The B3LYP/srsc wavefunction of the triply bridging $^2A_1$ state was found to be
$1a_1 \cdots 11a_1^2 12a_1^1 1b_1^2 \cdots 6b_1^2 1b_2^2 \cdots 6b_2^2 1a_2^2 2a_2^2$
whereas the wavefunction of the$^2A_1$ doubly bridging structure is
$1a_1 \cdots 10a_1^2 11a_1^1 1b_1^2 \cdots 6b_1^2 1b_2^2 \cdots 6b_2^2 1a_2^2 \cdots 3a_2^2$.
Both of these wavefunctions are consistent with the leading configurations of the respective MRCI wavefunctions. The B3LYP/srsc wavefunction of the $^2B_2$ global minimum is
$1a_1 \cdots 11a_1^2 1b_1^2 \cdots 6b_1^2 1b_2^2 \cdots 6b_2^2 7b_2^1 1a_2^2 2a_2^2$,
which is quite different from the excited MRCI configuration (viz.
63% $\mid 1a_1^2 \cdots 10a_1^2 11a_1^1 1b_1^2 \cdots 6b_1^2 7b_1^1 1b_2^2 \cdots 6b_2^2 1a_2^2 2a_2^2 3a_2^1 \rangle$)
and accounts for the lower ΔE predicted at this level of theory.

All doublet states were found to lie within 0.32 eV of the global minimum. The lowest energy quartet was found to be the $^4B_1$ state, with a geometry intermediate between doubly and triply bridging structures (Nb-C = 2.01 Å and Nb′-C = 2.28 Å). This state was found to be only 0.23 eV above the global minimum, however, all other quartets were found to be ≥ 0.5 eV above the doublet states. Sextet and octet states were universally high in energy, with the ΔE of sextet states ranging from 1.55 eV to 1.86 eV and octet states having ΔE values of 2.44 eV to 2.99 eV.

State	Nb-Nb (Å)	Nb-Nb′ (Å)	Nb-C (Å)	Nb′-C (Å)	Nb′-Nb-Nb-C (°)	ΔE (eV)	$\bar{\nu}$ (cm^{-1})
$^2B_2$ (TB)	2.66	2.53	2.08	2.07	65.0	0.00	33,220,233,248,357,509,514,683,801
$^2A_1$	2.49	2.61	2.07	2.08	61.0	0.00	25i,233,237,259,358,508,514,685,801
$^2A_1$ (DB)	2.88	2.48	1.99	2.44	90.0	0.08	187,234,251,338,362,457,374,704,800
$^4B_1$	2.92	2.50	2.01	2.28	81.4	0.23	147,208,225,271,357,468,622,657,781
$^2A_2$	2.69	2.53	2.04	2.14	68.8	0.29	210i,143,167,269,343,365,455,741,797
$^2B_1$	2.51	2.63	2.10	2.03	58.8	0.32	164i,233,293,336,358,505,524,743,801
$^4A_2$	2.80	2.67	1.95	2.57	85.7	0.80	213i,186,202,319,347,554,706,756,827
$^4B_2$	2.75	2.58	2.06	2.12	66.9	1.09	224i,135,214,328,368,402,473,548,781
$^4A_1$	2.45	2.79	2.12	2.01	53.0	1.27	275i,192,201,239,289,347,507,772,853
$^6B_1$	2.84	2.62	2.00	2.29	75.1	1.55	49,210,218,251,348,475,602,654,787
$^6A_1$	2.46	2.88	2.09	2.08	53.2	1.59	13,33,148,237,326,339,411,602,752
$^6B_2$	2.96	2.66	2.12	2.00	61.8	1.77	203i,177,227,265,290,304,453,589,775
$^6A_2$	2.98	2.54	2.03	2.25	78.6	1.86	399i,184,211,283,336,442,456,621,760
$^8B_2$	2.78	2.78	2.08	2.08	58.8	2.44	141,142,260,262,277,278,306,599,748
$^8B_1$	3.34	2.72	2.15	2.00	65.1	2.87	167i,124,260,328,376,407,414,535,736
$^8A_2$	2.56	3.03	2.08	2.10	49.6	2.92	144,155,203,283,350,435,493,536,700
$^8A_1$	2.58	2.93	2.06	2.17	55.4	2.99	59i,58,198,272,280,280,349,570,744

Table 2.16: Geometric parameters, relative energies and vibrational frequencies of Nb_3C_2 at the B3LYP/sdd level.

2.3.2 $Nb_3C_2^+$

The geometries and electronic states of $Nb_3C_2^+$ were studied at the CASSCF and DFT levels. MRCI single point energy calculations were undertaken on the CASSCF geometries for the singlet and triplet states. The CASSCF geometries and relative energy separations are shown in Table 2.17, DFT geometries, relative energies and frequencies are shown in Table 2.18.

The ground state is predicted to be $^1A_1$ at all levels of theory. The CASSCF geometry is a triply bridging geometry with a Nb-Nb′-Nb angle of 58.8° with an Nb-Nb bondlength of 2.55Å and two Nb-Nb′ bondlengths of 2.60Å. The shortening of the Nb-Nb bond, relative to a D_{3h} ideal, also shortens the Nb-C bonds from 2.07Å to 2.02Å. Attempts to converge a D_{3h} geometry were unsuccessful. The distortion of this geometry from ideal D_{3h} symmetry is likely to be an artifact of the restricted active space chosen as the preliminary CASSCF geometry optimisation on this state, which closed only the niobium $4s$ and $4p$ and carbon $1s$ orbitals ($6a_1$, $1a_2$, $4b_1$, $3b_2$) yielded a geometry only slightly perturbed from D_{3h} (Nb-Nb′-Nb = 60.0°, Nb-Nb = Nb-′ = 2.60Å, Nb-C = 2.05Å, Nb′-C = 2.04Å). The MRCI wavefunction of this state is:

$(70\%|\, 1a_1^2 \cdots 11a_1^2 1b_1^2 \cdots 6b_1^2 1b_2^2 \cdots 6b_2^2 1a_2^2 2a_2^2\rangle$

$+\, 1.9\% \mid 1a_1^2 \cdots 10a_1^2 12a_1^2 1b_1^2 \cdots 6b_1^2 1b_2^2 \cdots 6b_2^2 1a_2^2 2a_2^2\rangle$

$+\, 1\% \mid 1a_1^2 \cdots 10a_1^2 11a_1^1 12a_1^1 1b_1^2 \cdots 6b_1^2 1b_2^2 \cdots 5b_2^2 6b_2^1 7b_2^1 1a_2^2 2a_2^2\rangle$

$+\, 1\% \mid 1a_1^2 \cdots 11a_1^2 1b_1^2 \cdots 6b_1^2 1b_2^2 \cdots 5b_2 7b_2^2 1a_2^2 2a_2^2\rangle$

$+\, 1\% \mid 1a_1^2 \cdots 10a_1^2 11a_1^1 12a_1^1 1b_1^2 \cdots 6b_1^2 1b_2^2 \cdots 5b_2^2 6b_2^1 7b_2^1 1a_2^2 2a_2^2\rangle)$

Significantly, no doubly bridging geometry could be found for this state, all attempts converged to the triply bridging geometry already discussed.

State	Nb-Nb (Å)	Nb-Nb′ (Å)	Nb-C (Å)	Nb′-C (Å)	Nb′-Nb-Nb-C (°)	$\Delta E_{\mathrm{CASSCF}}$ (eV)	ΔE_{MRCI} (eV)	$\Delta E_{\mathrm{MRCI+Q}}$ (eV)
$^1A_1$ (TB)	2.55	2.60	2.02	2.07	62.7	0.000	0.000	0.000
$^3A_2$	2.74	2.71	1.92	2.45	78.6	0.173	0.481	0.674
$^3B_1$	2.45	2.80	2.14	1.92	49.6	0.345	0.838	0.979
$^1A_2$	2.83	2.62	1.96	2.38	80.1	0.677	0.989	1.061
$^3A_1$	2.67	2.78	1.94	2.40	71.5	0.641	1.051	1.222
$^1B_1$	2.84	2.64	1.96	2.33	77.1	0.696	1.105	1.252
$^1B_2$	2.59	2.79	2.02	2.16	59.7	1.805	2.162	2.130
$^3B_2$	3.02	2.54	1.97	2.31	85.3	2.082	1.969	1.734
$^5B_2$	2.83	2.66	1.95	2.41	80.1	1.318		
$^5A_2$	2.73	2.86	1.92	2.58	77.2	1.338		
$^7A_2$	2.71	3.06	1.92	2.77	76.5	1.723		
$^7A_1$	2.75	3.12	1.91	3.04	86.8	2.039		
$^5B_1$	2.77	2.77	1.95	2.40	73.7	2.125		
$^5A_1$	2.86	2.83	2.05	2.11	59.4	2.185		
$^7B_1$	2.95	2.99	2.01	2.23	59.3	3.239		
$^7B_2$	2.90	3.07	2.01	2.30	59.3	4.230		

Table 2.17: Geometric parameters and relative energies of electronic states of $Nb_3C_2^+$ at the CASSCF, MRCI and MRCI+Q levels.

A ^{1}A$_1$ state is also predicted to be the ground state at the B3LYP/srsc level of theory. The geometry for this state is in good agreement with the B3P86/Lanl2dz geometry gained by Yang, slightly lengthening all bondlengths (viz. The Nb-Nb bonds are lengthened from 2.54Å to 2.57Å and the Nb-C bonds from 2.06Å to 2.07Å). The harmonic vibrational frequencies are also in good agreement with the B3P86/Lanl2dz results, with the B3LYP/sdd frequencies indicating three degenerate vibrations, supporting an assignment of D_{3h} symmetry. The 232 / 235 cm^{-1} frequencies are the two components of the degenerate Nb-C asymmetric stretch with e'' symmetry, the 265 cm^{-1} frequencies correspond to components of the Nb-Nb symmetric stretch with e' symmetry and the 531 / 533 cm^{-1} frequencies represent components of the symmetric Nb-C stretch of e' symmetry. Constraint of the ^{1}A$_1$ geometry to D_{3h} symmetry at the DFT level resulted in a ^{1}A$'_1$ state with the same energy as the ^{1}A$_1$ (C_{2v}) state. In D_{3h} symmetry, addition of an electron to form the neutral would populate a degenerate e' orbital resulting in lowered symmetry of the neutral due to Jahn-Teller distortion.

The assignment of the ^{1}A$_1$ ground state is quite unambiguous with no states lying close in energy to the global minimum; the next lowest energy structure being a doubly bridging ^{3}A$_2$ state, 0.70 eV above the ground state. The ^{1}A$_2$ state is also doubly bridging and lies 0.87 eV above the ground state, very close in energy to the doubly bridging ^{1}A$_1$ state. The only other structure with a ΔE below 1 eV is a ^{3}B$_2$ transition state was found to lie 0.98 eV above the ground state. Quintet and septet structures were found to lie 1.67 - 3.17 eV above the ^{1}A$_1$ ground state.

State	Nb-Nb (Å)	Nb-Nb′ (Å)	Nb-C (Å)	Nb′-C (Å)	Nb′-Nb-Nb-C (°)	ΔE (eV)	$\bar{\nu}$ (cm^{-1})
$^1A_1$ (TB)	2.56	2.56	2.07	2.07	63.0	0.00	232,235,265,265,359,531,533,716,811
$^3A_2$	2.82	2.57	1.98	2.34	79.8	0.70	178,207,229,260,370,486,674,675,810
$^1A_2$	2.83	2.54	1.99	2.29	78.1	0.87	193,217,221,273,283,367,622,665,803
$^1A_1$ (DB)	2.94	2.48	1.99	2.34	86.6	0.88	174,178.232.362.398.406,660,687,816
$^3B_2$	2.82	2.53	2.06	2.10	68.9	0.98	291i,160,232,300,344,424,462,610,789
$^3B_1$	2.32	2.89	2.16	1.95	47.3	1.11	315i,33,188,258,386,440,655,673,809
$^1B_1$	2.31	2.90	2.17	1.95	47.0	1.16	307i,103,224,259,389,398,645,678,811
$^1B_2$	2.81	2.55	2.05	2.13	69.7	1.17	132i,157,222,328,329,404,480,781,790
$^5B_1$	2.90	2.55	2.02	2.26	77.3	1.67	166i,207,229,278,345,442,568,650,789
$^3A_1$	2.87	2.53	1.98	2.43	86.6	1.77	136,231,252,334,355,379,645,673,812
$^5A_2$	2.75	2.72	1.97	2.39	74.2	2.05	197,212,240,365,372,470,678,681,816
$^5A_1$	2.54	2.82	2.07	2.09	55.7	2.26	289i,194,201,206,314,352,405,701,770
$^5B_2$	2.75	2.66	2.03	2.18	67.0	2.29	112i,148,248,277,356,384,486,775,1414
$^7A_2$	2.82	2.77	2.00	2.32	69.8	2.62	171,178,197,234,326,394,590,645,782
$^7B_1$	2.51	3.03	2.08	2.08	48.7	2.63	123,138,219,302,351,466,516,552,720
$^7A_1$	2.60	2.88	2.07	2.12	55.4	2.87	102,153,212,240,277,303,366,594,758
$^7B_2$	3.21	2.61	2.04	2.24	81.5	3.17	231i,193,288,303,325,464,516,558,710

Table 2.18: Geometric parameters, relative energies and vibrational frequencies of $Nb_3C_2^+$ at the B3LYP/sdd level.

2.3.3 IP Calculations

Yang *et al.* recorded the photoionization efficiency spectrum and ZEKE spectrum of Nb_3C_2 and accurately determined the IP to be 5.039 ±0.05 eV [21]. Adiabatic IPs at the DFT, MRCI and MRCI+Q levels of theory are calculated using the ground state predicted by that level of theory, i.e. the DFT (B3LYP) IP is calculated as the $^2B_2 \rightarrow ^1A_1$ transition and the MRCI and MRCI+Q IPs are calculated as the $^2A_1 \rightarrow ^1A_1$ transition. B3LYP/srsc predicts an IP of 5.126 eV, which agrees closely with the experimental value. The IP of the doubly bridging structure could be calculated as either $^2A_1$ (DB) $\rightarrow$ $^1A_1$ (DB) or $^2A_1$ (DB) $\rightarrow$ $^3A_2$, yielding values of 5.924 and 5.748 eV respectively. It is clear that neither of these values correspond closely with the experimental value, supporting the previous assignment of a triply bridging structure for both neutral and cationic Nb_3C_2. The B3P86 functional used by Yang is known to predict IPs that are 0.3 - 0.7 eV higher than experimentally measured values [123, 124], and their B3P86/Lanl2dz IPs of 5.781 for the triply bridging structure and 6.637 eV for the doubly bridging structure are consistent with this observation.

As there was no benefit observed by increasing the quality of the basis set for Nb_3N_2, the MRCI values presented are those calculated using the srsc basis on niobium and cc-pVDZ on carbon. Subsequently, the IP predicted, is the difference between the $^2A_1$ and the $^1A_1$ states and has a value of 4.558 eV which is significantly lower than the experimental value. Inclusion of quadruple excitations (MRCI+Q) raises the IP to 4.690, only 0.35 eV below the experimental value.

	Calculated Transition	IP
srsc (Nb), cc-pVDZ (C)		
MRCI	$^2A_1 \rightarrow {}^1A_1$	4.558
MRCI+Q		4.690
B3LYP/srsc	$^2B_2 \rightarrow {}^1A_1$	5.126
Experiment		5.039 ± 0.012

Table 2.19: Ionisation Potential of Nb_3C_2 calculated at the DFT, MRCI and MRCI+Q levels. All values are in eV. Experimental IP taken from reference [21].

2.4 Conclusions

The low-lying excited states located in this study can be used to inform more detailed experiments on these species. The ZEKE spectra of both Nb_3N_2 and Nb_3C_2 scanned only to 500 cm^{-1} (0.06 eV), meaning that neither the $^3B_1$ state for Nb_3N_2 or the $^3A_1$ state of Nb_3C_2 would have been located. Scanning the ZEKE spectra to higher energies may reveal the onset of these low-lying (cationic) states, which these calculations would predict to appear at about 4000 cm^{-1}. The Nb_3 trimer is also a target for ZEKE experiments that could determine the energies of low lying cationic states. Conversely, no photoelectron spectra are known for either Nb_3N_2 or Nb_3C_2, these could be undertaken to determine excited states of the respective neutral species.

In the calculation of IPs, while no method of theory used in this study attains consistent "chemical accuracy", it is clear that DFT provides far more accurate IPs than the MRCI calculations, despite being three orders of magnitude faster. The errors for each method are summarised in Table 2.20. Adding quadruple excitations to the MRCI calculations increased IPs by 0.13 - 0.29 eV, suggesting that inclusion of only single and double excitations is (still!) inadequate to fully describe these systems. Thus it appears that the DFT treatment of correlation effects, while approximate and not systematically improvable, is superior than what can be reasonably produced employing MRCI methods. DFT is thus the method of choice and the next chapter is focussed on improving its performance.

	B3LYP	MRCI	MRCI+Q	Expt.
Nb_3	0.12	0.84	0.58	5.81 ± 0.05
Nb_3N_2	0.23	0.93	0.64	5.44 ± 0.05
Nb_3C_2	0.08	0.48	0.35	5.039 ±0.0012

Table 2.20: Errors in calculated IPs of Nb_3, Nb_3N_2 and Nb_3C_2 calculated at the DFT and MRCI+Q levels. All values are in eV. Experimental IPs taken from references [21, 23, 116]

Chapter 3

The IP Problem: BFW

IONISATION Potentials (IPs) or Electron Affinities (EAs) for transition metal clusters are an important parameter that can be used to identify and differentiate between clusters. Accurate calculation of these values is therefore vital. Previous attempts using a variety of DFT models have correctly predicted trends, but have relied on the use of scaling factors to compare to experimental IPs. In this chapter, we introduce a new density functional (BFW) that is explicitly designed to yield accurate, absolute IPs for transition metal clusters. This paper presents the numerical results for a selection of transition metal clusters and their carbides, nitrides and oxides for which experimental IPs are known. When tested on transition metal clusters, the BFW functional is found to be significantly more accurate than B3LYP and B3PW91.

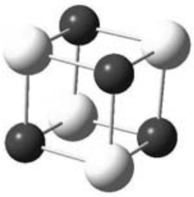

The last decade has seen an explosion in the experimental and theoretical study of transition metal clusters [18, 125–134]. Due to the size-dependent variation of each cluster's electronic and geometric structure, the interaction of a molecule with a specific cluster is unique, yielding species with novel chemical and physical properties. [18, 129, 130] Consequently, considerable effort has gone into understanding the physical and chemical properties of molecules, both experimentally and computationally. However, the partially filled *d*-shells of the metal atoms that constitute the clusters make this a difficult task.

For transition metal clusters, one of the most readily determined physical properties is the ionisation potential (IP) or electron affinity, (EA). These are easily obtained experimentally over a large range of sizes and their importance in understanding cluster properties has been documented in several reviews [18, 125–128, 130]. It has been shown that the IP and EA can provide information about electronic and geometric structure as well as chemical reactivity with other molecules. Therefore, the ability to accurately calculate IPs and EAs, and compare them with experiment, can provide an important component to understanding the physical and chemical properties of metal clusters. The reaction between Ag clusters and ethylene is an example where the use of IP information has been instrumental in determining the structure. For Ag_3-C_2H_4, DFT calculations predict two close-lying minima where the μ-bonded ethylene is either μ^1 or μ^2 bonded. Relative to Ag_3, the two isomers were predicted to have lower and higher IPs, respectively, the former being in better agreement with experiment [18, 134]. More recent work by some of the present authors has shown that the reaction of CO with Nb_3 and Nb_4 yields a product with an IP that is consistent with DFT calculations in which the CO is dissociated [135].

Hence, it is important to have the best possible computational tool for calculating absolute IPs and EAs for transition metal clusters and the relative changes that occur upon binding to a variety of molecules. However, accurately calculating theses values has been shown to be problematic [136]. DFT methods have been shown to accurately reproduce trends across series of metal clusters [124], but reproduction of absolute values has remained elusive. Calculations undertaken by Dryza *et. al.* employed linear shifts of 0.63 eV and 0.4 eV for Ta_3C_m and Ta_4C_m series respectively. The reliance on scaling factors determined *post hoc* robs calculations of much of their predictive power.

Due to the large number of electronic states that must be considered, ab initio methods require multi-configurational approaches and calculations are largely intractable for all but the very smallest clusters. Present DFT methods give values that vary dramatically with the chosen functional and basis set, which is not surprising since metal cluster species are not included in their parameterisation. Therefore, by optimizing a specific functional to cluster species, it may be possible to improve the performance of DFT for calculating such parameters.

3.1 Method

A common strategy in forming new density functionals, is the recombination of existing functionals into a compound functional. B3LYP [137], one of the most successful and widely used functionals, is of this form and comprises exact (or Fock [138]) exchange, the Dirac [139] and Becke‘88 [50] exchange functionals, and the Vosko-Wilk-Nusair [140] and Lee-Yang-Parr [141] correlation functionals. Other functionals of this form include the family of empirical density functionals; EDF1 [142] and EDF2 [143].

The determination of the linear mixing coefficients in these functionals is usually achieved by minimising the residual error between the predicted and experimentally measured values for a set of training data. This results in a functional that depends not only on the choice of component functionals, but also on the choice of training data. In practice this choice of data is dictated by the availability of accurately determined experimental values, such as those in the G2 data set [144]. For transition-metal clusters, few reliable thermochemical data are available in the literature and for this reason we were limited to transition-metal atoms, metal-metal dimers and metal oxides for which the ionisation potentials (IPs) or electron affinities (EAs) are well-established. Systems larger than diatomics were ruled out due to difficulties in obtaining reliable experimental values and/or uncertainties in the electronic states involved. A list of the 47 systems in the training set is shown in Tables 3.1 and 3.2.

For each system in the training set a reference density was computed using the B3LYP functional and SRSC effective core potential and associated basis set [47, 48]. Bond lengths for diatomics were optimized at the same level of theory and are listed in Table 3.2. Five exchange functionals (Fock [138], Dirac [139], Becke‘88 [50], Perdew-Wang ‘91 [145] and Gill ‘96 [146]) and six correlation functionals (Perdew ‘86 [51], Perdew-Zunger [147], Vosko-Wilk-Nusair fifth parameterisation [140], Lee-Yang-Parr [141], Wigner [148] and Perdew-Wang ‘91 [145]) were applied to these reference densities to obtain a set of eleven non-self-consistent energy vectors. Corrections for differences in zero-point vibrational energies are small in the reactions considered, and were not included. All calculations were undertaken using a development version of the QCHEM3.0 [149] software package using a 50 point Euler-Maclaurin radial grid and 302 point Lebedev grid for angular integration.

Estimates of the mixing coefficients were obtained by performing ‘external’ optimizations [142] using the non-self-consistent energies. This involved considering all possible k-subsets of the eleven energy vectors for $1 \leq k \leq 10$ and performing a linear regression using each subset of functionals to determine the optimal values of the mixing coefficients. No constraints were imposed on the coefficients and for simplicity, we included exchange-only and correlation-only combinations (i.e. all possible combinations of any k of the above eleven functionals were considered). This gives rise to a total of 2046 different functionals which, for each value of k, were ranked according to their mean absolute deviation (MAD).

As k increases from $1 \rightarrow 3$, the MAD of the optimal combination of functionals decreases sharply from 0.45 to 0.23 to 0.16 eV. This is to be expected as the increased flexibility of the functional is better able to model the data. The MAD decreases slightly to 0.158 eV for $k = 4$, but beyond this it remains almost constant and does not drop below 0.153 eV. The absence of significant improvement beyond $k = 3$ indicates that there are appreciable linear dependencies within our functional basis. This, too, is to be expected as each exchange (correlation) functional is trying to model the same component of the total energy. Based on these results it was decided to restrict our attention to three-parameter functionals. A list of the top five three-parameter functionals is shown in Table 3.3.

The five functionals shown in Table 3.3 can be divided into two distinct classes: The first are those based on the Wigner correlation functional, include around 29% exact exchange and have exchange coefficients that sum to 1.02. The second are those functional combinations based on the PW91 correlation functional. Both of these include 37% exact exchange and have exchange coefficients that sum to only 0.92. This, along with the much larger coefficient of the correlation component in these functionals, indicates there is a significant portion of the exchange energy that is being captured by the PW91 correlation functional.

It is clear that the Wigner-based functionals perform better for this set of training data, however, there is little to choose between them. We selected the first combination, (B88, HF and Wigner) and used this as a basis for further refinement. Two methods of refinement were tried, both producing similar results.

The first method used was optimisation of the ‘guess’ functional using a downhill simplex method [150]. Several vectors were supplied to this method, however in all cases the simplex converged, yielding coefficients only marginally different from the best guess values.

Secondly, a $5 \times 5 \times 5$ grid, centred at the coefficients in Table 3.3 was constructed, with step sizes corresponding to 5% of each coefficient. The *self-consistent* energies for all the members of the training set, along with the associated MAD values were computed at each of these grid points. Of these 125 self-consistent MAD values, the lowest (0.154 eV) was obtained by decreasing the Wigner coefficient by 5%, whilst leaving the B88 and HF coefficients unchanged. We attempted to further minimise this error by fitting a tri-quartic polynomial to the grid points values and finding the minimum on this three-dimensional surface, however, when the new estimates of the mixing parameters where used self-consistently, there was no improvement over the best grid point value.

The final form of our proposed functional is based on the best grid value and is given by

$$E_{\mathrm{XC}} = 0.736E_{\mathrm{X}}^{\mathrm{B88}} + 0.286E_{\mathrm{X}}^{\mathrm{Fock}} + 1.178E_{\mathrm{C}}^{\mathrm{Wigner}} \tag{3.1}$$

We call this the BFW functional and it can be considered as a hybridised form of the Becke-Wigner functional that was proposed some time ago [151].

3.2 Results and Discussion

Tables 3.1 and 3.2 contain the results of applying the BFW, B3LYP and B3PW91 functionals to the training set, B3PW91 was included as it has recently been successfully applied to clusters by Fielicke and co-workers [26]. Geometries for the diatomics were fixed at the B3LYP values to allow consistent comparison. As a test, geometry optimizations were also performed with each of the 3 functionals and it was found that the IPs changed very little. For the 26 transition metal atoms in the set BFW has a MAD of 0.10 eV, compared with 0.15 and 0.26 eV for B3LYP and B3PW91, respectively. Upon inclusion of the diatomic species, these values increase to 0.15, 0.24 and 0.29 eV, respectively, as shown at the bottom of Table 3.2.

Similarly, the mean signed deviation (MSD) of the BFW functional are improved over B3LYP and B3PW91 for the atomic and diatomic sets. Fortuitous cancellation of errors results in the overall MSD for B3LYP being slightly better than that of BFW. Overall, it is clear that BFW significantly out-performs the other two functionals for this training set.

In order to test the performance of the new functional on metal clusters, we needed to use only species whose geometric and electronic structure have been unambiguously characterised, these are listed in Table 3.4. Most of these species have been characterised by PFI-ZEKE, which is capable of extremely accurate ionisation potential determinations (± 3 cm^{-1}. Moreover, geometric information is conveyed in the vibronic features of the spectrum, although they rely on comparisons with predicted geometric structures. Yang and Hackett [24] have performed such experiments on a range of metal clusters and some of their carbides, nitrides and oxides. Other species for which ZEKE spectra are available have not been included i.e. V_3, V_4, Nb_5 and Nb_5X ($X = C_2, N_2$). For these species there is considerable uncertainty about their structures since insufficient vibronic information is carried in their spectra. However, we have included the species Nb_3, Nb_3CO and $Nb_3(CO)_2$. These species have only had their IPs determined by photoionisation efficiency (with an error of 0.05 eV), however, we have included them due to their similarity to the other niobium cluster species [135]. Clusters containing late transition metal atoms generally have much higher ionisation potentials that make them more difficult to characterise experimentally and therefore were not selected for the test set.

Published DFT geometries were used as the starting guesses for B3LYP optimizations. Single point energies using the new BFW functional as well as B3PW91 were carried out on the optimized structures. The Maximum Overlap Method [152] was employed in the single point energy calculations to ensure that the correct electronic state was maintained. The results are shown in Table 3.4.

Overall, the predicted ionisation potentials for the BFW functional are better than B3LYP and B3PW91, as can be seen in Table 3.4. The mean signed deviations of BFW, B3LYP and B3PW91 are +0.05, -0.12 and -0.12 eV, respectively, showing that, unlike B3LYP and B3PW91, the new functional tends to underestimate IPs. The MAD value for the BFW functional is also less than those of the others, indicating that its error distribution is narrower and suggesting that BFW is likely to reproduce IP trends more reliably than B3LYP and B3PW91.

BFW underestimates the IPs of the pure metal clusters (Y_2, Y_3, Zr_3 and Nb_3) by 0.07 to 0.20 eV. The B3PW91 functional overestimates these values by 0.03 to 0.25 eV. B3LYP overestimates all species except Zr_3. For the doped-clusters, BFW clearly performs better however this is to be expected given the bias toward metal - second row dimers in the training set. The exception to this is Zr_3O for which B3LYP and B3PW91 fortuitously calculate the value almost exactly.

Vibrational information is also known for all of the species in Table 3.5 (for both neutral and cation) through their ZEKE spectra (Nb_3 and Zr_3 data were obtained through matrix isolation Raman experiments [153, 154]. It was decided to test the ability of the new functional with respect to vibrational frequencies. In order to do this it was necessary to optimize the geometries of each cluster species (which has negligible effects on the IPs calculated above) and their harmonic vibrational frequencies were subsequently calculated. B3LYP geometries were used as the starting guesses for BFW and B3PW91 optimizations and the results are shown in Table 3.5 along with the experimental frequencies. The BFW frequencies are significantly improved over B3LYP and B3PW91, with MAD values of 15, 27 and 31 cm^{-1} respectively. In particular, low frequency symmetric bending modes ($\delta(M_n)$) are accurately calculated. The only poor result for BFW is for the Nb_3N_2 singlet cation, although it is better than the B3LYP and B3PW91 frequencies.

Out of curiosity, the new BFW functional was applied to the thermochemical values contained in the well-known G2 dataset [144]. In combination with the 6-31+G* basis set, atomisation energies, IPs, EAs and proton affinities were calculated and the results are summarised in Table 3.6. While this performance is mediocre, it is acceptable given that a functional tailored for a particular purpose often struggles when applied well outside its region of strength.

	Neutral State	Cation State	Exp.	Exp-BFW	Exp-B3LYP	Exp-B3PW91
Sc	$^2D_{3/2}$	$^3D_1$	6.56	0.00	0.03	0.15
Ti	$^3F_2$	$^4F_{3/2}$	6.83	0.24	0.24	0.50
V	$^4F_{3/2}$	$^5D_0$	6.75	-0.13	0.04	0.01
Mn	$^3F_2$	$^7S_3$	7.43	-0.15	-0.12	0.21
Fe	$^6S_{5/2}$	$^6D_{9/2}$	7.90	-0.15	-0.13	0.11
Co	$^4F_{9/2}$	$^3F_4$	7.88	0.34	0.07	0.10
Ni	$^3F_4$	$^2D_{5/2}$	7.64	-0.03	-0.3	-0.25
Cu	$^2S_{1/2}$	$^1S_0$	7.73	-0.18	-0.45	-0.38
Zn	$^1S_0$	$^2S_{1/2}$	9.39	-0.09	-0.13	0.00
Y	$^2D_{3/2}$	$^1S_0$	6.22	-0.11	-0.12	-0.29
Zr	$^3F_2$	$^4F_{3/2}$	6.63	0.06	0.06	0.26
Nb	$^6D_{1/2}$	$^5D_0$	6.76	0.00	-0.17	-0.33
Mo	$^7S_3$	$^6S_{5/2}$	7.09	0.02	-0.14	-0.33
Tc	$^6S_{5/2}$	$^7S_3$	7.28	0.05	-0.16	-0.28
Ru	$^5F_5$	$^4F_{9/2}$	7.36	-0.01	-0.25	-0.32
Rh	$^4F_{9/2}$	$^3F_4$	7.46	0.02	-0.24	-0.27
Pd	$^1S_0$	$^2D_{5/2}$	8.34	-0.17	-0.26	-0.28
Ag	$^2S_{1/2}$	$^1S_0$	7.58	-0.06	-0.31	-0.27
Cd	$^1S_0$	$^2S_{1/2}$	8.99	0.05	-0.04	0.07
Ta	$^4F_{3/2}$	$^5F_1$	7.89	-0.07	0.31	0.59
W	$^5D_0$	$^6D_{1/2}$	7.98	0.12	0.25	0.48
Re	$^6S_{5/2}$	$^7S_3$	7.88	0.02	0.07	0.48
Os	$^5D_4$	$^7D_{9/2}$	8.70	0.02	0.30	0.55
Ir	$^4F_{9/2}$	$^5F_5$	9.10	-0.13	0.14	0.11
Pt	$^3D_3$	$^2D_{5/2}$	9.00	0.02	-0.16	-0.19
Au	$^2S_{1/2}$	$^1S_0$	9.23	0.23	-0.01	-0.01
MAD (atoms)				**0.10**	**0.17**	**0.26**
MSD (atoms)				**0.00**	**-0.06**	**0.02**

Table 3.1: The 26 transition metal atoms in the training set (the Cr, La, Hf, Hg atoms were excluded because of either SCF convergence difficulties or lack of available ECPs for the SRSC basis set). Atomic ionisation potentials were obtained from the NIST database [155]. Calculated differences (eV) for the functionals tested are shown in the final three columns.

	Neutral State	B3LYP bondlength (Å)	Cation State	B3LYP bondlength (Å)	Exp.	Exp-BFW	Exp-B3LYP	Exp-B3PW91
V_2	$^3\Sigma^-$	2.00	$^4\Sigma^-$	1.86	6.36	0.10	0.04	-0.05
Cr_2	$^1\Sigma_g^+$	1.60	$^2\Sigma_g^+$	1.58	7.00	-0.06	-0.50	-0.49
Cu_2	$^1\Sigma_g^+$	2.25	$^1\Sigma_g^-$	2.39	7.90	-0.02	-0.23	-0.14
Nb_2	$^3\Sigma^-$	2.07	$^4\Sigma^-$	2.02	6.37	0.05	0.01	0.02
Mo_2	$^1\Sigma_g^+$	1.96	$^2\Sigma_g^+$	1.94	6.95	0.07	-0.05	-0.07
Ag_2	$^1\Sigma_u^+$	2.61	$^2\Sigma_g^-$	2.76	7.66	0.12	-0.12	-0.07
TiO	$^3\Delta$	1.63	$^2\Delta_{3/2}$	1.59	6.82	-0.24	-0.38	-0.37
VO	$^4\Sigma^-$	1.64	$^3\Sigma^-$	1.61	7.25	0.44	0.44	0.45
CrO	$^5\Pi$	1.65	$^4\Sigma^-$	1.65	7.85	-0.52	0.90	0.93
FeO	$^5\Delta_4$	1.65	$^6\Sigma$	1.68	8.56	0.13	0.07	0.18
CuO	$^2\Pi_{3/2}$	1.77	$^3\Sigma$	1.84	9.41	-0.01	-0.07	0.32
ZrO	$^3\Delta$	1.77	$^2\Sigma^-$	1.73	6.81	0.00	-0.15	-0.17
MoO	$^5\Pi$	1.74	$^4\Sigma^-$	1.68	7.45	-0.30	0.85	0.80
NbO	$^4\Sigma^-$	1.76	$^3\Sigma^-$	1.69	7.15	-0.12	-0.26	-0.35
TaO	$^2\Delta$	1.77	$^1\Sigma$	1.71	8.61	0.46	0.48	0.28
NiO^-	$^2\Pi_{3/2}$	1.68	$^3\Sigma^-$	1.65	1.47	0.09	0.18	0.16
PdO^-	$^2\Pi_{3/2}$	1.86	$^3\Sigma^-$	1.90	1.67	0.54	0.46	0.44
PtO^-	$^2\Pi_{3/2}$	1.83	$^3\Sigma^-$	1.90	2.17	-0.08	-0.02	-0.10
RhC^-	$^3\Pi$	1.69	$^2\Sigma^+$	1.65	1.46	0.93	0.87	0.80
RhN^-	$^2\Pi$	1.77	$^1\Sigma^+$	1.66	1.58	0.20	0.16	0.18
RhO^-	$^3\Sigma^-$	1.81	$^4\Sigma_{3/2}$	1.76	1.51	-0.23	-0.27	-0.28
MAD (dimers)						**0.21**	**0.32**	**0.32**
MSD (dimers)						**0.07**	**0.11**	**0.12**
MAD (overall)						**0.15**	**0.24**	**0.29**
MSD (overall)						**0.03**	**0.02**	**0.06**

Table 3.2: The 21 dimeric species in the training set. Ionisation potentials for dimers were obtained through DiRef [156] and references therein. Calculated differences (eV) for the functionals tested are shown in the final three columns.

MAD (eV)	Functionals in the mix
0.162	$0.286\ E_{\mathrm{X}}^{\mathrm{Fock}} + 0.736\ E_{\mathrm{X}}^{\mathrm{B88}} + 1.240\ E_{\mathrm{C}}^{\mathrm{Wigner}}$
0.164	$0.295\ E_{\mathrm{X}}^{\mathrm{Fock}} + 0.728\ E_{\mathrm{X}}^{\mathrm{PW91}} + 1.132\ E_{\mathrm{C}}^{\mathrm{Wigner}}$
0.164	$0.284\ E_{\mathrm{X}}^{\mathrm{Fock}} + 0.733\ E_{\mathrm{X}}^{\mathrm{Gill96}} + 1.389\ E_{\mathrm{C}}^{\mathrm{Wigner}}$
0.171	$0.373\ E_{\mathrm{X}}^{\mathrm{Fock}} + 0.551\ E_{\mathrm{X}}^{\mathrm{PW91}} + 1.698\ E_{\mathrm{C}}^{\mathrm{PW91}}$
0.173	$0.373\ E_{\mathrm{X}}^{\mathrm{Fock}} + 0.544\ E_{\mathrm{X}}^{\mathrm{B88}} + 1.818\ E_{\mathrm{C}}^{\mathrm{PW91}}$
0.214	B3LYP

Table 3.3: The five combinations of functionals with the lowest MAD. Note that these are based on the non-self-consistent energies obtained from B3LYP/SRSC densities. The (self-consistent) B3LYP MAD is also shown for comparison.

	Exp.	Exp-BFW	Exp-B3LYP	Exp-B3PW91
Y_2	4.98	0.11	-0.07	-0.11
Y_3	5.00	0.16	-0.04	-0.14
Y_3C_2	4.22	0.10	-0.13	-0.15
Zr_3	5.22	0.20	0.09	-0.03
Zr_3O	5.19	0.17	0.00	-0.01
Nb_3	5.80	0.07	-0.18	-0.25
Nb_3C_2	5.05	0.07	-0.09	-0.08
Nb_3O	5.51	-0.05	-0.20	0.25
Nb_3CO	5.82	-0.02	-0.21	-0.23
$Nb_3(CO)_2$	5.85	-0.14	-0.26	-0.26
Nb_3N_2	5.44	-0.09	-0.25	-0.27
MAD		**0.11**	**0.14**	**0.16**
MSD		**0.05**	**-0.12**	**-0.16**

Table 3.4: MAD and MSD errors (eV) for the IPs of transition metal complexes.

		Exp.	BFW	B3LYP	B3PW91
Y_2	$\nu_s(M-M)$	185	185	188	192
Y_2^+	$\nu_s(M-M)$	197	213	213	216
Y_3C_2	$\delta(M_n)$	82	82	96	107
$Y_3C_2^+$	$\delta(M_n)$	86	98	108	99
$Y_3C_2^+$	$\nu_s(M-M)$	228	239	239	244
Zr_3	$\delta(M_n)$	177	197	203	185
Zr_3	$\nu_s(M-M)$	258	279	284	287
Zr_3O^+	$\nu_s(M-M)$	272	276	277	262
Nb_3	$\delta(M_n)$	227	218	226	245
Nb_3	$\nu_s(M-M)$	335	367	361	370
Nb_3C_2	$\delta(M_n)$	237	233	249	263
Nb_3C_2	$\nu_s(M-M)$	327	353	357	368
$Nb_3C_2^+$	$\delta(M_n)$	258	265	265	272
$Nb_3C_2^+$	$\nu_s(M-M)$	339	352	360	370
$Nb_3N_2^+$	$\delta(M_n)$	257	324	377	386
Nb_3O	$\delta(M_n)$	330	332	346	350
Nb_3O	$\nu_s(M-L)$	720	709	704	715
Nb_3O^+	$\delta(M_n)$	312	304	308	316
MAD			**15**	**27**	**31**
MSD			**11**	**25**	**29**

Table 3.5: Experimental [24] and calculated frequencies (cm^{-1}) for clusters in the test set.

RMS errors (kcal/mol)	Exp-BFW	Exp-B3LYP	Exp-B3PW91
atomisation energies	13.48	8.10	6.10
ionisation potentials	8.62	5.05	6.63
electron affinities	6.53	4.40	5.16
proton affinities	7.33	5.51	5.80

Table 3.6: RMS thermochemical errors (kJ/mol) for functionals. Experimental values are taken from the G2 dataset [144].

Chapter 4

Structure Determination Using a Stochastic Search: Kick

DETERMINING the global minimum for an unfamiliar stoichiometry is a daunting task that quickly becomes ill-defined as the size of the problem increases. Transition metal clusters, in particular, defy simple bonding descriptions, and often possess several distinct geometries with near-degenerate energies making the task of determining the global minimum even more challenging. It is clear, that in such situations, relying on intuition will at best produce an incomplete picture and it is possible, even probable that novel geometries may be missed. Bera *et al.* (J Phys Chem A 2006, 110, 4287-4290) described the use of a stochastic algorithm to locate minima on the PES of any given stoichiometry. This algorithm was re-implemented and used to determine the low energy isomers of several different transition metal clusters.

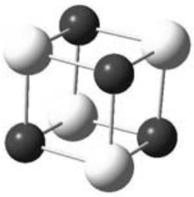

If you were to ask a chemist to predict all, or even the lowest energy isomers of a given stoichiometry, they would likely take some time to answer. This is not the fault of the chemist. As the number of atoms in a system increases, the possible connectivities scale factorially. Intuition about the chemistry one is looking for and the potential energy surface may narrow down these choices, but searching by hand is inefficient and non-intuitive structures, that may possess interesting chemistry or unusual stability, will often be missed.

To gain an idea of just how quickly such a problem becomes ill-defined, the possible connectivites for a tetramer are illustrated below in Figure 4.1 (a-f). Next to each label is the number of permutations possible when A, B, C and D are all different, giving a total of 56 possible permutations. Bera *et. al.* [157] illustrated the possible connectivities of a pentatomic molecule, indicating also, the number of possible permutations for the case of an ABCDE molecule. They listed a total of 15 possible connectivities with a total of 577 permutations!

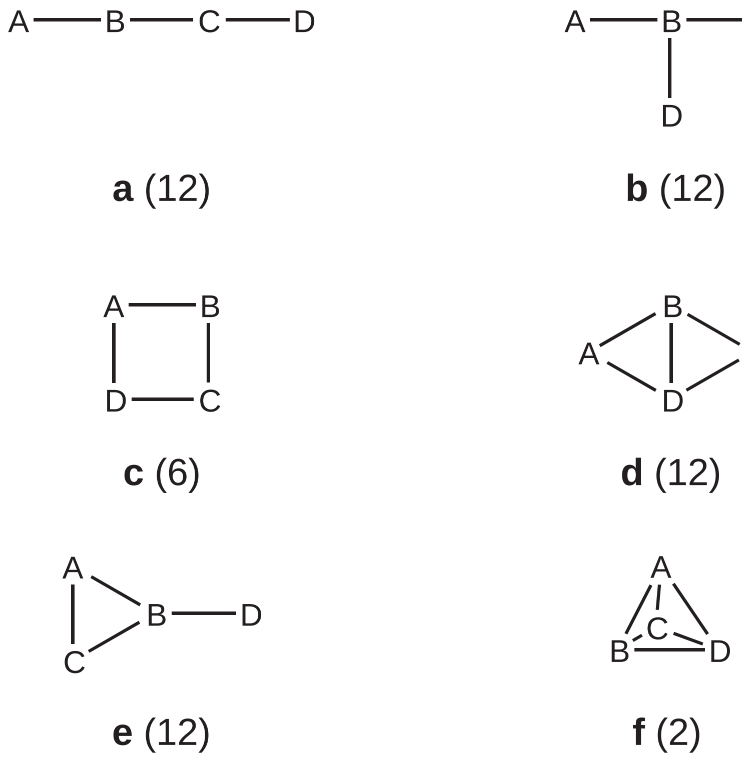

a (12) **b** (12)

c (6) **d** (12)

e (12) **f** (2)

Figure 4.1: Possible connectivities and permutations for a tetratomic molecule.

Transition metal cluster chemistry often involves low symmetric species with ill-defined bonds so small perturbations in the geometry can have strong effects on the energy of the cluster. The human chemist may be able to explain these effects in retrospect, but one would have to have many monkeys working without breaks to sift through all the possibilities in advance. There may be a manageable number of possible isomers if say a 30° rotation of any angle or dihedral is considered significant, but this quickly becomes an unmanageable number when a 5° or even a 15° rotation makes the difference between a minimum and a transition state. When several such coordinates are important or unknown, the number of possible structures rapidly becomes too daunting for the human chemist to list, let alone rank in order of stability.

There are many well known algorithms to search across conformer space for the global minimum; simulated annealing [158], genetic algorithms [159], basin hopping [160], Monte Carlo [161] and scaled hyper sphere [162] searches have all been used alone and in various combinations. Fewer algorithms exist to “signpost” or “sketch out” a completely unfamiliar potential energy surface with no *a priori* information.

Saunders [163] first suggested a stochastic algorithm and applied it to C_6. His algorithm began with a Gaussian input file and applied a random translation or “kick” to each atom, limited only by a preset maximum translation size, resulting in each system being confined to a sphere. Bera *et al.* [157] used the same stochastic method but began with no *a priori* known structure, instead placing each atom at a point and then randomly translating it within a box of given dimensions.

The second approach was felt to be more flexible as it allows the size of the box to be changed at will, decreasing one dimension of the box will direct the search toward planar structures, decreasing two dimensions will of course, only permit linear structures.

Using this philosophy, code was written that presupposes only the number and type of atoms present in the system, the total charge and multiplicity of the system and the size of the box. Additional parameters are supplied; the number of jobs to run and a job time limit if necessary for the queueing system. The Kick-start script (Appendix B) will read an example header, so machine-specific filespace and memory concerns may be addressed there.

So, with enough supercomputer resources, all of chemistry can be entirely solved! This was predicted even two centuries ago:

> *"We are perhaps not far removed from the time when we shall be able to submit the bulk of chemical phenomena to calculation."* - Joseph Louis Gay – Lussac. *Memoires de la Societe D'Arcueil* 1808*,* 2*,* 207*.*

Of course, some parts of "chemistry" will be solved more efficiently than others.

A subset of chemical problems involve some reasonably well defined species A, reacting with B to produce unknown results. Specifically of interest to this thesis, is one or more (gaseous) reactants reacting on a (well defined) metal cluster, producing unknown results. In order to tackle this problem more efficiently, a "fragment" capability was built into the new Kick code. When a fragment is specified in the global input file, the script searches for a corresponding set of cartesian coordinates, which are then rotated randomly and translated by a random vector within the defined box. This chapter will discuss the use of Kick without fragments to elucidate the structures of transition metal clusters, chapter 5 will discuss the application of the fragment capability to several different chemical systems.

Many initial geometries thus generated of course, produce "garbage" results; with atoms virtually coincident or alternately too far apart. Most of these garbage geometries will not achieve SCF convergence and die quickly. Other initial geometries will not achieve geometric convergence in the time allowed. Judicious choice of walltime limit can prevent these jobs from wasting resources. To prevent minima being “missed”, more batches of jobs are run until no new minima are obtained - i.e. enough initial guesses will generate a guess within the “catchment area” of any minimum on the potential energy surface. Who knew monkeys could do chemistry as well as English Literature?

A second script parses the logfiles of all jobs run and identifies those that complete normally. From these jobs, the final energies are obtained and any redundancies (to within 0.00001 au) are eliminated without any checking of the geometries. The cutoff of 1×10^{-5} a.u. was the same as that employed by Bera *et al.*. For these unique structures, the final geometry is obtained from the logfile and stored with the energy and file reference.

A third (optional) script, will take all the unique geometries and resubmit them as frequency jobs or optimisations / single point energies at a higher level of theory.

Using this methodology, the singlet (or doublet in the case of odd-electron species) potential energy surfaces of the following systems were investigated: NbMoRuRhPd, $\mathrm{Rh_6}$, $\mathrm{Pd_nAu_m}$ (m + n = 5) and $\mathrm{Nb_nRh_m}$ (m + n = 5). Unless otherwise stated, calculations were undertaken using the B3P86 functional and SRSC basis set combination. In figures, bonds are drawn between two atoms when the distance between those two atoms is less than the sum of their covalent radii.

4.1 NbMoRuRhPd

Bera *et al.* [157] studied two pentameric ABCDE systems, BCNOS and CAlSiPS, finding linear isomers to be the most stable for the first system and triangle + linear chain (which they termed; type o) structures to be the most stable motif for the second system. A metallic ABCDE system would be expected to favour close-packed structures to a much greater degree than either of the organic examples studied by Bera. Five consecutive (skipping Technetium) second row transition metal elements were chosen: Nb through to Pd.

500 kick jobs yielded 39 unique structures from 216 successful jobs. Indeed, packed structures were favoured with 8 of the lowest 9 structures being tetrahedra with the fifth atom bound to one of the edges (i.e. across a bond). The second lowest energy structure was an axle-and spoke geometry. Distorted square pyramids comprised the next lowest energy group of structures, with capped butterfly structures (curiously these were nearly always capped by the palladium atom) being favoured for the remaining isomers. All unique structures are included in Figure 4.2.

The lowest 23 structures all contain a Nb-Mo bond.

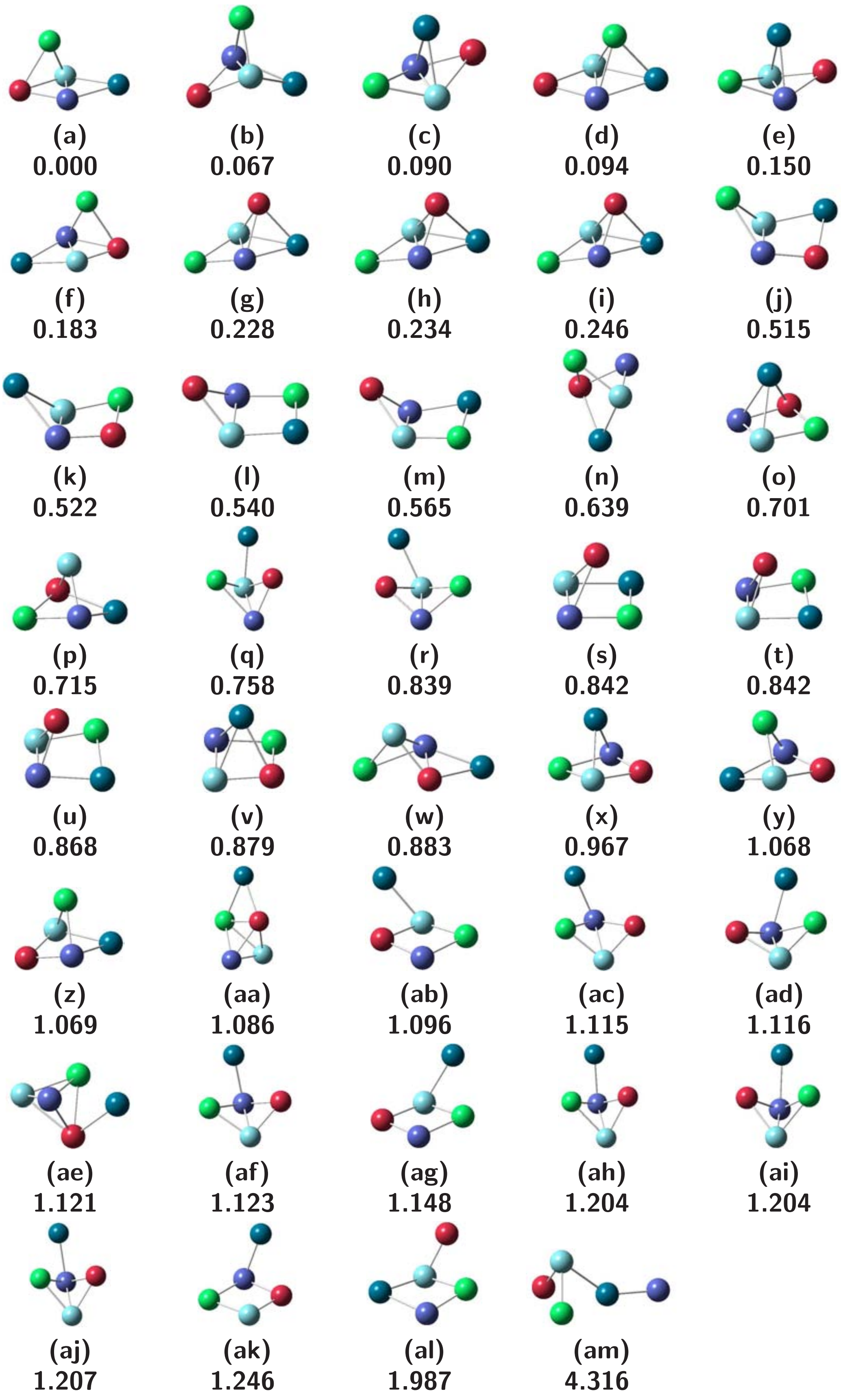

(a) 0.000
(b) 0.067
(c) 0.090
(d) 0.094
(e) 0.150
(f) 0.183
(g) 0.228
(h) 0.234
(i) 0.246
(j) 0.515
(k) 0.522
(l) 0.540
(m) 0.565
(n) 0.639
(o) 0.701
(p) 0.715
(q) 0.758
(r) 0.839
(s) 0.842
(t) 0.842
(u) 0.868
(v) 0.879
(w) 0.883
(x) 0.967
(y) 1.068
(z) 1.069
(aa) 1.086
(ab) 1.096
(ac) 1.115
(ad) 1.116
(ae) 1.121
(af) 1.123
(ag) 1.148
(ah) 1.204
(ai) 1.204
(aj) 1.207
(ak) 1.246
(al) 1.987
(am) 4.316

Figure 4.2: NbMoRuRhPd structures identified in a Kick run. Relative energies are given in eV. Nb atoms are coloured pale blue, Mo atoms are purple, Ru atoms are red, Rh atoms are green and Pd atoms are turqoise.

4.2 Rh_6

Owing to their industrial importance as highly reactive catalysts and as a possible medium for high density magnetic storage, rhodium clusters, Rh_n, have been extensively studied by both experimental [164–166] and theoretical [167–170] means. Walsh *et al.* studied neutral and cationic Rh_6 clusters using a basin-hopping algorithm [160] and DFT. It was therefore, thought that this system made a good test case, particularly as the use of bulk-derived empirical potentials prevented the basin-hopping algorithm from finding the trigonal prism minimum, which they included in their DFT calculations on the basis of a previous study [171].

Some 100 jobs were run, resulting in 45 successful jobs, of which 11 possessed unique geometries, these are listed in Figure 4.3. No new structures were identified in the final two 10 job runs. The four lowest energy structures identified by Walsh and co-workers were identified by Kick as the trigonal prism (**a**, 0.000 eV), octahedral (**b**, 0.334 eV), bicapped tetrahedron / capped trigonal bipyramid (**c**, 0.376 eV) and face-capped square pyramid / slanted trigonal prism (**d**, 1.053 eV).

The other seven identified structures were three edge-capped square pyramids (**e** 1.138,**f** 1.248 and **g** 1.278 eV), an edge-capped trigonal bipyramid (**h**, 1.666 eV), two edge capped tetrahedra (**i**, 1.749 and **j** , 1.888 eV) and an obtuse trigonal prism (**k**, 2.385 eV). A manual search identified no planar structures and a C_{5v} starting structure collapsed to a capped square pyramid.

It was attempted to use Kick to search for transition states, however 100 jobs found only 9 candidate structures, the lowest energy of which was 1.194 eV above the Rh_6 global minimum and therefore not energetically competitive. Given the higher sensitivity of transition state searches to the initial geometry, it is preferable to identify minima and then target transition

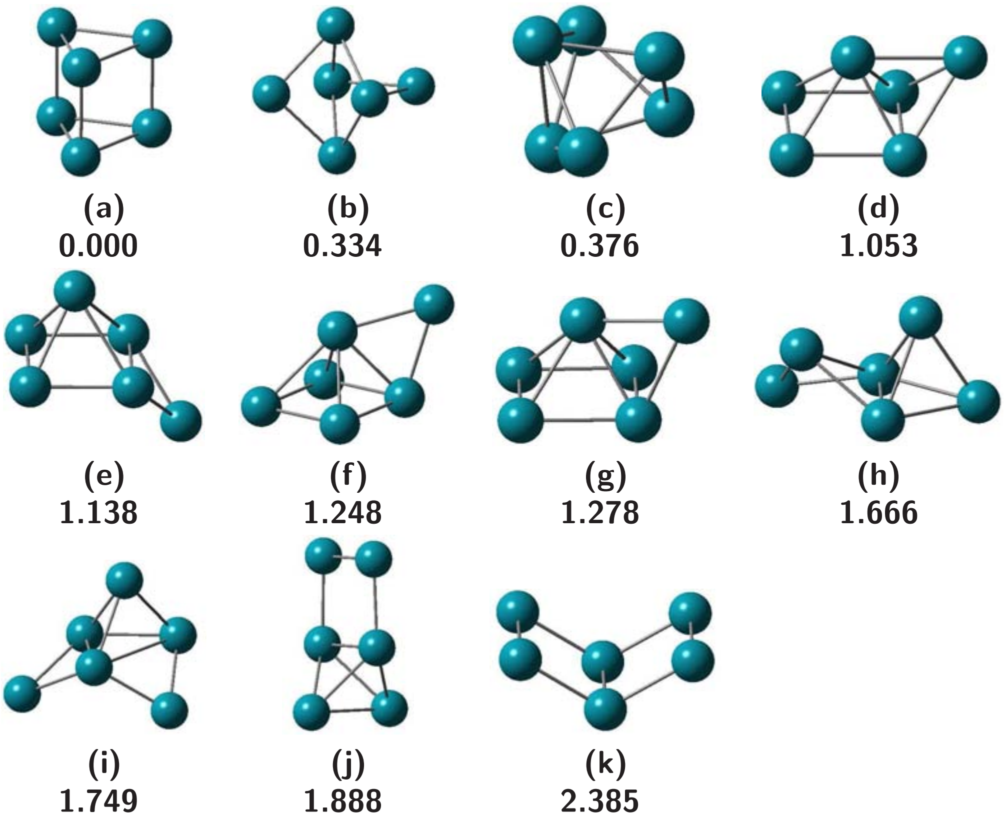

(a) **0.000**
(b) **0.334**
(c) **0.376**
(d) **1.053**
(e) **1.138**
(f) **1.248**
(g) **1.278**
(h) **1.666**
(i) **1.749**
(j) **1.888**
(k) **2.385**

Figure 4.3: Rh_6 structures identified in a Kick run. Relative energies are given in eV.

state searches between these minima.

4.3 Pd_nAu_m (m + n = 5)

Gold clusters have been extensively studied by both experimental [172–175] and theoretical [176, 177] means. Further studies have examined the effect of single-atom doped gold clusters [178, 179] and binary alloys [173, 180–182] on structure and adsoprtion characteristics. For example, it has been shown that in binary Au/Pt clusters, O_2 prefers to adsorb on Au atoms, whereas CO prefers to adsorb on Pt [183].

Several studies [176, 177] have shown gold clusters to prefer planar structures up to the hexamer, whereas the global minima for palladium clusters $\geq$ 4 atoms prefer 3D structures [184, 185]. It was therefore decided to investigate binary clusters, Pd_nAu_m with $m + n = 5$ to determine the effect of cluster composition on structure.

For each stoichiometry, 50 jobs were run as an initial batch and further lots of 10 were run, if necessary, to ensure no new minima were obtained. A 4 Å cube was used as the default box size in all runs.

For Pd_5, 49 jobs completed successfully, to yield 3 unique geometries. These are shown in Figure 4.4. All three structures were quite similar in energy, the lowest two structures (**a**, 0.000 and **b**, 0.003 eV) are both essentially trigonal bipyramidal, with the higher energy isomer having a larger plane-to-tip dihedral angle. The third isomer (**c**, 0.008 eV) is a square pyramid. Both the trigonal bipyramid and square pyramid structures were predicted by Cheng *et al.*, who also predicted them to lie quite close in energy, with predicted binding energies of 1.791 and 1.785 eV/atom for the trigonal bipyramid and square pyramid isomers respectively.

15 successful jobs identified two Pd_4Au structures which are shown in Figure 4.5. Both structures obtained were analogues of the lowest energy Pd_5. The global minimum had replaced one of the tip atoms, the plane substituted isomer, **b**, had an energy 0.079 eV above the global

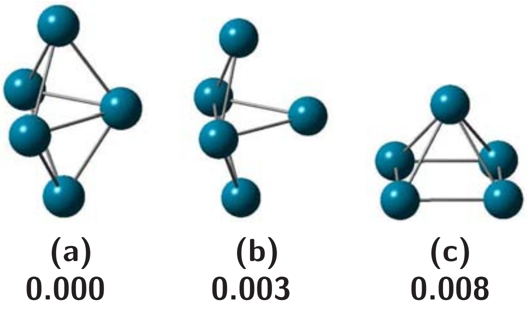

Figure 4.4: Pd_5 structures identified in a Kick run. Relative energies are given in eV.

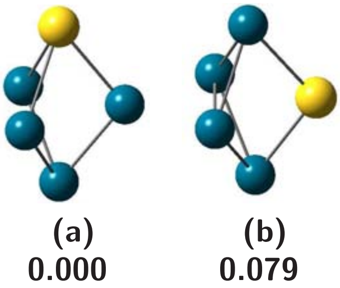

Figure 4.5: Pd_4Au structures identified in a Kick run. Relative energies are given in eV.

minimum.

For Pd_3Au_2, 38 successful jobs identified 5 unique minima. These are shown in Figure 4.6. The lowest three minima (**a**, 0.000; **b**, 0.103 and **c**, 0.154 eV) were the plane-plane, tip-tip and tip-plane disubstituted trigonal bipyramids respectively. Lying significantly higher in energy were a Au_5-like planar structure (**d**, 0.761 eV) and a planar C_{2v} structure (**e**, 1.250 eV). Structures obtained by manual substitution of these two isomers converged to one of the previously identified 3D minima. A further Kick run of 20 structures, using a planar, $5 \times 5 \times 1$ Å box did not identify any new structures.

A total of 100 jobs, of which 69 were successful, identified 13 unique Pd_2Au_3 geometries, which are shown in Figure 4.7. The lowest two isomers (**a**, 0.000 and **b**, 0.044 eV) are both strongly distorted trigonal bipyramids. The next two structures (**c**, 0.064 and **d**, 0.0184 eV) can be thought of as Au_5-like structures that are strongly distorted from planarity by the presence of a Pd-Pd bond. Three structures (**e**, 0.234; **f**, 0.318 and **g**, 0.342 eV) are capped

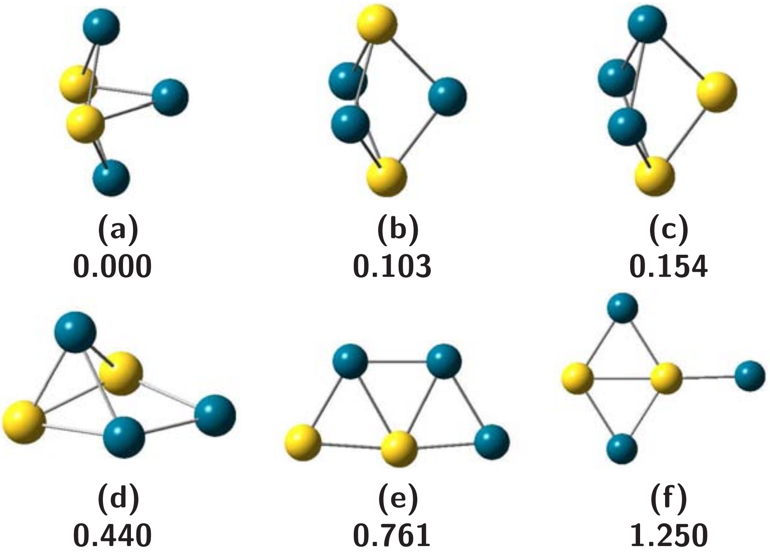

Figure 4.6: Pd_3Au_2 structures identified in a Kick run. Relative energies are given in eV.

Pd_2Au_2 tetrahedra; the lowest two of these structures has the remaining gold atom attached to a single gold atom, while the highest energy structure uses the remaining gold atom to bridge a Au-Pd bond. Another two distorted Au_5-like structures (**h**, 0.393 and **i**, 0.444 eV), are followed by a distorted trigonal bipyramid (**j**, 0.499 eV), a bridge-capped Pd_2Au_2 tetrahedron (**k**, 0.690 eV), another distorted Au_5-like structure (**l**, 0.806 eV) and an end-capped $PdAu_3$ tetrahedron with almost C_s symmetry (**m**, 1.049 eV).

Of 60 $PdAu_4$ jobs, 44 were successful, yielding 9 unique structures within 0.55 eV. These are shown in Figure 4.8. Perhaps unsurprisingly, the lowest two structures are substituted Au_5 geometries. The global minimum is substituted in the centre atom, while the next lowest energy structure (**b**, 0.258 eV) has the palladium substitution on the top layer of atoms. Three structures, (**c**, 0.283; **d**, 0.293 and **e**, 0.352 eV) are bridge-capped $PdAu_3$ tetrahedra; the lowest of these is capped along a Au-Au bond, the slightly higher energy isomer is capped along a Au-Pd bond and the highest isomer returns to capping a Au-Au bond but with a Au-Au-Au-Au dihedral $\geq 180°$. The next isomer, (**f**, 0.367 eV) is an end-capped $PdAu_3$ tetrahedron. The remaining end-substituted Au_5 analogue has an energy 0.433 eV above the global minimum, **g**. A shallow butterfly (Au-Pd-Au-Au = 142°), capped on one wingtip, was 0.475 eV above

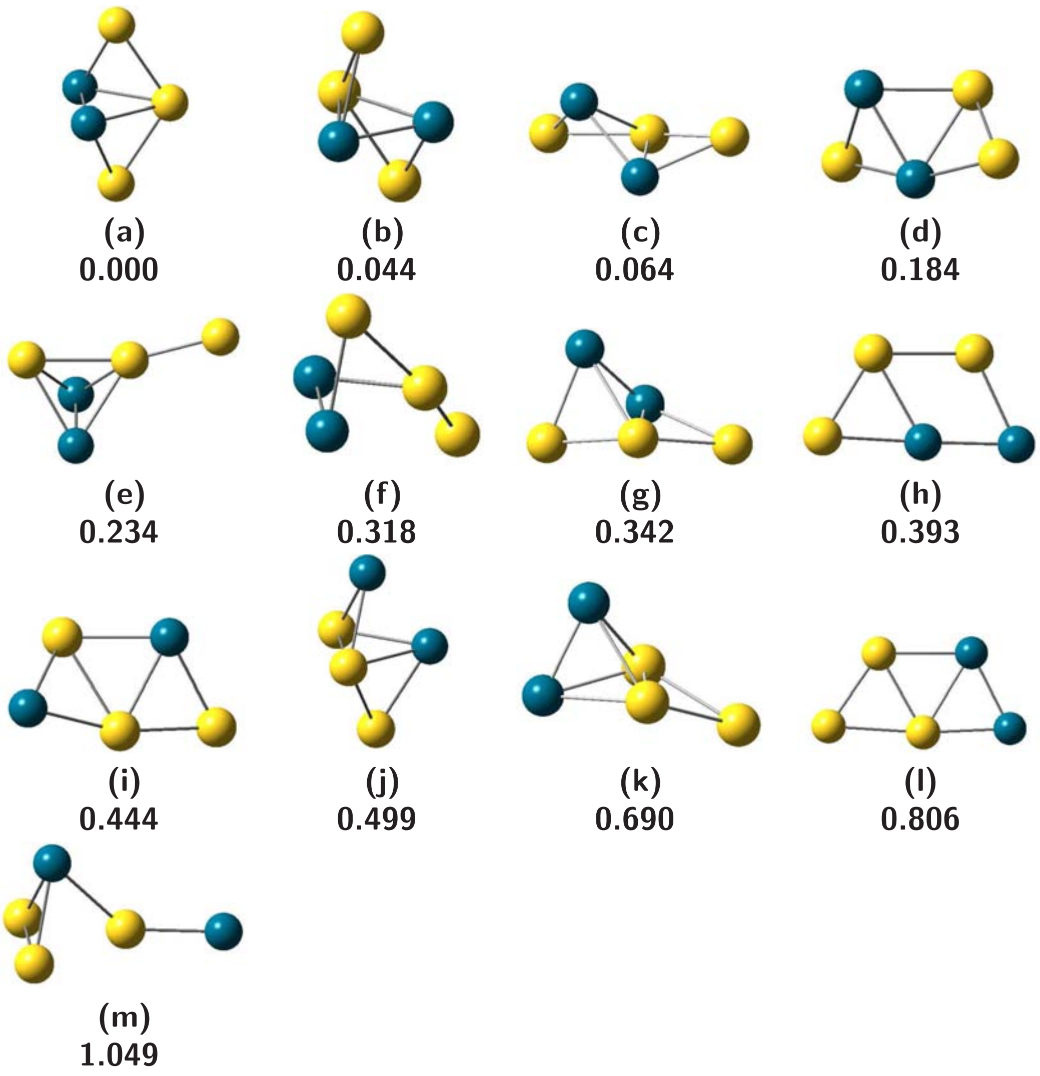

Figure 4.7: Pd_2Au_3 structures identified in a Kick run. Relative energies are given in eV.

the global minimum, **h**. Finally a planar "bow-tie" with the palladium atom on one of the corners, (**i**) had an energy 0.523 eV above the global minimum. Substitution of the centre atom to produce the other isomer of this structure rearranges to form the lowest energy isomer.

In the case of Au_5, only 7 of 50 jobs completed successfully, yielding one isomer which is shown in Figure 4.9. The low number successful jobs is not entirely unexpected, given the planar minimum. A cubic box, allows 3D structures to be generated which are clearly unfavourable for Au_5, leading to the large number of unsuccessful optimisations. As a check, a further 10 jobs were run with a 5 × 5 × 1 Å box. Of these jobs, 7 converged to the previously identified

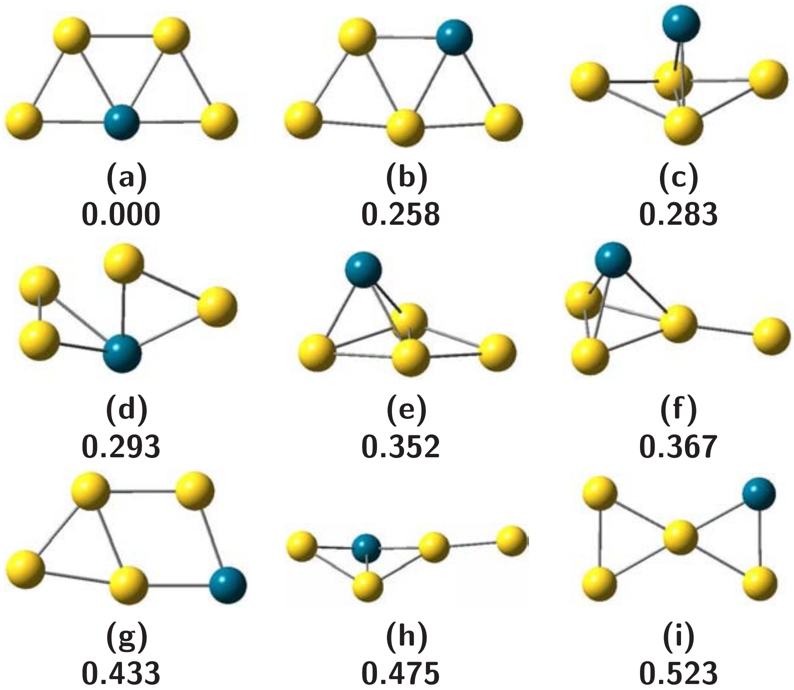
(a) 0.000
(b) 0.258
(c) 0.283
(d) 0.293
(e) 0.352
(f) 0.367
(g) 0.433
(h) 0.475
(i) 0.523

Figure 4.8: $PdAu_4$ structures identified in a Kick run. Relative energies are given in eV.

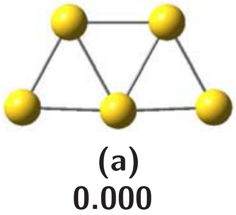
(a)
0.000

Figure 4.9: Au_5 structures identified in a Kick run. Relative energies are given in eV.

minimum. No new minima were located.

Across the series a clear gradient from "palladium-like" behaviour to "gold-like" behaviour can be seen. It should be noted that even in the "gold-like" structures with one or two palladium substitutions, substantial non-planarity is observed. An interesting exception to this however, is the planar Pd_3Au_2 structure (Figure 4.6), why this should retain planarity is unknown.

4.4 Nb_mRh_n (m + n = 5)

The second binary cluster considered was Nb_mRh_n, where (m + n = 5). In contrast to the Pd_nAu_m case, both these metals prefer 3-dimensional cluster structures. In particular trigonal bipyramidal structures are low energy isomers of both Nb_5 [186] and Rh_5 [187]. Thus binary clusters of Nb and Rh were not expected to show such a strong preference for "niobium-like" structures or "rhodium-like" structures.

The only binary Nb_mRh_n cluster in the literature, Nb_2Rh_2 was studied using DFT by Chen *et al.* [188] who determined that the Nb-Nb bond was the strongest bond, followed by Nb-Rh and Rh-Rh.

For the Nb_5 cluster, 55 jobs were run, of which 32 were successful. All of these jobs converged to the single minimum shown in Figure 4.10. Manual attempts to converge other geometries (square pyramid, axle-and-spoke, pentagonal) were either unsuccessful or converged to the trigonal bipyramid. The linear isomer was found to lie 9.129 eV above the global minimum. As a further check, seeing as no other runs had produced only one stable geometry, the first 50 starting (random) geometries of Rh_5 (which generated two unique Rh_5 structures) were re-run with niobium atoms being substituted, again producing only the trigonal pyramid shown in Figure 4.10.

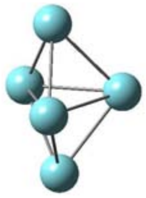

(a)

0.000

Figure 4.10: Nb_5 structures identified in a Kick run. Relative energies are given in eV.

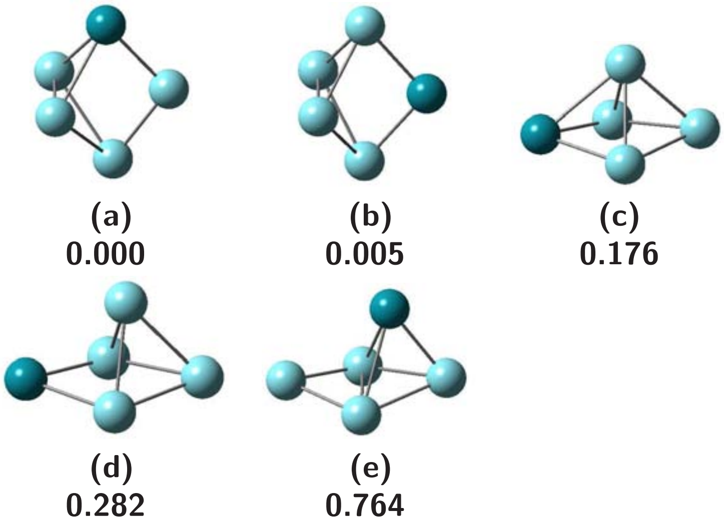

Figure 4.11: Nb_4Rh structures identified in a Kick run. Relative energies are given in eV.

110 kick jobs were run for the Nb_4Rh cluster. 47 of these completed successfully, identifying 5 unique geometries which are listed in Figure 4.11. The lowest two geometries are the tip (**a**, 0.000 eV) and plane (**b**, 0.005 eV) substitutions of Nb_5. The next lowest structure (**c**, 0.176 eV) may be viewed as a hybrid trigonal bipyramid / square pyramid, with a Rh-Nb-Nb-Nb dihedral of 164° and a Nb-Rh-Nb angle of 76°. The next structure (**d**, 0.282 eV) is a bridge-capped Nb_4 tetrahedron which has a base Rh-Nb-Nb-Nb dihedral of 170°, much higher in energy (**e**, 0.764 eV) lies a similar structure with the fourth Nb atom bridge-capping a Nb_3Rh tetrahedron over a Nb-Nb bond.

For the Nb_3Rh_2 cluster, 140 jobs were run, of which 11 were successful. The resulting 6 unique structures are presented in Figure 4.12. Approximately 30% of jobs failed due to not being able to take a valid geometry step. The global minimum is still a Nb_5-type cluster which possessed almost C_{2v} symmetry. There were no other structures within 0.5 eV, the next lowest structure had an energy 0.608 eV above the global minimum. It sacrifices a Nb-Nb bond and two Nb-Rh bonds to create a rhomboid base with a Rh-Nb-Nb-Rh dihedral of 174° and Nb-Rh-Nb angle of 76°. The isomer with an energy 0.629 eV above the global minimum has similar bonding, but the Rh-Nb-Nb-Rh dihedral is 180° and the Nb-Rh-Nb angle is 78°. A bridge-capped Nb_3Rh tetrahedron has an energy 0.742 eV above the global minimum. The

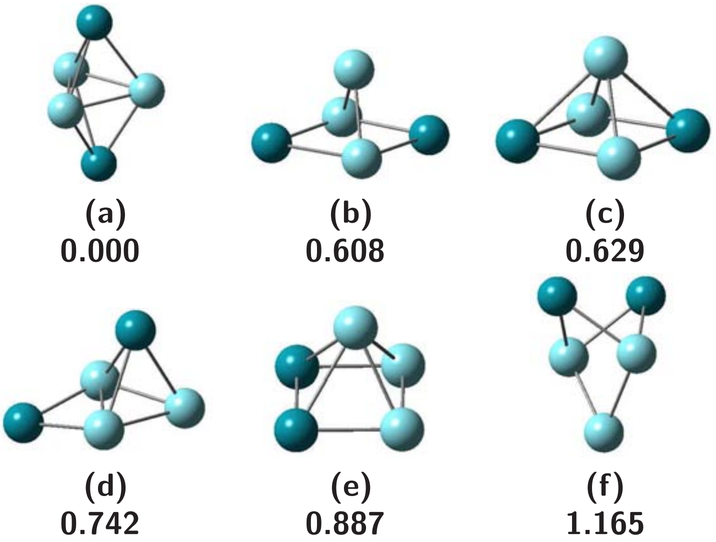

Figure 4.12: Nb_3Rh_2 structures identified in a Kick run. Relative energies are given in eV.

first clear Rh_5-like structure (square pyramid) has a relative energy of 0.887 eV. Other possible substitutions of this structure (Rh atoms at opposite corners of the base, one Rh atom at the peak) converged to one of the existing isomers. The final isomer is a C_{2v} axle-and-spoke type structure with a Rh-Nb-Nb-Rh dihedral of 85°. Attempts to converge an isomer of this structure with an Rh-Rh axis converged to the second kick generated isomer (**b**, 0.608 eV).

Of 180 kick jobs run for Nb_2Rh_3, 22 completed successfully, yielding 7 unique structures which are shown in Figure 4.13. The lowest energy structure is a C_{2v} axle-and-spoke geometry with a Nb-Nb axle, the unique Rh-Nb-Nb-Rh dihedral is 90°. The next lowest energy structure (0.375 eV), a distorted trigonal bipyramid may also be viewed as an axle-and-spoke type geometry with one dihedral being $\geq 180°$. The next three structures (0.904, 1.263 and 1.285 eV) are all based on a Nb-Rh-Nb-Rh square with the additional Rh atom attached to a Nb atom. The Rh-Nb-Nb-Rh "square" dihedral decreases with increasing isomer energy (166°, 108° and 97° respectively). The final two structures are both distorted square pyramids, the lower energy isomer (1.330 eV) has a Nb-Nb bond length of 2.64 Å, a Nb-Rh bond length of 2.19 Å and an Rh-Rh bond length equal to that of Nb-Nb, the third Rh atom bridges the Nb-Nb bond with a dihedral of 79°. The highest energy isomer (1.425 eV) has a more square base with a Nb-Nb bond length of 2.50 Å, two Nb-Rh bonds of 2.26 Å and a Rh-Rh bond of 2.55 Å.

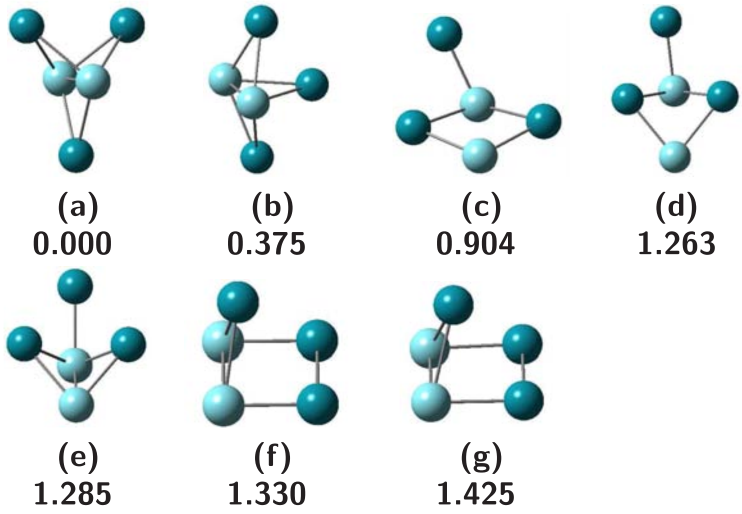

Figure 4.13: Nb_2Rh_3 structures identified in a Kick run. Relative energies are given in eV.

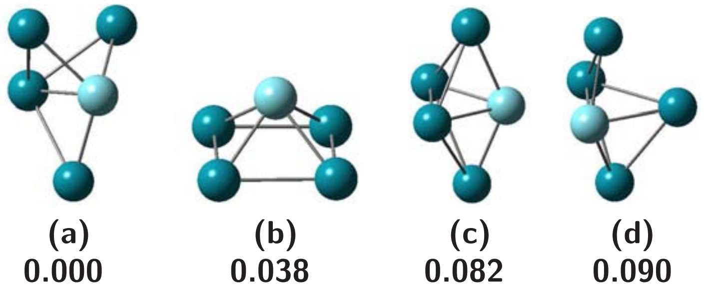

Figure 4.14: $NbRh_4$ structures identified in a Kick run. Relative energies are given in eV.

Again, the third Rh atom bridges the Nb-Nb bond with a dihedral of 74°.

150 kick jobs, of which 30 completed successfully, yielded 4 isomers of $NbRh_4$ which are shown in Figure 4.14. Unlike most other cases, all isomers were within 0.1 eV of the global minimum. The lowest energy structure was an axle-and-spoke geometry with C_s symmetry. 0.038 eV higher lies a square pyramid with C_{4v} symmetry **(b)**. The next isomer (**c**, 0.082 eV) is a trigonal bipyramid (C_{2v} with the niobium atom in the triangle plane. An attempt to converge a structure with the niobium atom on the tip converted back to structure **c**. The final structure calculated (**d**, 0.090 eV) was a bridge-capped $NbRhRh_3$ tetrahedron with the Rh atom bridging a Nb-Rh bond.

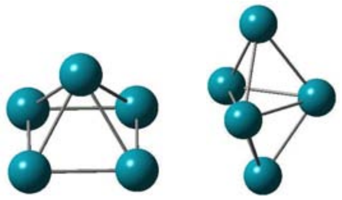

Figure 4.15: Rh_5 structures identified in a Kick run. Relative energies are given in eV.

Only two minima were identified in 125 kick jobs for Rh_5. These are shown in Figure 4.15. A square pyramid was identified as the global minimum with a trigonal pyramid structure lying 0.132 eV higher in energy.

Unlike the Au_mPd_n system, there was no obvious trend observed in structures as incremental substitutions were made. This is expected given the competitiveness of the Rh_5 trigonal bipyramid. What was strongly observed in this series was the ability of kick to identify many structurally similar isomers, such as structures **b** and **c** of Nb_3Rh_2 or **f** and **g** of Nb_2Rh_3. Also of note was that no planar structures were observed in any of the Nb_mRh_n clusters, suggesting that the starting geometries provided by kick are not influencing the final chemistry. To confirm this, the Kick-generated input files for Au_4Pd, which did identify planar geometries, were rerun having substituted Au for Nb and Pd for Rh (i.e. $Au_4Pd \rightarrow Nb_4Rh$). Not only were no planar geometries identified, all successful jobs converged to one of the previously identified geometries for Nb_4Rh. In addition to supporting the lack of planar Nb_4Rh geometries, this run indicated the relative "tightness" of the catchment wells for minima on the Nb_4Rh surface. Where 73% of the 60 Au_4Pd jobs completed successfully, only 17% of the Nb_4Rh jobs beginning from the same initial guesses completed successfully.

Chapter 5

Constraining a Stochastic Search with Molecular Fragments: Kick II

AN extension to the Kick program developed by Bera *et al.* (J Phys Chem A 2006, 110, 4287-4290) in which chemically-sensible molecular fragments are used in an automated stochastic search algorithm. This results in a vastly reduced region of the potential energy surface which can be explored very quickly. While this modification was conceived with reactions of transition metal clusters in mind, it is useful in a broad range of chemical problems. This modified algorithm has been used to search for low-lying isomers of a transition metal complex, the reaction products of small molecules with a transition metal cluster and isomers of a microsolvated dipeptide.

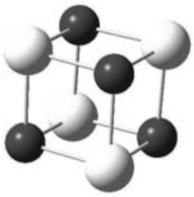

5.1 Introduction

In a follow-up to their original Kick paper, Bera *et al.* studied the periodane (LiBeBCNOF) molecule and highlighted highlighted the utility of an automated stochastic search procedure combined with the focus afforded by the chemical intuition of a human [189]. After their initial unrestricted search uncovered predominantly planar structures, they restricted all further guesses to C_s symmetry, which highlights the ability of human observation to reduce the complexity of the problem. Another, potentially more applicable, way to reduce the complexity of a problem, is to specify chemically sensible molecular fragments that should be present in the final geometry. Thus, the original Kick algorithm was extended to include the handling of arbitrary molecular fragments.

Once candidates for the global minimum of a cluster are discovered, it is then often desired to determine the binding configuration and energy of the cluster reacting with a small molecule target. Such systems could be investigated by supplying Kick with the individual atoms of the cluster + individual atoms of the desired reactants, however it is clear that as the size of the cluster increases, a diminishing proportion of jobs will form the desired cluster and many "successful" jobs will be wasted. Thus efficiency can be gained by defining the previously established cluster structure as a fragment. Chemically, it is generally considered that perturbations to the geometry of the metal cluster upon binding with a small molecule will be minor, therefore defining the cluster as a fragment and kicking it with the desired molecule(s) does not, in general, exclude *relevant* portions of the PES for the system from investigation.

For each fragment specified in the global input file, the script reads in cartesian coordinates, which are rotated by a random angle about each cartesian axis before being translated ("kicked") into the box. Rotation of the coordinates prior to kicking the fragment avoids fixing the relative orientation of the fragments when two or more fragments are specified. Atoms possess spherical symmetry and can therefore be kicked into the box without any prior processing. Fragments are placed in the box according to their first atom, therefore this atom is guaranteed to be within the specified box, however depending on the random rotation and translation applied and the shape and extent of the fragment itself, not all atoms of the fragment may be contained within the box. By default, no constraints are placed on geometry optimisations within a Kick run, thus allowing the geometries of defined fragments to relax. Dissociation of supplied fragments is possible, but unlikely, so determining whether a small molecule associatively or dissociatively adsorbs on a cluster would kick the small molecule as its constituent atoms. Such an approach allows a chemically sensible subset of the PES for a given stoichiometry to be searched efficiently with all the advantages that an otherwise unbiased, stochastic search procedure offers.

The characteristics of transition metal cluster chemistry that complicate the investigation of such systems, (*viz.* low symmetry species, ill-defined bonding and complicated energetics) are in no way exclusive to these systems. The same difficulties also occur in the investigation of hydrogen-bonded complexes such as those that result from the hydration of organic molecules. An example is the binding of H_2O to amino acids or peptides. These species present challenges in determining the optimal binding sites and orientations, particularly as the binding of solute molecules may change the conformational preference of a peptide. However, as in the reaction of small molecule species on a transition metal cluster, these systems are comprised of clearly defined sub-units and therefore may be efficiently and thoroughly investigated by a stochastic search that maintains these sub-units.

To illustrate the broad applicability of this modified Kick algorithm, it has been applied to three quite different chemical systems; a transition metal complex, reactions of transition metal clusters and a microsolvated dipeptide.

Zeise's anion was investigated in two separate Kick runs; one run employing an ethylene fragment and the second run employing no fragments (i.e. all 10 atoms were Kicked individually). Secondly the structure of Au_6 was determined and then this geometry was used as a fragment in further Kick runs with CO, O_2 and CO_3 in order to determine the thermodynamic products of the reaction of Au_6 with CO and O_2. In these runs, the Au_6 cluster was maintained, however the small molecule reactants were Kicked in both atomic and molecular (fragment) configurations. Finally the structure of two conformers of a microsolvated dipeptide were investigated by defining the dipeptide as one fragment and Kicking one or two additional water molecules as fragments. Except where specified, Kick runs were undertaken at the lowest possible multiplicity (i.e. singlet or doublet).

5.2 Zeise's anion

As an initial test of the efficiency of the fragment capability of Kick, Zeise's anion, $[PtCl_3(C_2H_4)]^-$ was investigated. Zeise's anion is a known 16 electron complex, where the ethylene ligand is a dihapto two-electron donor. Therefore, Kicking this system as 10 atoms and then with a supplied ethylene fragment (…one we prepared earlier…) allows a direct estimate of the efficiency gain possible by employing fragments.

The first run employed an ethylene fragment, the geometry of which was not optimised. The yield of successful completions was 34%. Zeise's anion was determined to be the global minimum and was obtained in the first 10 job batch. No significant new isomers were obtained after the third 10 job batch. Identified minima are listed in Figure 5.1. The second lowest energy isomer (**b**, 0.901 eV) has two Cl atoms bound to Pt and a singly bound CH_2CH_2Cl group. The CH_2CH_2Cl is in a staggered conformation and the Cl atom lies in the plane defined by Pt and the two carbon atoms, perpendicular to the Pt-Cl-Cl-C plane. A slightly higher minimum (**c**, 1.211 eV), also contained a CH_2CH_2Cl group, but has a Pt-C-C-Cl dihedral of 78°.

The fourth isomer (**d**, 1.372 eV) was found, where one hydrogen atom had been partially abstracted from the ethylene unit.

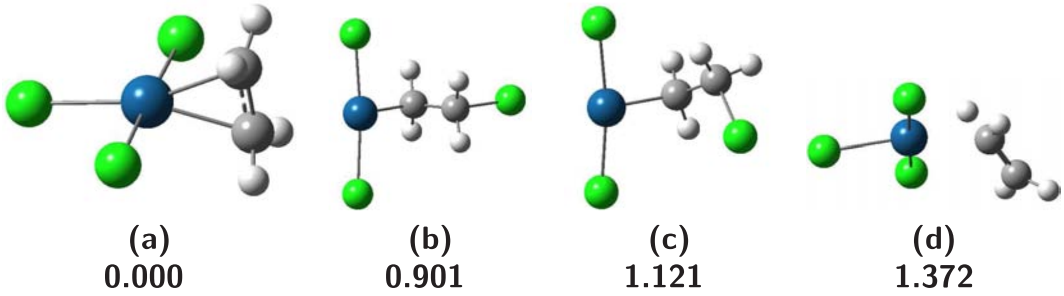

Figure 5.1: $[PtCl_3(C_2H_4)]^-$ structures identified in a Kick run employing an ethylene fragment. Relative energies are given in eV.

The more general approach to exploring the $[PtCl_3(C_2H_4)]^-$ potential energy surface is to supply Kick with no preconceived fragments, simply the required 10 atoms. Some 10000 jobs were run, resulting in 422 successful jobs of which 394 gave unique energies. The lowest two geometries from the fragment run (Figure 5.1 **a** and **b**) were replicated. Several of the "successful" geometries had energies 5 - 13 eV above the global minimum, on inspection, these turned out to have nonsensical geometries where one or more atoms had been placed in a far corner of the box and thus did not participate in any bonding interactions. In several cases HCl, Cl_2 and CH_n fragments were formed. Significant minima from this run are listed in Figure 5.2.

As was hoped, this approach identified not only the global minimum, Zeise's anion, but all possible substituted isomers. Three isomers (**e**, 1.298; **f**, 1.499 eV and **i**, 1.753 eV) were found where one of the ethylene hydrogen atoms was substituted by a chlorine atom. A total of five geometries where two ethylene hydrogens had been substituted were found, three of these had the chlorine atoms attached to a single carbon atom (**r**, 3.437 eV; **s**, 3.553 eV and **u**, 3.884 eV), the other two had one chlorine atom attached to each carbon atom (**p**, 3.345 eV and

t, 3.723 eV). The tri-substituted isomer, **v**, was found to have an energy 5.368 eV above the global minimum.

In structure **g** (1.549 eV) one hydrogen atom has migrated to the metal atom, leaving a $CHCH_2$ ligand bound by the unsaturated carbon atom.

Several structures in which a mono-substituted ethane ligand binds to the central platinum atom were found (**b**, 0.901 eV; **c**, 0.974 eV and **d**, 1.212 eV). The first of these is the second lowest energy structure (**b**, 0.901 eV) which was identified in the fragment run. The fact that the other two minima were not identified in the 394 unique jobs, despite several close analogues being identified, indicates the complexity of the PES around the Pt-C bond. More jobs, perhaps with a more restrictive box size would identify these minima.

Two structures with di-substituted ethane ligands, **j** and **k**, were identified at 2.145 and 2.163 eV above the global minimum respectively. Other interesting minima identified and shown in Figure 5.2 were an acetylene complex (**q**, 3.370 eV), a complex with a H_2 fragment (**o**, 2.847 eV) and several complexes with HCl fragments (**h**, 1.706; **m**, 2.548 and **n**, 2.681 eV).

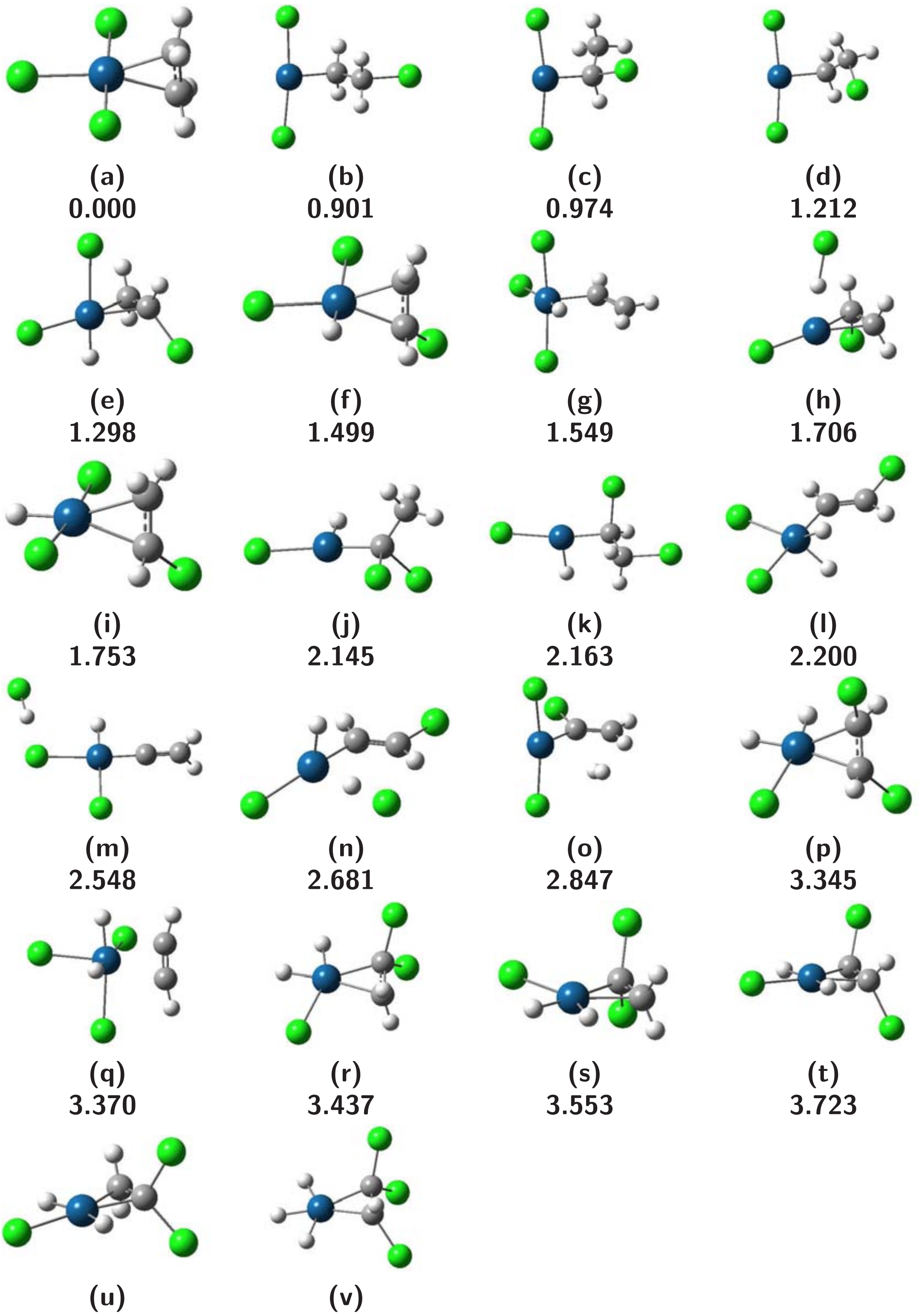
(a) 0.000 (b) 0.901 (c) 0.974 (d) 1.212 (e) 1.298 (f) 1.499 (g) 1.549 (h) 1.706 (i) 1.753 (j) 2.145 (k) 2.163 (l) 2.200 (m) 2.548 (n) 2.681 (o) 2.847 (p) 3.345 (q) 3.370 (r) 3.437 (s) 3.553 (t) 3.723 (u) 3.884 (v) 5.368

Figure 5.2: $[PtCl_3(C_2H_4)]^-$ structures identified in a Kick run where all 10 atoms were supplied individually. Relative energies are given in eV.

5.3 Au_6, $Au_6 + CO$, $Au_6 + O_2$, $Au_6 + CO + O_2$

Six Au atoms were kicked into a 6 Å cube, with the global minimum thus obtained agreeing with the previously established structure of a planar "triangle-within-a-triangle" geometry as shown in Figure 5.3 **a** [190, 191]. This isomer was identified more than a dozen times in 100 jobs. Two other isomers with a relative energy of < 1.0 eV are shown in Figure 5.3 and their energies listed in Table 5.1. A subsequent search, using a 6 × 6 × 1 Å box (i.e. essentially planar) did not discover any new geometries but had a higher yield of successful jobs. Only singlet species were kicked. The lowest energy cluster (Figure 5.3 **a**) was then treated as a fragment in further kick runs with the small molecules, CO and O_2. In each run, one half of the jobs were run with the small molecule also treated as a molecular fragment and in the other half, the atoms were kicked in separately. This approach ensures that both associatively bound and dissociatively bound minima are located for each Au_6 - molecule adduct. It was found that kicking in separate atoms often led to an associatively bound minimum, in contrast, it was rare for the geometry optimisation to dissociate a small molecule fragment. Therefore, one needs to be aware that if a dissociative structure is the global minimum, then it may not be located when fragments are employed. In the case of Au_6CO_3, all possible permutations of CO and O_2, and their respective atoms, were kicked with the global minimum of Au_6 (Figure 5.3 **a**).

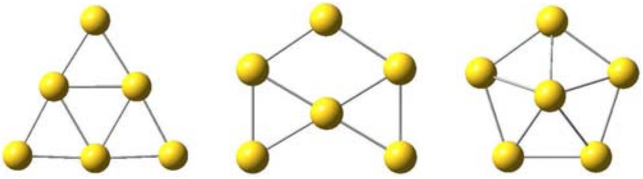
(a) **0.000** **(b)** **0.564** **(c)** **0.856**

Figure 5.3: Au_6 structures with a relative energy of < 1.0 eV identified in a Kick run. Relative energies are given in eV.

Isomer	Total E (Hartree)	$E_e + E_v$	Rel. E (eV)
Figure 5.3 **a**	-817.51011	-817.50757	0.000
Figure 5.3 **b**	-817.48926	-817.48683	0.564
Figure 5.3 **c**	-817.47840	-817.47610	0.856

Table 5.1: Total energies (hartree), zero-point energies ($E_e + E_v$, hartree) and relative energies (eV) of selected low-energy isomers of Au_6.

5.3.1 Au_6CO

Some 150 jobs identified 18 unique minima. Five of these minima had relative energies below 1.0 eV and are shown in Figure 5.4 and their energies listed in Table 5.2. The global minimum of Au_6CO is found to be a planar, associatively bound structure with CO binding to one of the apex atoms of the Au_6 cluster (Figure 5.4 **a**). This structure agrees closely with the C_{2v} structure of Wang *et al.* [192]. A structure with the CO moiety bent relative to the Au_6 cluster is found to be only 0.024 eV higher in energy (Figure 5.4 **b**); this structure was proposed as the global minimum by Fernandez *et al.* [193]. In Figure 5.4 **c**, CO binds to an edge Au atom resulting in the Au_6 cluster losing planarity and the cluster adopting a boot-like geometry that is 0.359 eV above the global minimum. Structures **d** and **e** have no formal Au-C or Au-O bonds and are possible candidates for the “capture species”. The lowest energy dissociatively bound structure is found 4.394 eV above the global minimum and is a planar structure with C and O atoms μ^2 bound either side of the apex of a distorted Au_6 cluster (not listed in Table 5.2).

5.3.2 Au_6O_2

As the ground state of the O_2 molecule is a triplet, both singlet and triplet surfaces were kicked. After 100 jobs at each multiplicity, minima on the triplet surface were found to be universally lower in energy than corresponding minima on the singlet surface (by 0.6 - 1.0 eV) and therefore only the triplet surface was considered further. A total of 300 jobs identified 17

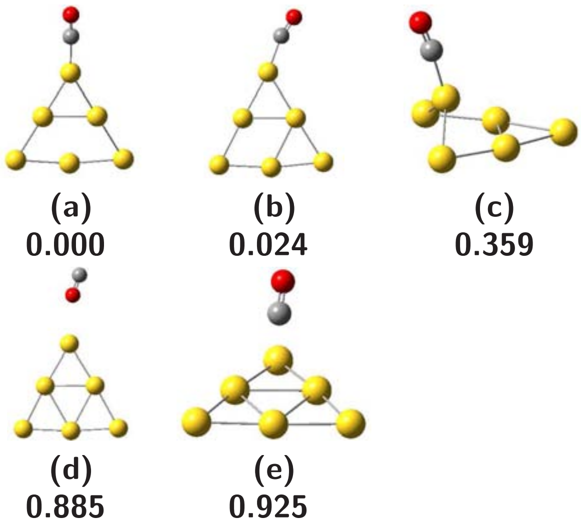
(a) 0.000
(b) 0.024
(c) 0.359
(d) 0.885
(e) 0.925

Figure 5.4: Au_6CO structures with a relative energy of < 1.0 eV identified in a Kick run. Relative energies are given in eV.

Isomer	Total E (Hartree)	$E_e + E_v$	Rel. E (eV)	Δ E (eV)	CO Frequency (cm^{-1})
Figure 5.4 **a**	-931.06675	-931.05755	0.000	-1.027	2063
Figure 5.4 **b**	-931.06595	-931.05666	0.024	-1.003	2055
Figure 5.4 **c**	-931.05359	-931.04435	0.359	-0.668	2037
Figure 5.4 **d**	-931.03277	-931.02501	0.885	-0.142	2030
Figure 5.4 **e**	-931.03104	-931.02354	0.925	-0.101	2032

Table 5.2: Total energies (hartree), zero-point energies ($E_e + E_v$, hartree) and relative energies (eV) of selected low-energy isomers of Au_6CO. The fifth column indicates the stabilization with respect to $E_{Au_6} + E_{CO}$. The final column shows the harmonic CO frequency (*c.f* ν_{CO} 2047 cm^{-1}).

unique minima; those with relative energies < 0.5 eV above the global minimum are shown in Figure 5.5 and their energies are listed in Table 5.3. The global minimum of Au_6O_2 is found to be a planar structure with dissociatively bound oxygen in agreement with the calculations of Yoon *et al.* and those of Fernandez *et al.* [193, 194] and is shown in Figure 5.5 **a**. Notable in this structure is that the baseline of the Au_6 triangle is distorted upwards. The lowest energy structure with associatively bound O_2 is 0.325 eV above the global minimum (Figure 5.5 **b**). Structures **c**, **d**, **f**, **g** and **i** all possess an O_2 molecule that is not formally bound to the cluster. The fifth structure has abstracted the "tip" Au atom and has an O-Au-O unit rising out of the Au_5 plane. Structure **h** appears to be an intermediate structure, where one oxygen atom resides in a similar position to that of **a** (and one Au-Au bond has been broken), however the

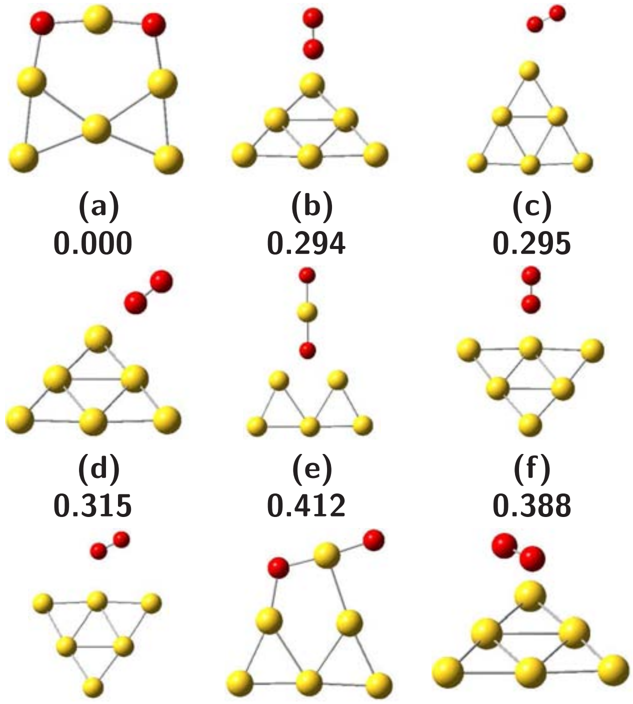

(a) **0.000** **(b)** **0.294** **(c)** **0.295**

(d) **0.315** **(e)** **0.412** **(f)** **0.388**

(g) **0.394** **(h)** **0.415** **(i)** **0.403**

Figure 5.5: Au_6O_2 structures with a relative energy of < 0.5 eV identified in a Kick run. Relative energies are given in eV.

second oxygen atom is only bound to one gold atom.

5.3.3 Au_6CO_3

All possible configurations were kicked for this system (i.e. Au_6 + CO_3, Au_6 + CO + O_2, Au_6 + CO, + O + O, Au_6 + C + O + O_2, Au_6 + C + O + O + O, Au_6CO + O + O and Au_6O_2 + C + O). No previous work on neutral Au_6 + CO + O_2 is known. For each configuration, a minimum of 250 jobs were run. As in the case of Au_6O_2, both singlet and triplet surfaces were kicked and since equivalent triplet structures had energies significantly greater (≈ 0.8 eV) than the singlet, only the singlet surface is considered further. The three lowest energy structures for each kicked configuration are presented in Figure 5.6 and Table 5.4. The global minimum is Figure 5.6 **s**.

Isomer	Total E (Hartree)	$E_e + E_v$	Rel. E (eV)	Δ E (eV)	O_2 Frequency (cm^{-1})
Figure 5.5 **a**	-968.11991	-968.11209	0.000	-0.513	
Figure 5.5 **b**	-968.10798	-968.10130	0.294	-0.219	1371
Figure 5.5 **c**	-968.10791	-968.10124	0.295	-0.217	1373
Figure 5.5 **d**	-968.10713	-968.10052	0.315	-0.198	1390
Figure 5.5 **e**	-968.10447	-968.09694	0.412	-0.100	
Figure 5.5 **f**	-968.10428	-968.09782	0.388	-0.124	1432
Figure 5.5 **g**	-968.10397	-968.09763	0.394	-0.119	1437
Figure 5.5 **h**	-968.10392	-968.09685	0.415	-0.098	
Figure 5.5 **i**	-968.10353	-968.09730	0.403	-0.110	1494

Table 5.3: Total energies (hartree), zero-point energies ($E_e + E_v$, hartree) and relative energies (eV) of selected low-energy isomers of Au_6O_2. The fifth column indicates the stabilization with respect to $E_{Au_6} + E_{O_2}$. The final column shows the harmonic O_2 frequency (*c.f* ν_{O_2} 1482 cm^{-1}).

Isomer	Total E (Hartree)	$E_e + E_v$	Rel. E (eV)	Δ E (eV)	Highest Frequencies (cm^{-1})
Figure 5.6 **a**	-1081.67241	-1081.65638	2.110	-1.385	639,764,2101
Figure 5.6 **b**	-1081.66067	-1081.64485	2.424	-1.071	554,827,2090
Figure 5.6 **c**	-1081.64708	-1081.63145	2.789	-0.706	565,857,1907
Figure 5.6 **d**	-1081.69919	-1081.68230	1.405	-2.090	913,1010,1660
Figure 5.6 **e**	-1081.67283	-1081.65668	2.102	-1.393	685,801,2100
Figure 5.6 **f**	-1081.64264	-1081.62648	2.924	-0.571	868,960,1662
Figure 5.6 **g**	-1081.73764	-1081.72036	0.369	-3.126	601,1307,2362
Figure 5.6 **h**	-1081.73294	-1081.71587	0.491	-3.004	631,1300,2348
Figure 5.6 **i**	-1081.71867	-1081.70224	0.862	-2.633	617,1280,2308
Figure 5.6 **j**	-1081.73752	-1081.72028	0.372	-3.124	592,1309,2365
Figure 5.6 **k**	-1081.73269	-1081.71552	0.501	-2.994	632,1305,2355
Figure 5.6 **l**	-1081.71910	-1081.70262	0.852	-2.643	619,1281,2309
Figure 5.6 **m**	-1081.73762	-1081.72034	0.370	-3.125	603,1307,2361
Figure 5.6 **n**	-1081.70010	-1081.68351	1.372	-2.123	575,762,2088
Figure 5.6 **o**	-1081.69985	-1081.68344	1.374	-2.121	577,707,2091
Figure 5.6 **p**	-1081.65890	-1081.64378	2.453	-1.042	586,658,2073
Figure 5.6 **q**	-1081.63707	-1081.62214	3.042	-0.453	562,627,2094
Figure 5.6 **r**	-1081.62358	-1081.60806	3.425	-0.070	563,637,1810
Figure 5.6 **s**	-1081.75271	-1081.73393	0.000	-3.495	1036,1316,1472
Figure 5.6 **t**	-1081.74124	-1081.72357	0.282	-3.213	802,1069,1467
Figure 5.6 **u**	-1081.73602	-1081.71825	0.427	-3.068	918,1051,1603

Table 5.4: Total energies (hartree), zero-point energies ($E_e + E_v$, hartree) and relative energies (eV) of the three lowest energy isomers of each Au_6CO_3 Kick run. The fifth column indicates the stabilization with respect to $E_{Au_6} + E_{CO} + E_{O_2}$. The final column shows the three highest harmonic freqencies. Structure **s** is the global minimum.

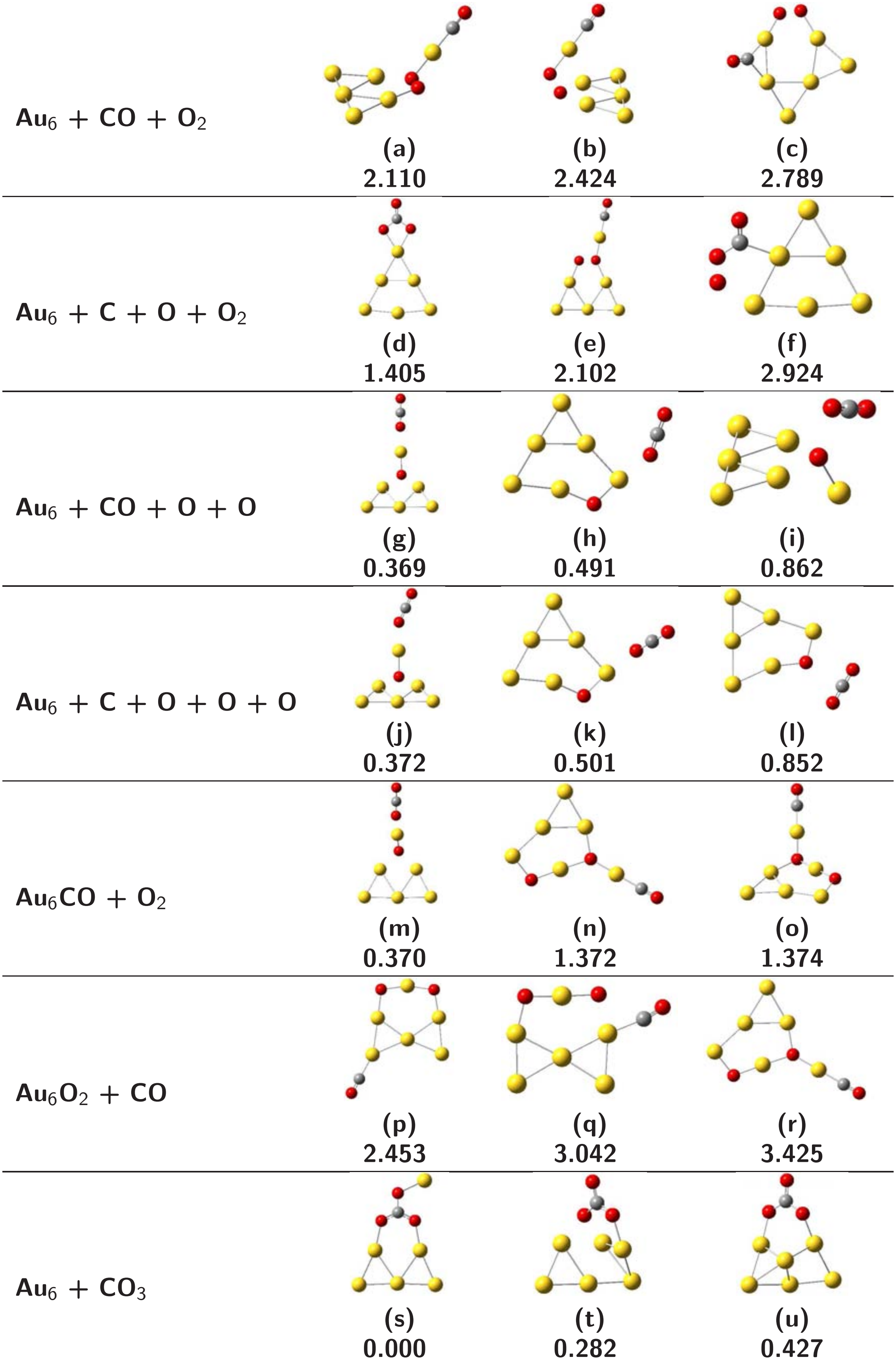

Figure 5.6: Au_6CO_3 structures identified in several Kick runs. Relative energies are given in eV.

Kicking three molecular fragments (Au_6, CO and O_2) resulted in three high energy structures, 2.1-2.8 eV above the global minimum (**s** in Figure 5.6 and Table 5.4 above). Both Figure 5.6 **a** and Figure 5.6 **b** abstract a single gold atom away from Au_6, and differ only in the orientation of the CO group (toward or away) relative to the Au_5 plane. Figure 5.6 **c** retains the Au_6 cluster and binds CO and O_2 on either side of the Au_6 triangle.

Breaking the CO fragment into its constituent atoms (i.e. kicking Au_6, O_2, C and O) again results in high energy isomers, 1.4-2.9 eV above the global minimum. Here, the lowest energy structure formed (Figure 5.6 **d**) contains a carbonate unit bound to an apex gold atom. Figure 5.6 **e** is very similar to Figure 5.6 **a** and **b**, again differing only in the orientation of the CO moiety relative to the gold cluster. Figure 5.6 **f** is a structure where CO has partially abstracted an oxygen atom from O_2, resulting in a CO_2 bound to the Au_6 cluster with the remaining oxygen atom forming a bridge to an apex gold atom.

Breaking the O_2 and kicking Au_6, CO, O and O yields three interesting low energy isomers, 0.5-0.9 eV above the global minimum, that possess CO_2 units. The lowest energy isomer (Figure 5.6 **g**) has a linear CO_2 group and an O atom inserted into the gold cluster. Alternatively it can be considered as a gold atom being abstracted from the cluster. Figure 5.6 **i** is similar but with a differing orientation of the CO_2 group and Figure 5.6 **h** also has a CO_2 unit but the extra oxygen atom is bound to two gold atoms.

Kicking Au_6 with four atoms (i.e. $Au_6 + C + O + O + O$) also results in low energy isomers, Figure 5.6 **j** - **l** that are 0.4-0.9 eV above the global minimum. These have very similar energy and structure to those described immediately above, in that free CO_2 is created and the remaining O atom lies partially or completely embedded into the gold cluster.

For the next two configurations we considered the global minimum of Au_6CO (i.e. Figure 5.4 **a**) and the global minimum of Au_6O_2 (i.e. Figure 5.5 **a**) and kicked in individual atoms. For $Au_6CO + O + O$, the lowest energy structure, Figure 5.6 **m**, yielded essentially the same structure as Figure 5.6 **g** and Figure 5.6 **j** and is 0.370 eV above the global minimum. The other two structures (Figure 5.6 **n** and **o**) were both ≈1.37 eV higher in energy and both contained partially inserted O atoms.

Kicking Au_6O_2 with C and O atoms resulted in structures that largely retained the Au_6O_2 moiety and the CO group bound to a different part of the cluster. All are quite high in energy, 2.5-3.4 eV above the global minimum. Figure 5.6 **p** binds CO to one of the two equivalent base gold atoms, Figure 5.6 **q** binds CO in one of the two equivalent edge positions and Figure 5.6 **r** has CO bound to an abstracted gold atom.

The final combination considered was kicking Au_6 with CO_3, which resulted in the lowest energy structure of all combinations (Figure 5.6 **s**), as well as other low energy structures (at 0.282 and 0.427 eV, respectively). As seen in Figure 5, the global minimum has the CO_3 inserting into the Au_6 cluster and pushing out a gold atom. Both Figure 5.6 **t** and **u** are structures where the Au_6 cluster has rearranged to a 3-dimensional configuration with an approximately triangular face to which CO_3 binds.

For many of the low energy minima identified in this section, it is difficult to say whether these are parts of the potential energy surface that would be accessed in any real chemical interaction between Au_6, CO and O_2. It has been shown such a reaction involving gas phase Au_2 anions forms $Au_2CO_3^-$ and corresponding computational work shows the global minimum to have a carbonate moiety [195, 196]. Similar gas phase reactions are observed for larger gold cluster anions, particularly Au_6^-, which exhibit cooperative coadsorption to produce CO_2 [197]. It is also known that Au_8, and larger clusters, deposited onto MgO surfaces oxidize

CO to CO_2[133]. Furthermore, the theoretical investigation of this work proposes that an important part of the CO oxidation involves the gold atoms significantly changing geometry [133]. Therefore, the low energy 3-dimensional structures identified here (i.e. Figure 5.6 **t** and **u**) may well be a critical part of the PES. However, it will require careful linking between minima and transition states if one is to start computationally exploring the reaction dynamics of such interactions.

5.4 Gly-Trp.nH_2O n = 1,2

To further test the fragment capability of Kick on other types of molecule-molecule complexes, such as hydrogen bonded clusters, a system entirely composed of fragments was considered. To facilitate comparison of structures, gas phase calculations were used in favour of crystal structures as crystal structures are likely to be mediated by inter-peptide hydrogen bonds.

The conformation of a flexible biological molecule, such as either of the dipeptides studied depends on a number of factors, including intramolecular hydrogen bonding, electrostatic interactions and intermolecular interactions with the molecules in the first solvation shell. These intermolecular interactions can play a strongly important role in dictating the conformational stability of flexible molecules, particularly in hydrogen bonding solvents such as water. The presence of both hydrogen bond donor and acceptor sites allows water molecules in the first solvation sphere to form water bridges [198], which may alter the conformational preference of the dipeptide. Several possible sites for hydrogen bonding exist on the dipeptide backbone, viz. -COOH, Glycine NH_2, Tryptophan π cloud, Tryptophan NH and the CONH moiety.

The two lowest energy conformers of the Gly-Trp dipeptide (differing in the orientation of the -COOH group) were taken from the B3LYP/6-31g(d,p) calculations of Hünig [199] and reoptimized at the RHF/6-311g(d) level. The ΔE (including ZPE) of the two bare dipeptides was 0.063 eV and they are hereafter referred to as Isomer A and Isomer B. Each dipeptide was then kicked with one or two water molecules. A box size of $7 \times 7 \times 7$ Å was chosen to include the entire dipeptide, thus allowing enough space for the water molecule(s) to be placed at any position relative to the dipeptide.

The rich chemistry expected of these systems, provides an ideal test for Kick.

For isomer A of Gly-Trp.H_2O, 100 jobs were run, of which 45 completed successfully, yielding 12 unique isomers within 0.3 eV that are listed in Table 5.5. As expected, the most favourable place for a single water molecule to bind is the carboxylic acid group of the Trp residue where the water molecule is able to bridge the carboxylic acid group and form two hydrogen bonds, as shown in Figure 5.7. Structures where the water molecule formed only one hydrogen bond to the carboxylic acid group were the highest in energy identified, 0.285 (A(H_2O) **k**) and 0.286 (A(H_2O) **l**) eV above the global minimum.

For Gly-Trp.H_2O Isomer B, 100 jobs, of which 62 completed, yielded 19 unique isomers which are listed in the second half of Table 5.5. The lowest energy configuration, B(H_2O) **a**, lies 0.081 eV above the global minimum (i.e. A(H_2O) **a**) and like that structure has the water molecule forming two hydrogen bonds to the carboxylic acid moiety. It is worth noting that the relative energy between the two isomers has increased slightly compared to the energy difference between the unsolvated Gly-Trp isomers (i.e. 0.063 cf. 0.081 eV). The next group of structures (A(H_2O) **a** - **e**) formed hydrogen bonds to the glycine residue. The highest energy group of structures (A(H_2O) **q** - **s**) have the water binding to the underside of the aromatic plane.

A total of 400 Gly-Trp.2H_2O (Isomer A) jobs were run. The fourth 50 job batch did not result in any significant new isomers, though on several occasions, "repeats" of previously identified isomers with energies varying by < 0.003 eV were identified. In these instances, only the lowest energy isomer is presented. The global minimum structure is shown in Figure 5.7. Overall, a total of 22 minima were identified and these are listed in Table 5.6. 19 of the identified isomers possessed a water bridging motif, with the two H_2O molecules linking two separate points on the Gly-Trp dipeptide. In some cases one water molecule migrated several Angstrom from its initial placement in order to form such a bridge. The two lowest energy structures, A(2H_2O) **a** and A(2H_2O) **b** (0.000 and 0.040 eV) have both water molecules clustered around the -COOH group of the Trp residue. The next group of structures, A(2H_2O) **c**, A(2H_2O) **d** and A(2H_2O) **e** (0.133, 0.153 and 0.165 eV) also possess a water bridge, the first water molecule is hydrogen bonded to the =O of Trp and the second links to the ring NH in Trp. The lowest energy of this group of minima has the first water molecule in a position where it can also form a weak hydrogen bond (viz. H$\cdots$O bondlength of 2.33 Å) with the terminal NH_2 of the Gly residue. In several cases, notably A($2H_2O$) **k** (0.246 eV), the dipeptide conformation significantly altered in order to accommodate the two-water bridge.

Another 400 Gly-Trp.$2H_2O$ jobs were run for Isomer B. A total of 46 isomers were found, listed in the second half of Table 5.6, of which only 26 possessed a two-water bridge. The global minimum (B($2H_2O$) **a**) has a two-water bridge linking the carboxylic acid group with the glycine oxygen atom and is shown in Figure 5.7. Structurally this isomer is different from the global minimum of Isomer A, (A($2H_2O$) **a**), however, the next isomer, B($2H_2O$) **b** is only 0.014 eV above B($2H_2O$) **a** and is analogous to A($2H_2O$) **a** in having both water molecules bridging the carboxylic acid group. The highest energy structures in this group (B($2H_2O$) **ap** - **at**) all possessed one water molecule binding to the underside of the aromatic plane. It is again worth noting that the energy difference between the two isomers of Gly-Trp.$2H_2O$ of 0.060 eV is almost identical to the bare dipeptide (i.e. 0.063 eV).

The two dipeptide conformers considered, A and B, differed only in the orientation of one group (the -COOH). Many more conformers would need to be "kicked" in order to be satisfied that the entire PES had been explored. Of particular interest would be the possibility of conformers interconverting when kicked with one or more water molecules and relative energies changing with increasing solvation. Neither of these effects were seen with the two conformers considered.

Isomer	Total E (Hartree)	$E_e + E_v$	Rel. E (eV)	Δ E (eV)
A(H_2O) **a**	-965.23590	-964.91261	0.000	-0.433
A(H_2O) **b**	-965.23218	-964.90904	0.101	-0.336
A(H_2O) **c**	-965.23108	-964.90827	0.131	-0.315
A(H_2O) **d**	-965.23048	-964.90787	0.147	-0.304
A(H_2O) **e**	-965.23039	-964.90779	0.150	-0.302
A(H_2O) **f**	-965.22877	-964.90682	0.194	-0.276
A(H_2O) **g**	-965.22868	-964.90548	0.196	-0.239
A(H_2O) **h**	-965.22860	-964.90615	0.199	-0.257
A(H_2O) **i**	-965.22824	-964.90585	0.208	-0.249
A(H_2O) **j**	-965.22811	-964.90495	0.212	-0.225
A(H_2O) **k**	-965.22542	-964.90367	0.285	-0.190
A(H_2O) **l**	-965.22540	-964.90341	0.286	-0.183
B(H_2O) **a**	-965.23291	-964.90966	0.000	-0.376
B(H_2O) **b**	-965.22938	-964.90654	0.085	-0.291
B(H_2O) **c**	-965.22861	-964.90541	0.116	-0.260
B(H_2O) **d**	-965.22799	-964.90559	0.111	-0.265
B(H_2O) **e**	-965.22790	-964.90539	0.116	-0.259
B(H_2O) **f**	-965.22756	-964.90508	0.125	-0.251
B(H_2O) **g**	-965.22750	-964.90403	0.153	-0.222
B(H_2O) **h**	-965.22749	-964.90500	0.127	-0.249
B(H_2O) **i**	-965.22724	-964.90437	0.144	-0.232
B(H_2O) **j**	-965.22686	-964.90423	0.148	-0.228
B(H_2O) **k**	-965.22617	-964.90446	0.142	-0.234
B(H_2O) **l**	-965.22614	-964.90436	0.144	-0.231
B(H_2O) **m**	-965.22610	-964.90309	0.179	-0.197
B(H_2O) **n**	-965.22515	-964.90334	0.172	-0.204
B(H_2O) **o**	-965.22262	-964.89993	0.265	-0.111
B(H_2O) **p**	-965.22177	-964.89973	0.270	-0.105
B(H_2O) **q**	-965.22060	-964.89928	0.282	-0.093
B(H_2O) **r**	-965.22031	-964.89905	0.289	-0.087
B(H_2O) **s**	-965.21938	-964.89873	0.297	-0.078

Table 5.5: Total energies (hartree),zero-point energies ($E_e + E_v$, hartree) and relative energies (eV) of Gly-Trp.H_2O. The fourth column gives energies relative to A(H_2O) **a**, while the fifth column gives energies relative to $E_{H_2O} + E_{Gly-Trp}$.Below the horizontal rule, all relative energies are given with respect to B(H_2O) **a**.

Isomer	Total E (Hartree)	$E_e + E_v$	Rel. E (eV)	Δ E (eV)
A(2H_2O) **a**	-1041.28817	-1040.93739	0.000	-0.856
A(2H_2O) **b**	-1041.28715	-1040.93592	0.040	-0.817
A(2H_2O) **c**	-1041.28412	-1040.93251	0.133	-0.724
A(2H_2O) **d**	-1041.28247	-1040.93176	0.153	-0.704
A(2H_2O) **e**	-1041.28113	-1040.93131	0.165	-0.692
A(2H_2O) **f**	-1041.28112	-1040.93130	0.166	-0.691
A(2H_2O) **g**	-1041.28081	-1040.93136	0.164	-0.693
A(2H_2O) **h**	-1041.28037	-1040.93024	0.195	-0.662
A(2H_2O) **i**	-1041.28032	-1040.92951	0.214	-0.643
A(2H_2O) **j**	-1041.27968	-1040.92869	0.237	-0.621
A(2H_2O) **k**	-1041.27940	-1040.92834	0.246	-0.611
A(2H_2O) **l**	-1041.27883	-1040.92806	0.254	-0.603
A(2H_2O) **m**	-1041.27858	-1040.92781	0.261	-0.596
A(2H_2O) **n**	-1041.27840	-1040.92749	0.269	-0.588
A(2H_2O) **o**	-1041.27826	-1040.92824	0.249	-0.608
A(2H_2O) **p**	-1041.27822	-1040.92832	0.247	-0.610
A(2H_2O) **q**	-1041.27800	-1040.92787	0.259	-0.598
A(2H_2O) **r**	-1041.27706	-1040.92759	0.267	-0.591
A(2H_2O) **s**	-1041.27467	-1040.92565	0.320	-0.538
A(2H_2O) **t**	-1041.27387	-1040.92356	0.376	-0.481
A(2H_2O) **u**	-1041.27327	-1040.92327	0.384	-0.473
A(2H_2O) **v**	-1041.27029	-1040.92243	0.407	-0.451
B(2H_2O) **a**	-1041.28613	-1040.93520	0.000	-0.822
B(2H_2O) **b**	-1041.28536	-1040.93469	0.014	-0.808
B(2H_2O) **c**	-1041.28055	-1040.92966	0.151	-0.672
B(2H_2O) **d**	-1041.27982	-1040.92934	0.159	-0.663
B(2H_2O) **e**	-1041.27973	-1040.92909	0.166	-0.656
B(2H_2O) **f**	-1041.27897	-1040.92872	0.176	-0.646
B(2H_2O) **g**	-1041.27874	-1040.92805	0.195	-0.628
B(2H_2O) **h**	-1041.27868	-1040.92892	0.171	-0.651
B(2H_2O) **i**	-1041.27851	-1040.92897	0.170	-0.653
B(2H_2O) **j**	-1041.27789	-1040.92673	0.230	-0.592
B(2H_2O) **k**	-1041.27759	-1040.92787	0.199	-0.623
B(2H_2O) **l**	-1041.27712	-1040.92686	0.227	-0.595
B(2H_2O) **m**	-1041.27708	-1040.92700	0.223	-0.599
B(2H_2O) **n**	-1041.27701	-1040.92759	0.207	-0.615
B(2H_2O) **o**	-1041.27687	-1040.92672	0.231	-0.592
B(2H_2O) **p**	-1041.27643	-1040.92662	0.233	-0.589
B(2H_2O) **q**	-1041.27631	-1040.92728	0.216	-0.607
B(2H_2O) **r**	-1041.27585	-1040.92522	0.272	-0.551
B(2H_2O) **s**	-1041.27516	-1040.92499	0.278	-0.544
B(2H_2O) **t**	-1041.27491	-1040.92392	0.307	-0.515
B(2H_2O) **u**	-1041.27476	-1040.92527	0.270	-0.552
B(2H_2O) **v**	-1041.27469	-1040.92514	0.274	-0.549

B(2H_2O) **w**	-1041.27432	-1040.92479	0.283	-0.539
B(2H_2O) **x**	-1041.27431	-1040.92442	0.293	-0.529
B(2H_2O) **y**	-1041.27406	-1040.92502	0.277	-0.545
B(2H_2O) **z**	-1041.27349	-1040.92346	0.319	-0.503
B(2H_2O) **aa**	-1041.27330	-1040.92330	0.324	-0.498
B(2H_2O) **ab**	-1041.27322	-1040.92319	0.327	-0.495
B(2H_2O) **ac**	-1041.27306	-1040.92400	0.305	-0.518
B(2H_2O) **ad**	-1041.27240	-1040.92396	0.306	-0.516
B(2H_2O) **ae**	-1041.27220	-1040.92322	0.326	-0.496
B(2H_2O) **af**	-1041.27207	-1040.92216	0.355	-0.467
B(2H_2O) **ag**	-1041.27190	-1040.92300	0.332	-0.490
B(2H_2O) **ah**	-1041.27181	-1040.92231	0.351	-0.472
B(2H_2O) **ai**	-1041.27180	-1040.92242	0.348	-0.475
B(2H_2O) **aj**	-1041.27166	-1040.92294	0.334	-0.489
B(2H_2O) **ak**	-1041.27025	-1040.92114	0.383	-0.440
B(2H_2O) **al**	-1041.27019	-1040.92139	0.376	-0.447
B(2H_2O) **am**	-1041.26985	-1040.92149	0.373	-0.449
B(2H_2O) **an**	-1041.26892	-1040.91911	0.438	-0.384
B(2H_2O) **ao**	-1041.26693	-1040.91781	0.473	-0.349
B(2H_2O) **ap**	-1041.26689	-1040.91842	0.457	-0.366
B(2H_2O) **aq**	-1041.26563	-1040.91783	0.473	-0.350
B(2H_2O) **ar**	-1041.26541	-1040.91855	0.453	-0.369
B(2H_2O) **as**	-1041.26470	-1040.91609	0.520	-0.302
B(2H_2O) **at**	-1041.26467	-1040.91703	0.494	-0.328

Table 5.6: Total energies (hartree), zero-point energies ($E_e + E_v$, hartree) and relative energies (eV) of Gly-Trp.(H_2O)$_2$. The fourth column gives energies relative to A(2H_2O) **a**, while the fourth column gives energies relative to $2 \times E_{H_2O} + E_{Gly-Trp}$. Below the horizontal rule, all relative energies are given with respect to B(2H_2O) **a**.

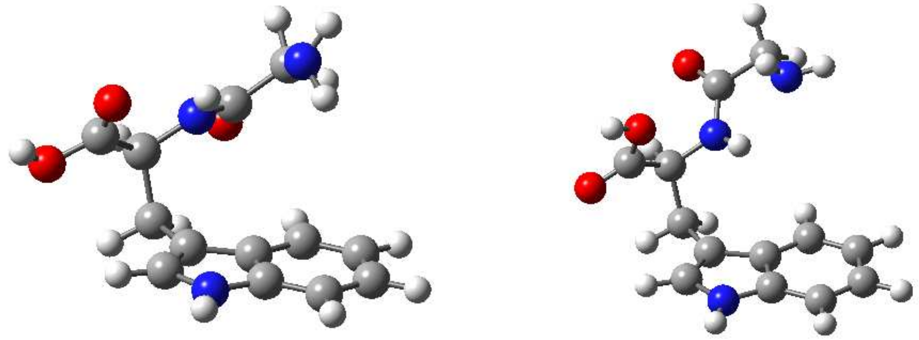

Gly-Trp (A)
-889.18519

Gly-Trp (B)
-889.18273

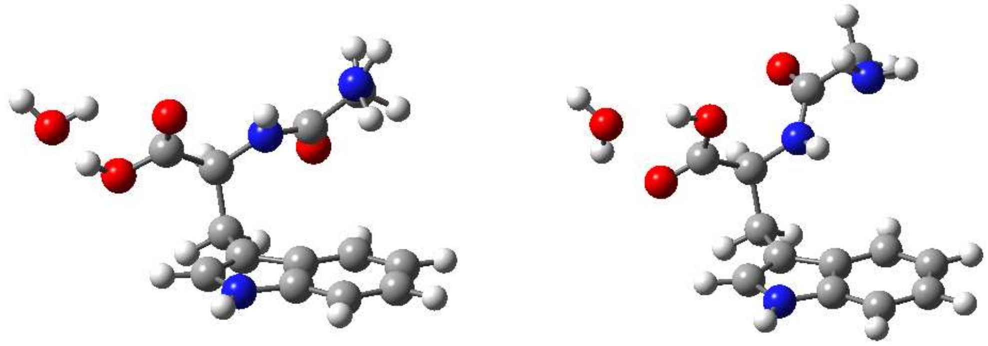

Gly-Trp.H_2O (A)
-965.23590

Gly-Trp.H_2O (B)
-965.23291

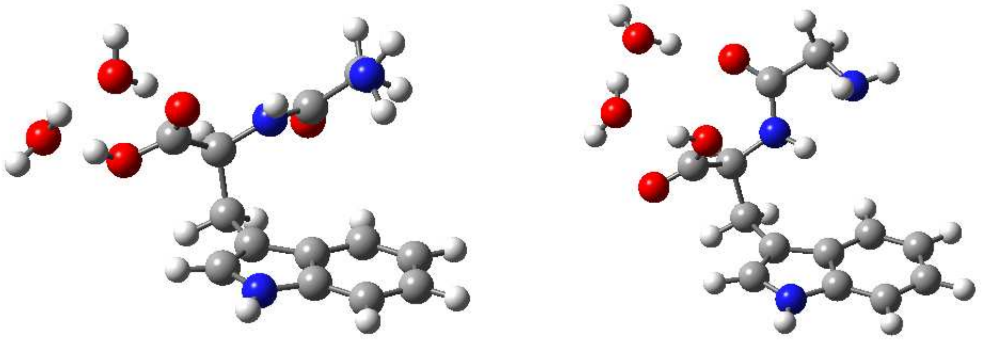

Gly-Trp.$(H_2O)_2$ (A)
-1041.28817

Gly-Trp.$(H_2O)_2$ (B)
-1041.28613

Figure 5.7: Structures and total energies (hartree) of Gly-Trp.nH_2O n = 1,2 A and B isomers. The bare dipeptides are shown in the top row for reference.

Chapter 6

Changing cluster properties, one atom at a time: Nb_3X

DENSITY functional calculations were performed to determine the equilibrium structures, ionization potentials and electron affinities of Nb_3X clusters (X = Na, Al, Sc, Sr, Y, Zr, Nb , Mo, Tc, Ru, Rh, Pd, Ag, Cd). Pseudo-tetrahedral geometries were preferred for all Nb_3X clusters except Nb_3Cd. The equilibrium structures and binding energies of the associatively and dissociatively bound products of the Nb_3X + CO reaction were calculated at the same level of theory. All clusters were found to thermodynamically dissociate CO. Only Nb_3Al and Nb_3Cd reduced the enthalpy of dissociation, relative to Nb_4 whereas all other heteroatoms increased it.

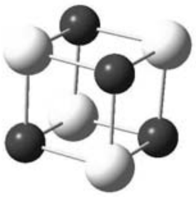

6.1 Introduction

The reaction of CO with transition metal clusters has been the subject of many experimental [60, 62, 64, 200, 201] and computational [18, 76, 77, 91, 202, 203] studies. It is known that bulk metals located on the left hand side of a diagonal line comprised of Co, Ru and Re dissociate CO at room temperature [204]. However, it is less well established whether this holds for small transition metal clusters. Of the $4d$ transition metals, niobium clusters have been previously shown by experiment and computation to thermodynamically dissociate CO [25], whereas rhodium clusters bind CO associatively [26, 62]. Our recent calculations show that CO dissociation is preferred for $4d$ transition metal trimers to the left of (and including) Tc_3.[205]

It was sought to further probe the circumstances of CO dissociation and to determine whether CO dissociation on early transition metal clusters may be prevented. Both the geometric and the electronic structure of the cluster may be perturbed by the addition of an impurity atom, which in turn may influence the behaviour of adsorbed species. Investigation of a related series of doped clusters thus permits elucidation of the key influences on cluster properties and reactivity. Several experimental [206–209] and computational [210–213] studies have used this approach and highlighted the effect of impurity atoms on both the structural properties and reactivity of a cluster. Experimental work by Kaya *et al.* [214] shows that the addition of a single aluminium atom to Nb_n, (n=4-7) clusters decreases their reactivity with H_2 by a factor of 3 and that further addition of aluminium decreases the reaction rate even further. Heiz *et al.* [215] measured the reactivity of Au_n and Au_nSr clusters ($1 \leq n \leq 9$) deposited on MgO surfaces and found that Au_3Sr binds O_2 by 1.94 eV, whereas Au_4 only binds O_2 by 0.18 eV. This increased binding results in a threefold increase in reaction rate for the oxidation of CO ($CO + \frac{1}{2} O_2 \rightarrow CO_2$). Finally, a DFT study by Jena and co-workers [179] investigated several Au_5M clusters and found that they could radically alter the geometric structure of the cluster, depending on the characteristics of the single dopant atom. In this study, impurity atoms with

p electrons (Al, Si and P) formed non-planar structures, whereas dopants with only s (Na and Mg) electrons in their outer shell retained planar structures.

An alternative approach to preventing CO dissociation (on early transition metal clusters) relies on the premise that, when dissociated, it necessarily occupies two binding sites, whereas associatively bound CO only occupies a single site. Using a co-adsorbant species to block binding sites therefore can prevent CO dissociation, simply by occupying the adjacent binding sites necessary for dissociation. A computational study of CO dissociation on $3d$ transition metal clusters proposed that tilted-bridge (η^2) structures are necessary for the dissociative adsoprtion of CO.[216] Since the metal carbide and metal oxide bonds are stronger than the CO bond, early transition metal clusters with two three-fold binding sites (triangular faces) free to accommodate the C and O atoms, will thermodynamically dissociate CO. Conversely, any early transition metal cluster with all faces blocked, cannot form an η^2(CO) motif and therefore cannot dissociate CO. Recent research on analogous vanadium clusters has employed this " site-blocking" approach, using hydrogen adsorption to prevent dissociation of adsorbed CO [217] This study succeeded in preventing CO dissociation only when the three-fold binding sites on the cluster were fully blocked by hydrogen atoms.

To determine whether this "site-blocking" approach of blocking dissociation opportunities is necessary to prevent CO dissociation, the binding of CO to a series of doped niobium clusters was investigated. The simplest possible 3-dimensional model system was chosen, Nb_4. Nb_4 has been previously determined to have a tetrahedral structure [108] and therefore, substitution of one niobium atom will therefore leave one Nb_3 face and create one or more (three if the tetrahedral shape is maintained) Nb_2X faces. Two possible mechanisms for disrupting the dissociation behaviour of CO are thus explored: (a) If CO preferentially binds to the heteroatom and the heteroatom does not back-donate sufficient electron density to the CO bond. (b) If the heteroatom is able to remove sufficient electron density from the Nb_3 moiety, such that Nb_3 can not back-donate sufficient electron density to the CO bond (i.e. altering the energies of the cluster HOMO and LUMO).

6.2 Computational Method

Nb_3X clusters, for X = Na, Al, Sc, Sr, Y, Zr, Nb (i.e. Nb_4) , Mo, Tc, Ru, Rh, Pd, Ag, Cd and their reactions with CO were investigated. No previous experimental or computational work exists on these systems. Calculations were undertaken using the B3P86 functional in Gaussian03 [78] and all atoms were treated with the sdd basis set.

Niobium is an odd-electron ($4d^4.5s^1$) species, therefore Nb_3 is also an odd-electron species. Previous studies [82, 205, 218] have shown the ground state of Nb_3 to be a doublet. Addition of a fourth niobium atom to form Nb_4 results in a singlet ground state [108]. The substitiution of the fourth niobium atom with any odd-electron atom (e.g. Na, Al, Sc, Y, Nb, Tc, Rh, Ag) will likewise result in an even-electron Nb_3X species. For these even electron Nb_3X species, singlets and triplets were investigated. Only Nb_4 and Nb_3Tc were found to be singlets, all other even electron Nb_3X species were found to have triplet ground states. Doublet and quartet multiplicities were investigated for cationic species, the former was found to be the ground state in all cases. As with the cationic species, doublet and quartet multiplicities were investigated for the anionic species, remembering the restriction that the $\Delta S = \pm 1/2$ selection rule be met. Nb_4^- was found to have a doublet ground state, all other anionic species were found to be quartets.

Conversely, substitution of the fourth atom with an even-electron species (e.g. Sr, Zr, Mo, Ru, Pd, Cd) yields an odd-electron Nb_3X species, meaning that doublet and quartet states were investigated. Only Nb_3Sr had a quartet ground state, all others being doublets. Owing to the $\Delta S = \pm 1/2$ selection rule, it is possible for cationic or anionic Nb_3Sr species to be quintets, however the ground state for both the cation and anion of this species was found to be a triplet. For all other cationic species, singlet and triplet multiplicities were investigated and all ground states were found to be triplets. For the anionic species, Nb_3Zr was found to have a singlet ground state, all other species investigated were found to be triplets.

Although it is anticipated that most Nb_3X structures would have the heteroatom sitting over the Nb_3 face, in a pseudo-tetrahedral geometry, we also explored the possibility of other binding sites. A local implementation of Bera's Kick procedure [157], which we have previously described [219], was used to locate the lowest energy structure for each stoichiometry. This approach permits pre-defined fragments to be kicked. A kick run with three niobium atoms plus each heteroatom was repeated for the multiplicities described above, and the lowest energy minima were chosen. In all cases a distinct Nb_3 triangular face was formed. To determine the adiabatic Ionization Potential, (IP) and Electron Affinity, (EA) of the bare Nb_3X clusters, cationic and anionic structures were optimized using the neutral geometries as starting guesses. These IPs and EAs can be used as a gross indicator of the energy of the HOMO and LUMO respectively.

The previously determined lowest energy Nb_3X cluster was then defined as a fragment in two further kick runs, firstly with a carbon monoxide fragment (i.e. $Nb_3X + CO$) and secondly with carbon and oxygen atoms (i.e. $Nb_3X + C + O$). Again the lowest two multiplicities were investigated. As each system had three identical atoms, 100 - 200 kick jobs was found to be sufficient with no new minima being generated in any further runs of 50 jobs. Binding energies are calculated relative to *zero energy* which is the sum of the energies of the separated metal cluster an carbon monoxide.

No symmetry constraints were imposed on any of the geometries, however examination of several of the optimised structures indicated symmetry greater than C_1. In these cases, we assume the higher point group but we denote it with an asterisk, e.g. C^*_{3v}, as we have described previously [124]. Frequency calculations were used to confirm the nature of all unique geometries. Energies and cartesian coordinates of all structures are provided in the Supplementary Material.

Associative and dissociative binding energies were calculated with respect to the sum of the energies of the Nb_3X cluster and CO, regardless of multiplicity. The energy of CO was determined with the same method and basis set, yielding an absolute energy of -113.5163078 hartree. The optimised bond length is 1.164 Å, which yields an harmonic vibrational frequency of 2046 cm^{-1} (cf. the experimental value of 2169.8 cm^{-1}). [220]

6.3 Results and Discussion

6.3.1 Bare Clusters

All bare Nb_3X neutral structures, with the exception of Nb_3Cd, retained pseudo-tetrahedral structures as shown in Figure 6.1 (arranged in order of increasing atomic number of X). The lowest energy structure of Nb_3Cd is a planar butterfly (C^*_{2v} symmetry) with the cadmium atom occupying one wingtip. Nb_3Rh has C^*_{3v} symmetry, all other Nb_3X clusters have C^*_s symmetry. Nb_3Pd and Nb_3Ag each have two short Nb-X bonds and one long, Nb_3X (X= Sr, Mo, Tc, Ru) have two long Nb-X bonds and one short.

The calculated adiabatic IPs for Nb_3X are presented in Table 6.1 along with the calculated transitions for the lowest energy transition permitted by the $\Delta S = \pm 1/2$ selection rule. The IPs predicted using B3P86 are typically 0.3 - 0.5 eV higher than experimental values [123], indeed the predicted IP for Nb_3Nb (i.e. Nb_4) is 5.96 eV, which is higher than the value of 5.64 eV measured by Knickelbein [116]. Therefore all values have had a linear offset of -0.32 eV applied in order to bring the predicted IPs in line with the experimental Nb_4 value. Of the

12 heteroatoms, only Al and Cd are found to increase the IP (by 0.41 and 0.28 eV respectively) of the cluster relative to Nb_4 and both of these clusters undergo significant geometry changes upon ionization. Neutral Nb_3Al has a doubly bridged structure of C_s^* symmetry which becomes triply bound (C_s^*, two short bonds, one long) upon ionisation, Nb_3Cd is planar with C_{2v}^* symmetry, but the cation has a Nb′-Nb-Nb-Cd dihedral of 154°.

Adiabatic EAs for Nb_3X are also presented in Table 6.1. The EA of Nb_4 was measured by Chen *et* al.[221] to be 1.15 eV, which corresponds closely to the predicted EA of 1.12 eV, therefore the predicted EA values have no offset applied. As with the cationic species, anions were chosen to access the neutral of interest. In the case of Nb_3Tc, the doublet and quartet anions were found to be nearly degenerate, however the quartet anion is unable to access the singlet neutral species. As the neutral Nb_3Tc singlet and triplet are also found to be close in energy, it is possible that the anionic quartet could access the triplet neutral and then the doublet cation, this is shown as an additional row in Table 6.1. Of all the species investigated, Nb_4 has the lowest EA, while Nb_3Al has the highest (1.99 eV).

The atomic Mulliken charges of the neutral Nb_3X clusters were extracted as a measure of the electron distribution and are presented in Table 6.2. Relative to Nb_4 where all atoms have zero charge, sodium, aluminium, scandium, yttrium and zirconium atoms possess δ-positive charges. Sodium, scandium and yttrium donate to all three niobium atoms approximately equally (supporting the assignment of C_{3v}^* symmetry). Aluminium donates to all three niobium atoms (unequally) and zirconium donates electron density to one niobium atom, leaving the remaining two atoms with a small δ-positive charge of 0.07. Sodium and aluminium atoms both donate almost half an electron to the Nb_3 moiety. All other heteroatoms withdraw electron density from the Nb_3 moiety, resulting in δ-negative charges ranging from -0.06 (Nb_3Cd) to -0.91 (Nb_3Rh).

6.3.2 CO and C, O bound clusters

The, lowest energy associatively and dissociatively bound Nb_3X-CO structures, determined at the lowest two multiplicities possible for each cluster, are shown in Figures 6.2 and 6.3 respectively. Associative and dissociative binding energies and CO stretching frequencies for the associatively bound structures are presented in Table 6.3. In all cases, the dissociatively bound structure was lower in energy than the associative structure. The associative and dissociative binding cases will be discussed in turn.

To begin comparison, we find the lowest energy associatively bound Nb_4CO structure has a μ^2 bound CO and possesses C_s^* symmetry. The CO is bound by 2.65 eV and has a stretching frequency (ν_{CO}) of 1443 cm^{-1} has reduced from the free value of 2046 cm^{-1} which is consistent with μ^2 binding.

Nb_3X clusters, where X is to the left of, and including, Mo, (i.e. X = Na, Sc, Sr, Y, Zr and Mo) all bind CO to one of the Nb_2X faces. Of these, Nb_3SrCO, Nb_3ZrCO and Nb_3MoCO all bind CO to an NbX edge in a μ^2 fashion whereas Nb_3ScCO and Nb_3YCO bind in a η^2 fashion i.e. parallel to the Nb_2X face, resulting in a significantly lowered ν_{CO} (913 and 905 cm^{-1} respectively). Nb_3NaCO also has a comparatively low ν_{CO} of 1108 cm^{-1} and binds similarly to Nb_3ScCO and Nb_3YCO, however the sodium atom is sufficiently distant from the Nb_3 plane to temper its effect on the CO moiety. CO binding energies reflect these geometries with Nb_3NaCO, Nb_3ScCO, Nb_3YCO and Nb_3ZrCO all binding CO by over 3 eV. Nb_3SrCO binds CO by 2.84 eV. Only Nb_3MoCO binds CO less than Nb_4CO with a binding energy of 2.44 eV. Overall, these binding energies range from 2.4 to 3.6 eV, the same range as previously calculated by us for CO binding to $4d$ transition metal trimers.[205]

The remainder of the Nb_3X clusters (X = Al, Tc, Ru, Rh, Pd, Ag, Cd), i.e. the heteroatoms to the right of Mo, all bind CO to an edge of the Nb_3 face in a μ^2 arrangement, with the exception of Nb_3PdCO which is μ^1 bound. CO binding energies for these clusters are all similar to (within 0.12 eV) the binding energy of Nb_4CO (cf. 2.65 eV) indicating that these heteroatoms, which are not directly bound to the CO moiety, have very little effect on the CO binding energy.

Dissociatively bound Nb_3X-C-O clusters also show a strong left to right dependence of the binding motif. Heterotatoms to the left of, and including, Mo (X = Na, Al, Sc, Sr, Y, Zr and Mo) use at least one of the Nb_2X faces to bind the C and O atoms. Nb_3Na-C-O binds both atoms in a μ^2 fashion to Nb-Nb bonds however, unlike later structures the Na-Nb-Nb-C and Na-Nb-Nb-O dihedral angles are acute (65° and 48° respectively) indicating that the carbon and oxygen atoms sit above the Nb_2Na face, rather than the Nb_3 face. Nb_3Al-C-O, Nb_3Sc-C-O, Nb_3Sr-C-O and Nb_3Y-C-O all have the carbon atom μ^3 bound to a Nb_2X face and the oxygen atom μ^2 bound to one of the adjacent Nb-X bonds. Nb_3Zr-C-O and Nb_3Mo-C-O bind both atoms in a μ^2 arrangement but differ in that Nb_3Zr-C-O has the oxygen atom bound to a Nb-Zr bond and the carbon atom to a Nb-Nb bond whereas Nb_3Mo-C-O binds the carbon atom to one of the Nb-Mo bonds and the oxygen atom to a Nb-Nb bond.

The second group of Nb_3X clusters, to the right of Mo (i.e. X = Tc, Ru, Rh, Pd, Ag, Cd) bind C, O in the same manner as Nb_4-C-O, that is both atoms μ^2 bound to a Nb-Nb bond. The only exception in this group is Nb_3Ag-C-O, where the carbon atom is μ^3 bound to the Nb_3 face.

The strength of Nb-O and Nb-C bonds (7.53 and 5.39 eV respectively) compared to the bond strength of CO ($\approx$11 eV) suggests that CO dissociation on niobium clusters is likely to be exothermic. This was found to be the case for all Nb_3X clusters investigated here. The final column in Table 6.3 shows the difference in binding energy between the associative and dissociative structures, $\Delta E_{\text{Dissoc.}-\text{Assoc.}}$. As seen, the values are mostly consistent between 2.1-2.7

eV with only two exceptions, discussed below. This means that whatever the (associative) binding energy of the CO complex, dissociation of the molecule is even more favourable by a relatively constant amount, regardless of Nb_3X.

The larger value of $\Delta E_{\text{Dissoc.}-\text{Assoc.}}$ seen for Sr (3.21 eV), indicates a relatively higher preference for dissociation for this species. Conversely, Nb_3Cd had a reduced value of only 1.67 eV, indicating a reduced preference for dissociation. Only one other species, Nb_3Al, had a reduced value compared to Nb_4 and this was only reduced by 0.01 eV. Only these two clusters exhibit the property consistent with our initial goal of using a heteroatom to reduce the dissociative character of niobium clusters. The Mulliken charge data for these two clusters are quite different and does not yield any insight into this result. It could be expected that the large δ-positive charge of the Al atom results from significant electron donation into the Nb_3 moiety which allows less interaction with CO. This is also supported by the relatively low binding energy for the associatively bound complex. However, the Mulliken charge for the Cd atom is barely changed. What these two clusters share is a calculated IP greater than that for Nb_4, which is unique to these two species. Conversely, the Nb_3X cluster with the lowest IP, Nb_3Sr, has the largest $\Delta E_{\text{Dissoc.}-\text{Assoc.}}$. It is known from the study of transition metal cluster + hydrogen kinetic data [18], that IP is an approximate guide to the reaction rates (although for some clusters, better correlation is found by combining IP with EA to give an estimate of the HOMO-LUMO promotion energy). This suggests that for this series of clusters, the IP is the dominant factor mediating exothermicity of CO dissociation. Therefore, clusters with high IP are less likely to dissociate CO and *v*ice-versa. This is completely consistent with the emerging picture described in the introduction where CO is now known to dissociate on clusters, such as Nb_n, with a relatively low IP but does not dissociate on clusters such as Rh_n that have high IPs (Rh_3 has an IP between 6.42 and 7.87 eV) [56].

Therefore, on the basis of this work, it would not seem possible to increase the IP of a Nb_3X cluster to a high enough value to stop dissociation occurring. It may be that the addition of more than one heteroatom might achieve our original aim of preventing the dissociation of CO, i.e. Nb_3X_2 or Nb_3X_3. However in doing this, more than the IP of the cluster is changed. As mentioned in the introduction, recent experimental work shows that physically blocking M_3 faces can be used to prevent CO dissociation on early transition metals.[217] Thus, a synergistic effect could be obtained whereby additional X atoms block the Nb-Nb edges over which dissociation occurs as well as increasing the IP. We are currently exploring this effect with a range of different atoms as X.

6.4 Conclusion

This study investigated whether the reactivity of niobium clusters could be altered by incorporation of a single heteroatom. It was found that the niobium atoms were always involved in binding CO and that the heteroatom could donate as much as half an electron or withdraw as much as almost a full electron from Nb_3 without significantly affecting the reactivity of the cluster with CO. Both Nb_3Al and Nb_3Cd have raised IPs relative to Nb_4 and both of these clusters have lower $\Delta E_{\text{Dissoc.}-\text{Assoc.}}$ than Nb_4 though the strength of this effect is mild and the dissociation of CO on these two clusters is still exothermic by 2.10 and 1.67 eV, respectively. In all other cases, the addition of a heteroatom increased the enthalpy of CO dissociation. This work suggests that it would be worthwhile to explore the behaviour of clusters with a higher proportion of heteroatoms.

Cluster	calculated transition	Adiabatic EA (eV)	Adiabatic IP (eV)
Nb$_3$Na	$S=\frac{3}{2}\rightarrow S=1\rightarrow S=\frac{1}{2}$	1.21	5.01
Nb$_3$Al	$S=\frac{3}{2}\rightarrow S=1\rightarrow S=\frac{1}{2}$	1.99	6.05
Nb$_3$Sc	$S=\frac{3}{2}\rightarrow S=1\rightarrow S=\frac{1}{2}$	1.63	5.23
Nb$_3$Sr	$S=1\rightarrow S=\frac{3}{2}\rightarrow S=1$	1.60	4.79
Nb$_3$Y	$S=\frac{3}{2}\rightarrow S=1\rightarrow S=\frac{1}{2}$	1.71	5.31
Nb$_3$Zr	$S=0\rightarrow S=\frac{1}{2}\rightarrow S=1$	1.56	5.35
Nb$_3$Nb	$S=\frac{1}{2}\rightarrow S=0\rightarrow S=\frac{1}{2}$	1.12	5.64
Nb$_3$Mo	$S=1\rightarrow S=\frac{1}{2}\rightarrow S=1$	1.54	5.06
Nb$_3$Tc	$S=\frac{1}{2}\rightarrow S=0\rightarrow S=\frac{1}{2}$	1.58	5.24
Nb$_3$Tc	$S=\frac{3}{2}\rightarrow S=1\rightarrow S=\frac{1}{2}$	1.72	5.23
Nb$_3$Ru	$S=1\rightarrow S=\frac{1}{2}\rightarrow S=1$	1.51	5.38
Nb$_3$Rh	$S=\frac{3}{2}\rightarrow S=1\rightarrow S=\frac{1}{2}$	1.44	5.53
Nb$_3$Pd	$S=1\rightarrow S=\frac{1}{2}\rightarrow S=1$	1.48	5.45
Nb$_3$Ag	$S=\frac{3}{2}\rightarrow S=1\rightarrow S=\frac{1}{2}$	1.72	5.54
Nb$_3$Cd	$S=1\rightarrow S=\frac{1}{2}\rightarrow S=1$	1.70	5.92

Table 6.1: B3P86/sdd predicted adiabatic IPs and EAs of Nb$_3$X clusters. A linear offset of -0.32 eV has been applied to all IPs. Calculated transitions are indicated in the second column.

Cluster	δNb(1)	δNb(2)	δNb(3)	δX
Nb$_3$Na	-0.16	-0.17	-0.17	0.49
Nb$_3$Al	-0.12	-0.16	-0.16	0.44
Nb$_3$Sc	-0.00	0.00	0.00	0.01
Nb$_3$Sr	0.12	0.04	0.04	-0.19
Nb$_3$Y	0.02	0.02	0.02	0.05
Nb$_3$Zr	-0.25	0.07	0.07	0.11
Nb$_3$Nb	0.00	0.00	0.00	0.00
Nb$_3$Mo	0.03	0.09	0.09	-0.20
Nb$_3$Tc	0.00	0.20	0.20	-0.40
Nb$_3$Ru	0.02	0.24	0.24	-0.50
Nb$_3$Rh	0.31	0.30	0.30	-0.91
Nb$_3$Pd	0.26	0.23	0.23	-0.72
Nb$_3$Ag	0.11	0.14	0.14	-0.39
Nb$_3$Cd	0.00	0.03	0.03	-0.06

Table 6.2: Mulliken populations of Nb$_3$X clusters. Nb(2) and Nb(3) are equal by symmetry.

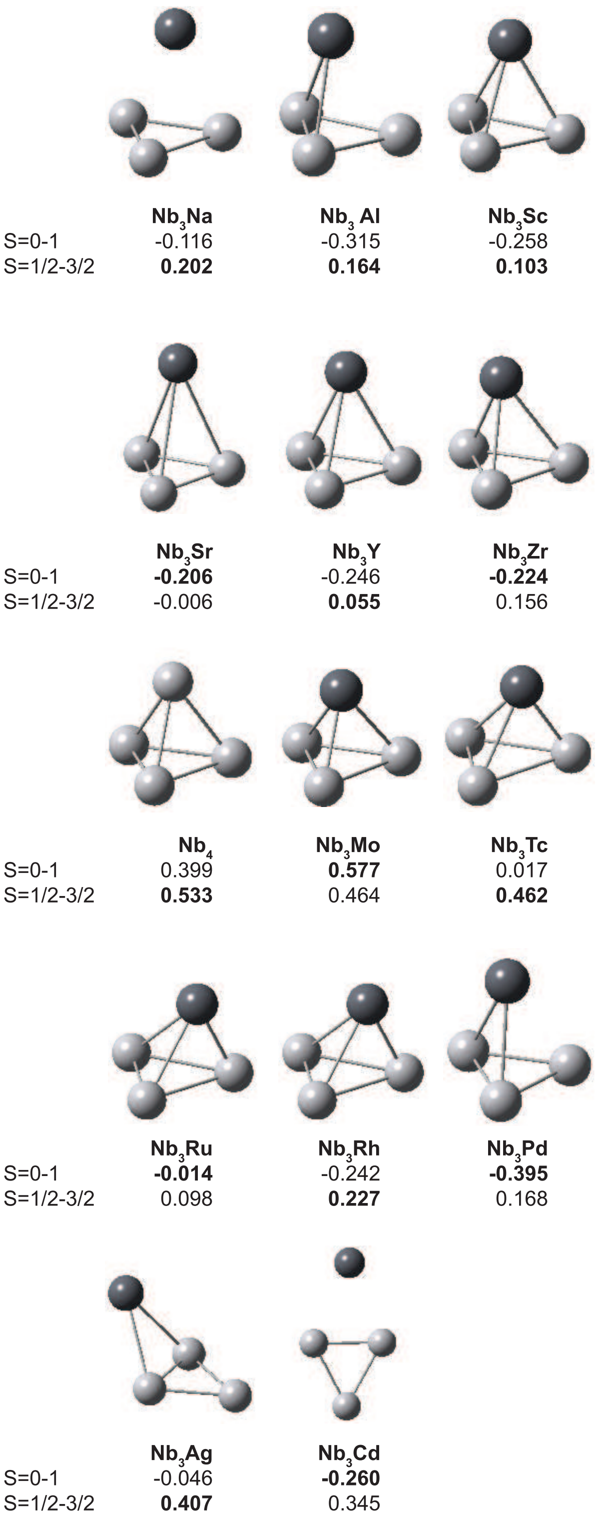

	S=0-1	S=1/2-3/2
Nb_3Na	-0.116	**0.202**
Nb_3 Al	-0.315	**0.164**
Nb_3Sc	-0.258	**0.103**
Nb_3Sr	**-0.206**	-0.006
Nb_3Y	-0.246	**0.055**
Nb_3Zr	**-0.224**	0.156
Nb_4	0.399	**0.533**
Nb_3Mo	**0.577**	0.464
Nb_3Tc	0.017	**0.462**
Nb_3Ru	**-0.014**	0.098
Nb_3Rh	-0.242	**0.227**
Nb_3Pd	**-0.395**	0.168
Nb_3Ag	-0.046	**0.407**
Nb_3Cd	**-0.260**	0.345

Figure 6.1: Structures and relative energies (eV) of the lowest two spin states of neutral and cationic Nb_3X clusters. The heteroatom is shown in black. Cationic ΔEs are indicated in bold.

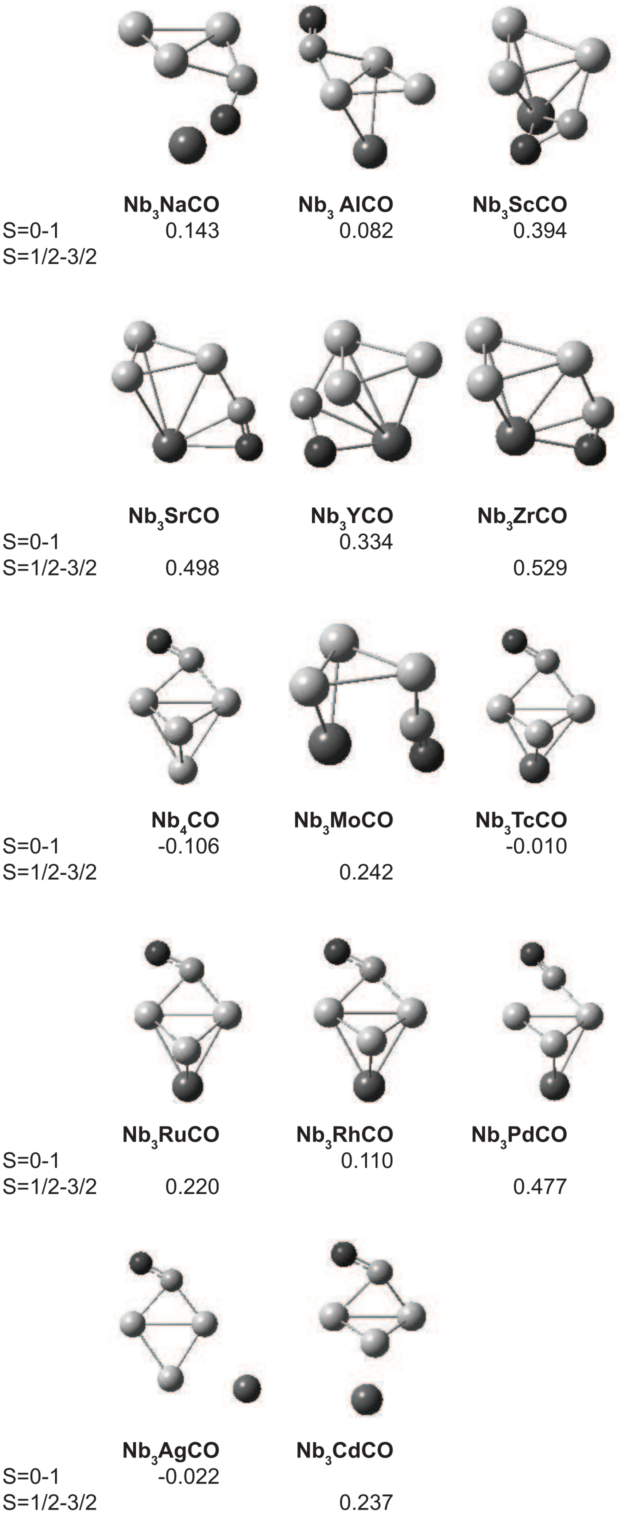

Figure 6.2: Structures and relative energies (eV) of the lowest two spin states of associatively bound neutral Nb_3X-CO clusters. The heteroatom is shown in black.

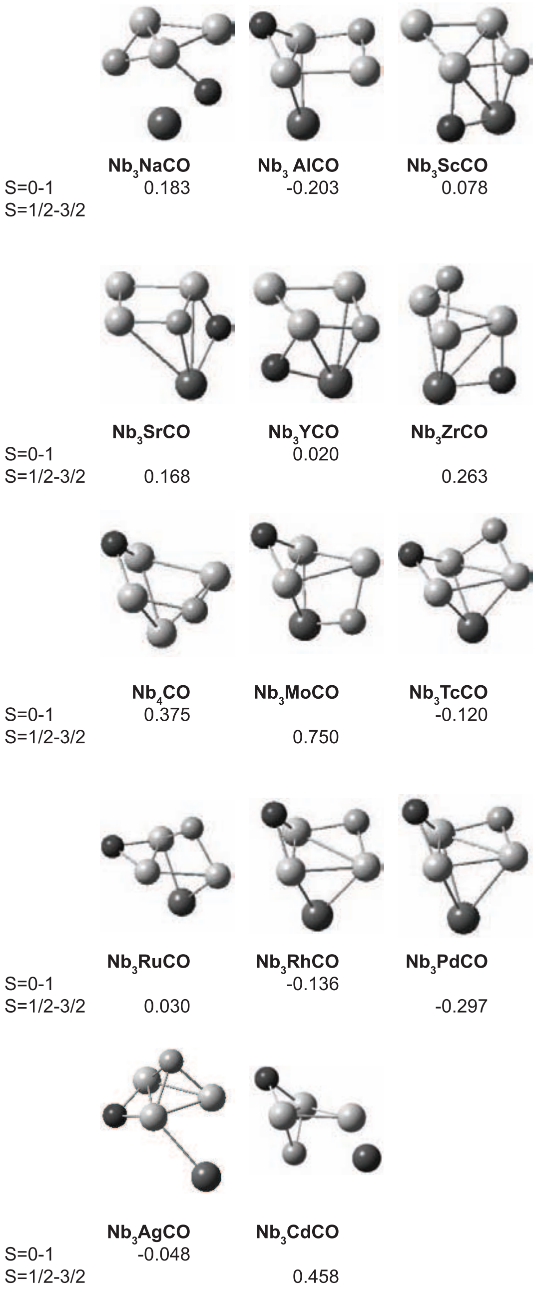

Figure 6.3: Structures and relative energies (eV) of the lowest two spin states of dissociatively bound neutral Nb_3X-C-O clusters.The heteroatom is shown in black.

Cluster	Nb_3X-CO Binding Energy (eV)	$\nu_{(\text{CO})}$ (cm^{-1})	Nb_3X-C-O Binding Energy (eV)	$\Delta E_{\text{Dissoc.}-\text{Assoc.}}$ (eV)
Nb_3Na	3.02	1108	5.25	2.23
Nb_3Al	2.59	1447	4.69	2.10
Nb_3Sc	3.62	913	6.39	2.78
Nb_3Sr	2.84	1417	6.04	3.21
Nb_3Y	3.46	905	6.23	2.77
Nb_3Zr	3.09	1294	5.71	2.62
Nb_3Nb	2.65	1443	4.76	2.11
Nb_3Mo	2.44	1544	4.70	2.26
Nb_3Tc	2.79	1357	5.11	2.32
Nb_3Ru	2.77	1387	5.18	2.41
Nb_3Rh	2.61	1391	4.87	2.26
Nb_3Pd	2.66	1628	4.83	2.17
Nb_3Ag	2.70	1386	4.95	2.24
Nb_3Cd	2.74	1272	4.40	1.67

Table 6.3: Associative and Dissociative binding energies of CO (eV) to Nb_3X clusters. BEs are determined from the lowest energy Nb_3X cluster to the lowest energy Nb_3XCO cluster regardless of multiplicity. $\nu_{(CO)}$ of the associative species is shown in the third column and the difference between associative and dissociative binding energies is shown in the final column.

Conclusions

Introduction

Transition metal clusters typically possess large numbers of low-lying electronic states, which arise from the partially filled d-shells of each metal atom. This high density of states hampers spectroscopic and computational elucidation alike. It is fortunate therefore that the weaknesses of experimental and computational approaches are often complementary. As such it is increasingly common for spectroscopists and computational chemists to work together, with calculations being used both to probe and predict experimental observations. The work in this thesis performs both roles. This brief summary will highlight the relationship between experiment and computation for each chapter of this work and suggest possible future directions for both experimental and computational investigations.

Summary

Chapter 1 began with the observation that CO was seen to dissociate on small niobium clusters, but not on small rhodium clusters. A metal trimer was selected as the smallest possible model of a cluster and a series of M_3CO stoichiometries were investigated, spanning the 4d transition metals from niobium to silver. Nb_3, Mo_3 and Tc_3 were found to thermodynamically dissociate CO and all trimers to the right of Tc (viz. Ru_3, Rh_3 Pd_3 and Ag_3) were found to bind CO associatively. For those trimers that dissociated CO, intrinsic reaction coordinate calculations were used to uncover probable reaction pathways to dissociation.

$Nb_3{}^-$ is one of a small number of systems, larger than dimers, to have its photoelectron spectrum recorded. Chapter 2 began by using DFT, CASSCF and MRCI calculations to assign the photoelectron spectrum of Nb_3^-. The first three states could be assigned to doublet neutral species, however the fourth peak seen in the spectrum is likely to belong to a quartet. ZEKE spectra have been recorded for both Nb_3N_2 and Nb_3C_2, so using the same methodololgy as applied to Nb_3, these species were investigated. In both cases the lowest lying (cationic) excited states were found well above the region that had been scanned in the ZEKE spectra, suggesting that revisiting these spectra and scanning to higher energies could uncover these states.

While the MRCI calculations were able to accurately determine relative energies of states of one charge and spin, DFT calculations proved to be far more reliable at predicting the distance between the neutral and cationic manifolds - i.e. the IP of the cluster. However, even the most reliable density functionals still required an empricially determined scaling factor in order to achieve absolute agreement with experimental IPs. Thus Chapter 3 was devoted to optimising a functional that could predict the adiabatic IPs of transition metal clusters. The final functional form was a hybridised Becke-Wigner functional and was named Becke-Fock-Wigner, or BFW. When tested on a set of metal clusters whose IPs and geometries had been previously determined, BFW performed better than both B3LYP and B3PW91 and it retained acceptable performance when tested on the G2 data set.

In Chapter 4, a stochastic algorithm, "Kick" for structure determination was implemented and tested for several small metal clusters. Two series of pentamers were investigated: Pd_nAu_m and Nb_mRh_n, $(m + n = 5)$. It was found that the geometric structure of Pd_nAu_m clusters underwent a substantial shift from 3-dimensional to planar as the gold composition increased, whereas Nb_mRh_n clusters adopted predominantly trigonal bipyramidal geometries regardless of composition. Kick was also able to identify geometric isomers with relative energies as small as 0.003 eV. Where different geometric isomers in a given stoichiometry lie close in energy, they may co-exist in a molecular beam experiment and this has been observed in several niobium clusters. Therefore it is desired to investigate the properties (including reactivity) of low-lying isomers independently. Thus an extension to the Kick algorithm, whereby previously determined (by Kick or otherwise) molecular fragments could be supplied to Kick. This new capability was tested on Zeise's anion, where the known x-ray crystal structure was determined to be the global minimum and the use of an ethylene fragment allowed the minimum to be located within 10 jobs, rather than requiring several thousand jobs. The extension was found to have far more general uses, beyond metal clusters and several applications of this modified algorithm are discussed in Chapter 5.

The final chapter in this thesis, came full circle and applied the modified Kick algorithm to determining the thermodynamic minima and properties of a series of singly substituted niobium clusters; Nb_3X with CO. All clusters considered thermodynamically dissociated CO. Experiments on these systems could confirm the calculated IPs and EAs of the bare metal clusters and confirm the dissociative binding of CO.

Conclusion

The task of mapping the chemical reactivity (and other properties) of small transition metal clusters is indeed monumental in size. The high density of states present in these clusters means that the structure of any given cluster, M_n, may be radically different from the structure of M_{n+1} or $M_{n-1}X$, subsequently no general rules for predicting cluster properties currently exist. Also due to the high density of states, these systems are intrinsically challenging to study from both spectroscopic and computational approaches. Further mapping of these systems may point towards some general rules as well as uncover clusters possessing unique reactivity that can be harnessed for use in ultra-efficient catalytic systems.

Appendix A

Nb_3X_2 orbitals

APPENDIX A depicts the symmetry adapted linear combination (SALC) of orbitals that describe Nb_3C_2 and Nb_3N_2 in C_{2v} symmetry. Carbon atoms are used for convenience, however, the same orbitals apply for Nb_3N_2.

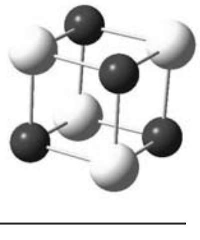

	E	$C_2(z)$	$\sigma_v(xz)$	$\sigma_v(yz)$	linear, rotations	quadratic
A_1	1	1	1	1	z	x^2, y^2, z^2
A_2	1	1	-1	-1	R_z	xy
B_1	1	-1	1	-1	x, R_y	xz
B_2	1	-1	-1	1	y, R_x	yz

Table A.1: Character table for the C_{2v} point group.

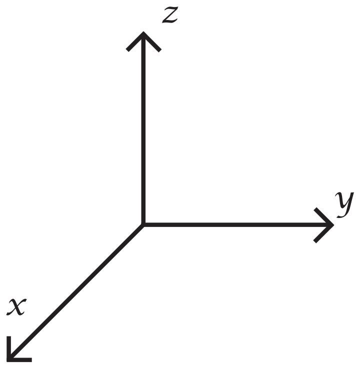

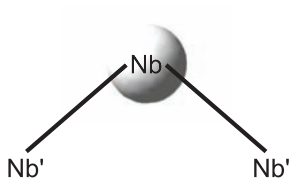

4s
5s

1 1 1 1 a_1

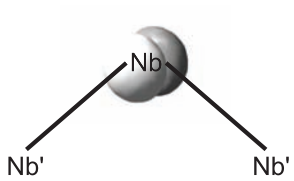

$4p_x$

1 -1 1 -1 b_1

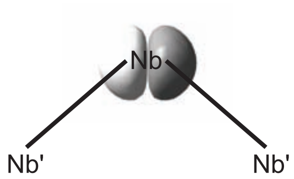

$4p_y$

1 -1 -1 1 b_2

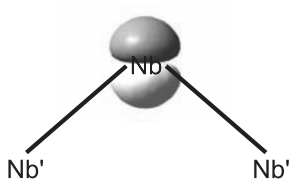

$4p_z$

1 1 1 1 a_1

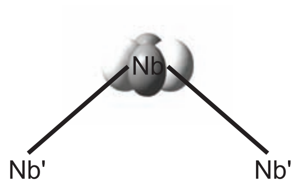

$4d_{x^2-y^2}$

1 1 1 1 a_1

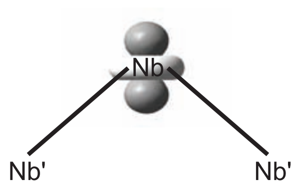

$4d_{z^2}$

1 1 1 1 a_1

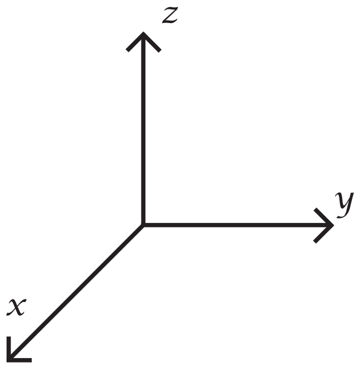

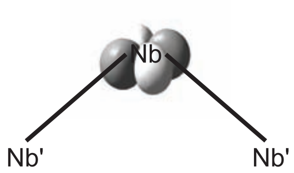

4d$_{xy}$

1	1	-1	-1	a_2

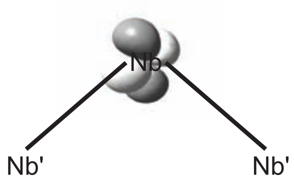

4d$_{xz}$

1	-1	1	-1	b_1

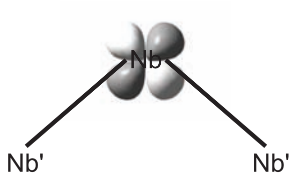

4d$_{yz}$

1	-1	-1	1	b_2

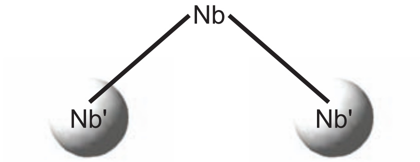

4s + 4s
5s + 5s

1	1	1	1	a_1

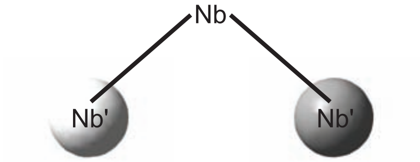

4s - 4s
5s - 5s

1	-1	-1	1	b_2

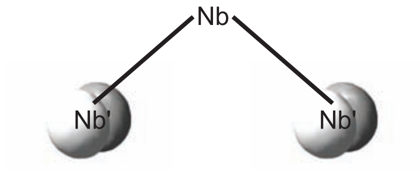

4p$_x$ + 4p$_x$

1	-1	1	-1	b_1

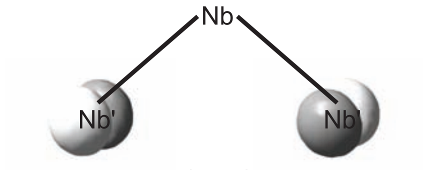

$4p_x$ - $4p_x$

1 1 -1 -1 a_2

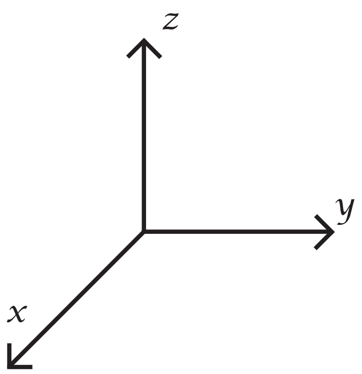

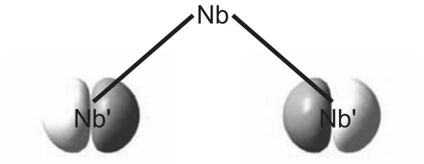

$4p_y$ + $4p_y$

1 1 1 1 a_1

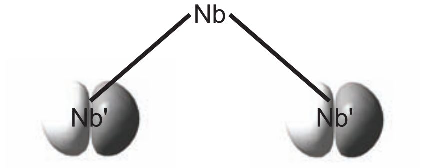

$4p_y$ - $4p_y$

1 -1 -1 1 b_2

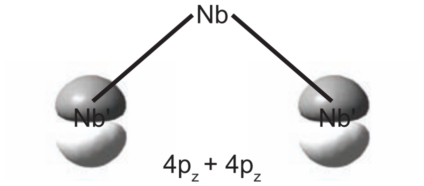

$4p_z$ + $4p_z$

1 1 1 1 a_1

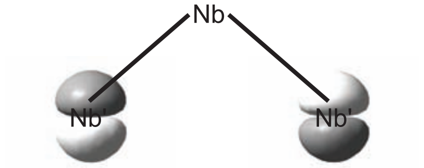

$4p_z$ - $4p_z$

1 -1 -1 1 b_2

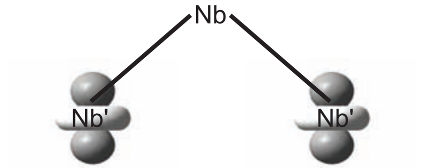

$4d_{z^2}$ + $4d_{z^2}$

1 1 1 1 a_1

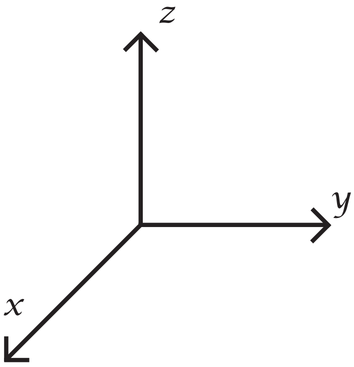

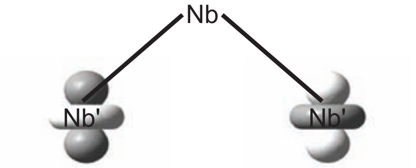

$4d_{z^2} - 4d_{z^2}$

1 -1 -1 1 b_2

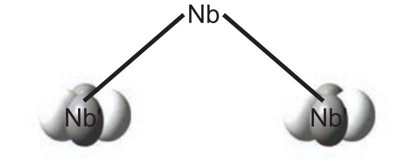

$4d_{x^2-y^2} + 4d_{x^2-y^2y}$

1 1 1 1 a_1

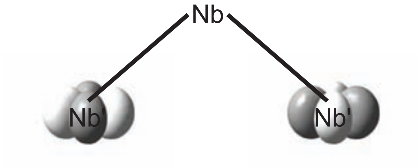

$4d_{x^2-y^2} - 4d_{x^2-y^2}$

1 -1 -1 1 b_2

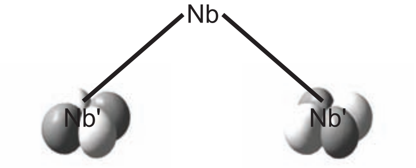

$4d_{xy} + 4d_{xy}$

1 -1 1 -1 b_1

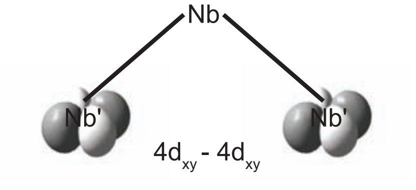

$4d_{xy} - 4d_{xy}$

1 1 -1 -1 a_2

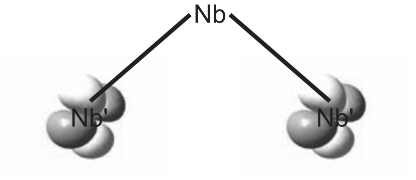

$4d_{xz} + 4d_{xz}$

1 -1 1 -1 b_1

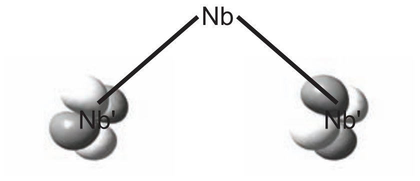

$4d_{xz} - 4d_{xz}$

1 1 -1 -1 a_2

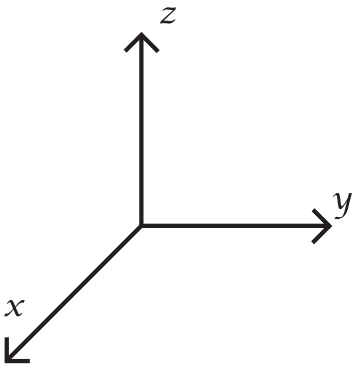

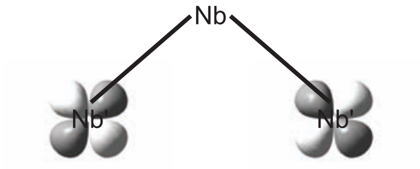

$4d_{yz} + 4d_{yz}$

1 1 1 1 a_1

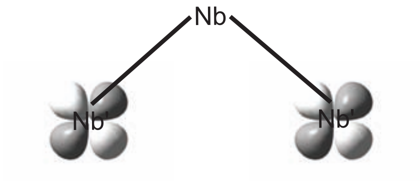

$4d_{yz} - 4d_{yz}$

1 -1 -1 1 b_2

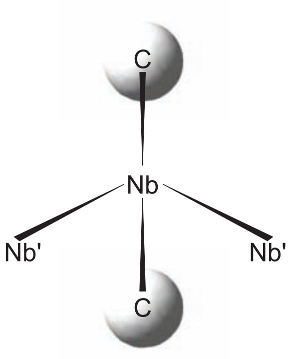

1s + 1s
2s + 2s

1 1 1 1 a_1

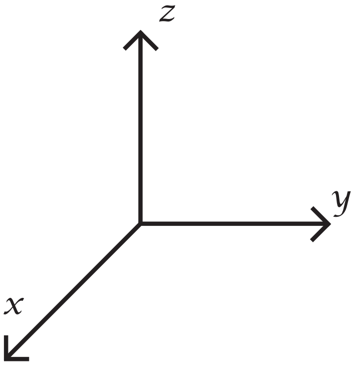

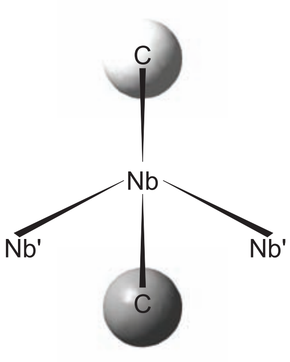

1s - 1s
2s - 2s

1 -1 -1 1 b_2

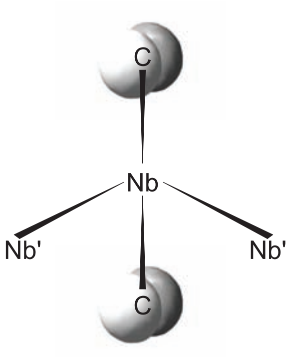

$2p_x + 2p_x$

1 1 1 1 a_1

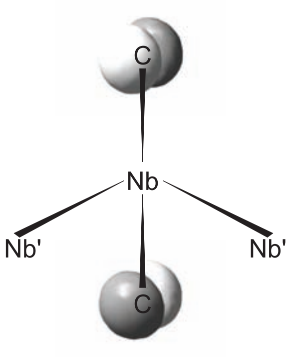

$2p_x - 2p_x$

1 -1 -1 1 b_2

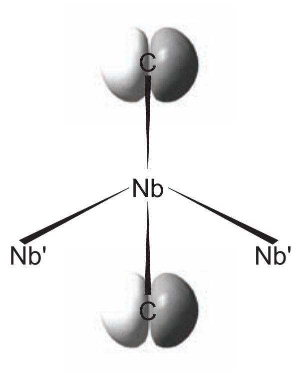

$2p_y + 2p_y$

1 -1 1 -1 b_1

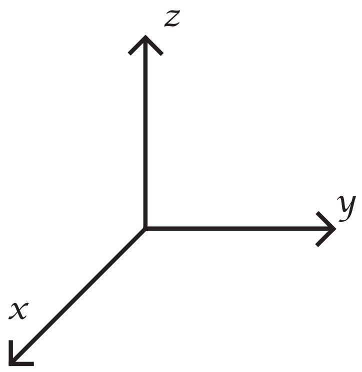

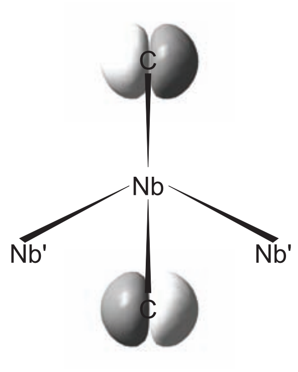

$2p_y - 2p_y$

1 1 -1 -1 a_2

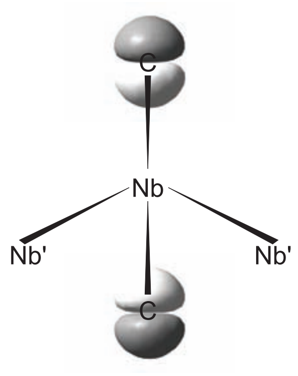

$2p_z + 2p_z$

1 1 1 1 a_1

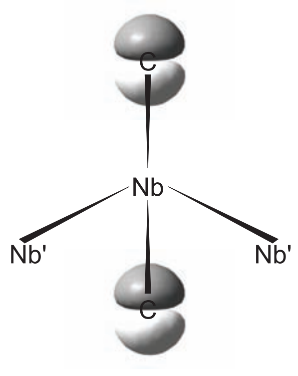

$2p_z - 2p_z$

1 -1 -1 1 b_2

The SALC orbitals for Nb_3 are: $12a_1$, $4a_2$, $5b_1$ and $9b_2$. These orbitals plus those for the pair of carbon (or nitrogen) atoms yield a symmetry adapted linear combination of: $16a_1$, $5a_2$, $6b_1$, $13b_2$ orbitals for Nb_3C_2 and Nb_3N_2.

Appendix B

Kick Source Code

APPENDIX B provides the perl source code for the three main Kick scripts. Kick-start sets up and runs the jobs. Kick-parse parses the results and provides summary output. Kick-freq resubmits frequency analysis / higher level of theory jobs for unique geometries.

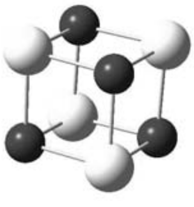

B.1 Kick-start

```
#!/usr/bin/perl -s
##
### Author: Matt Addicoat
##

# Script to set up random co-ordinate gaussian jobs

use Math::Matrix ;

$Input="Kick.in";
$Header="Header_opt.in";
$Pseudo="Pseudo_opt.in";
$Submit="Submit_opt.in";
$Restart="Restart.data";



# Read in Kick run parameters

open(KICK,"$Input") or die "Unable to open initial input file: $Input";

@lines = <KICK>;
$Num_of_geometries = $lines[1];
$Submit_guff = $lines[4];
@Submit_parameters = split(/,/, $Submit_guff);
$ncpus = @Submit_parameters[0];
$mem = @Submit_parameters[1];
$Time =@Submit_parameters[2];

chop $Time;
$Box = $lines[7];
@Box_dimensions = split(/,/, $Box);
$Box_x = @Box_dimensions[0];
$Box_y = @Box_dimensions[1];
$Box_z = @Box_dimensions[2];

$atoms = $lines[11];
chop $atoms;
@Atoms = split(/,/, $atoms);
$Num_of_atoms = @Atoms;

$fragments = $lines[13];
chop $fragments;
@Fragments = split(/,/, $fragments);
$Num_of_fragments = @Fragments;



$Charge = $lines[16];
chop $Charge; #remove newline character
$Multiplicity = $lines[19];
chop $Multiplicity; #remove newline character



for ($iteration = 0; $iteration < $Num_of_geometries; $iteration++)
{
if (-e $Restart) #Test to see if this is a restart run
```

```
{
open (RESTART,"$Restart");
$AlreadyDone = <RESTART>;
$number= sprintf '%04d',($iteration+$AlreadyDone+1);
}
else
{
$number= sprintf '%04d', $iteration;
}
$filebase="Kick$number";
$G03Input = "$filebase.com";
open (COMFILE, ">$G03Input");
read_dump_headers($Header);
print COMFILE "\n";
print COMFILE "$Charge $Multiplicity\n";

#Dealing with fragments

foreach $frag_id (@Fragments)
{
open(FRAG,"$frag_id.cart") or die "Unable to open fragment file: $frag_id.cart";
open(ROT_FRAG,">$frag_id.rot");

#get a set of angles
@base_angles = gen_ptp();
$phi = $base_angles[0];
$theta = $base_angles[1];
$psi = $base_angles[2];

#do the trig
$cos_phi = sprintf '%.6f', cos($phi);
$cos_theta = sprintf '%.6f', cos($theta);
$cos_psi = sprintf '%.6f', cos($psi);
$sin_phi = sprintf '%.6f', sin($phi);
$sin_theta = sprintf '%.6f', sin($theta);
$sin_psi = sprintf '%.6f', sin($psi);

#make the rotation matrix
$D = new Math::Matrix ([$cos_phi,$sin_phi,0],[-$sin_phi,$cos_phi,0],[0,0,1]);
$C = new Math::Matrix ([1,0,0],[0,$cos_theta,$sin_theta],[0,-$sin_theta,$cos_theta]);
$B = new Math::Matrix ([$cos_psi,$sin_psi,0],[-$sin_psi,$cos_psi,0],[0,0,1]);
$A = $B->multiply($C)->multiply($D);

@FragLines = <FRAG>;
while ($Fline = shift (@FragLines))
{
@Cartesians = split '\s+', $Fline;
($Atom_label, @orig_xyz) = @Cartesians;
print ROT_FRAG "$Atom_label\t";
$matrix_xyz = new Math::Matrix ([$orig_xyz[0],$orig_xyz[1],$orig_xyz[2]]);
$trans_xyz = ($matrix_xyz->transpose);
$rotated_xyz = $A->multiply($trans_xyz);
@new_xyz = split '\n+',$rotated_xyz;
print ROT_FRAG "$new_xyz[0]\t$new_xyz[1]\t$new_xyz[2]\n";
}
close ROT_FRAG;
}
```

```
#Now translate the rotated coords

foreach $frag_id (@Fragments)
{
#`cp $frag_id.rot $frag_id.rot.$iteration`;
open(FRAG,"$frag_id.rot") or die "Unable to open fragment file: $frag_id.cart";
@FragLines = <FRAG>;
@base_xyz = gen_xyz();
$base_x = $base_xyz[0];
$base_y = $base_xyz[1];
$base_z = $base_xyz[2];
while ($Fline = shift (@FragLines))
{
@Cartesians = split '\s+', $Fline;
$new_x = $base_x + $Cartesians[1];
$new_y = $base_y + $Cartesians[2];
$new_z = $base_z + $Cartesians[3];
print COMFILE "$Cartesians[0]\t$new_x\t$new_y\t$new_z\n";
}
}

foreach $species (@Atoms)
{
@xyz = gen_xyz();
print COMFILE "$species\t$xyz[0]\t$xyz[1]\t$xyz[2]\n";
}

print COMFILE "\n";
if (-e $Pseudo) #Test to see if a pseudo file exista
{
read_dump_pseudo($Pseudo);
}
submit_files($filebase);
}



#dump a file for restart
open (RESTART,">$Restart");
print RESTART "$number";
close RESTART;

# Generation of random co-ordinates

sub gen_xyz
{
$x = rand($Box_x);
$y = rand($Box_y);
$z = rand($Box_z);
$x_coord = sprintf '%.6f', $x;
$y_coord = sprintf '%.6f', $y;
$z_coord = sprintf '%.6f', $z;
@coords =($x_coord, $y_coord, $z_coord);
return @coords;
#print "$x_coord\t $y_coord\t $z_coord";
}

sub gen_ptp # phi, theta, psi
{
```

```
$pi = 3.14159265;
$phi = sprintf '%.6f', rand()*2*$pi;
$theta = sprintf '%.6f', rand()*2*$pi;
$psi = sprintf '%.6f', rand()*2*$pi;
@angles =($phi, $theta, $psi);
return @angles;
}

# Read / Dump headers

sub read_dump_headers
{
$Headerfile = $_[0];
open(HEADER,"$Headerfile") or die "Unable to open $Header";
@HeaderLines = <HEADER>;
while ($HLine = shift (@HeaderLines))
{
if ($HLine =~ /chk/) #find the checkpoint file line
{
chop $HLine; #remove newline char
print COMFILE "$HLine$filebase.chk\n";
}
else
{
print COMFILE "$HLine";
}
}
print COMFILE "\nKick job $iteration\n";
close HEADER;
}

sub read_dump_pseudo
{
$Pseudofile = $_[0];
open(PSEUDO,"$Pseudofile") or die "Unable to open $Pseudo";
@PseudoLines = <PSEUDO>;
while ($HLine = shift (@PseudoLines))
{
print COMFILE "$HLine";
}
close PSEUDO;
}
#submit stuff to queue

sub submit_files
{
$FileBase = $_[0];
$SubmitFile = "$FileBase.submit";
open(SUBFILE,">$SubmitFile");
#read the Submit_opt.in file
open(SUBMIT,"$Submit") or die "Unable to open $Submit";
@SubmitLines = <SUBMIT>;

while ($SLine = shift (@SubmitLines))
{
if ($SLine =~ /walltime=/) #Time should be taken from Kick.in
{
print SUBFILE "$`walltime=$Time:00:00\n"; #print whatever's on the line before walltime
```

```
}
elsif ($SLine =~ /PBS -N/) #Job name
{
print SUBFILE "#PBS -N $FileBase\n";
}
else
{
print SUBFILE "$SLine";
}

}
        if ($FileBase =~ /7$/) #every 10th job
        {
                print SUBFILE "./Kick-start.pl\n";
        }

print SUBFILE "g03 <$FileBase.com >& $FileBase.log \n";

close SUBFILE;
close SUBMIT;


`qsub $FileBase.submit`;

}
```

B.2 Kick-parse

```
#!/usr/bin/perl -s
###
#### Author: Matt Addicoat
###
#
## Script to parse and summarise output from a Kick run
#

use File::ReadBackwards ;

$OutputDir="./";
$Unordered_Energies_File ="Unordered_Energies.out";
$Ordered_Energies_File="Ordered_Energies.out";
$Unique_Energies_File="Unique_Energies.out";
$Summary_File="Summary.out";
$Geometries_File="Geometries.out";

@All_jobs= `ls *log --format=single-column`;
$Number_of_jobs=@All_jobs;

# Get a list (array) of successful jobs

@Grep_Normal = `grep Normal $OutputDir/*log`;
foreach $Job_id (@Grep_Normal)
{
```

```
$_ = $Job_id;
#s/(\/)(\S)(\:)/\2/;
s/(\s*$OutputDir\/)(Kick\d+\.log)(\:.*)/\2/;
#s/Log/Fog/;
#print "$_";
push(@Successful_Jobs, $_);
}
$Number_successful_jobs = @Successful_Jobs;

#Create a file with the energies of all successful jobs

open(UNORDERED,">$Unordered_Energies_File");

# Get the final energy
foreach $Job (@Successful_Jobs)
{
chop $Job;
@Grep_SCF = ‘grep "SCF Done" $OutputDir/$Job ‘;
$LastLine = pop(@Grep_SCF);
@LastLine_Bits = split ’\s+’,$LastLine;
$Energy = $LastLine_Bits[5];
#print "$Energy";
print UNORDERED "$Energy\t$Job\n";
$Energy =sprintf ’%.5f’, $Energy;
push(@List_of_Energies,$Energy);
}
close UNORDERED;

@Energies{@Successful_Jobs} = @List_of_Energies;



#sort by values
open(ORDERED_E,">$Ordered_Energies_File");

foreach (sort {$Energies{$a} cmp $Energies{$b} } keys %Energies)
{
print ORDERED_E "$Energies{$_}\t$_\n";
push(@Ordered_List_of_Filenames,$_);
push(@Ordered_List_of_Energies,$Energies{$_});
}
close ORDERED_E;

# remove duplicates

open(ORDERED_E,"$Ordered_Energies_File");
while(<ORDERED_E>){
($E,$Filename) = split ’\t’;
chop $Filename;
$Unique_E{$E} = $Filename;
}

$Number_Unique_Energies=scalar(keys %Unique_E);
$Lowest_E = (sort keys %Unique_E)[-1];

open(UNIQUE_E,">$Unique_Energies_File");
open(GEOM,">$Geometries_File");
foreach (sort keys %Unique_E)
{
```

```
print UNIQUE_E "$_ \t$Unique_E{$_}\n";
print GEOM "$_ \t$Unique_E{$_}\n";
$file_to_read="$OutputDir/$Unique_E{$_}";
@SO = grab_standard_orientation($file_to_read);
foreach $Line (@SO)
{
@stuff = split '\s+', $Line;
$AtomicNumber = $stuff[2];
$x_coord = $stuff[4];
$y_coord = $stuff[5];
$z_coord = $stuff[6];
print GEOM "$AtomicNumber\t$x_coord\t$y_coord\t$z_coord\n";
}



print GEOM "\n";

}

close UNIQUE_E;
close GEOM;
# Dump Energies and geometries to a file





# Create a summary

$Percent_success = sprintf '%.2f',(($Number_successful_jobs/$Number_of_jobs)*100);
$Percent_unique = sprintf '%.2f',(($Number_Unique_Energies/$Number_of_jobs)*100);

open(SUMMARY,">$Summary_File");
($sec,$min,$hour,$mday,$mon,$year,$wday,
$yday,$isdst)=localtime(time);

printf SUMMARY "%4d-%02d-%02d %02d:%02d:%02d\n\n",
$year+1900,$mon+1,$mday,$hour,$min,$sec;

print SUMMARY "In this Kick run, there were $Number_of_jobs  jobs run.\n";
print SUMMARY "Of which $Number_successful_jobs ($Percent_success\%) terminated normally.\n";
print SUMMARY "$Number_Unique_Energies ($Percent_unique\%) of these jobs gave unique energies (5 dp).\n\n";
print SUMMARY "The Unique Energies were:\n";

foreach (sort keys %Unique_E)
{
$Delta_E = sprintf '%.3f',(($_-$Lowest_E)*27.2116); #in eV
print SUMMARY "$_\t $Delta_E\t$Unique_E{$_}\n";
}

close SUMMARY;





sub grab_standard_orientation
{

$logfile=$_[0];
```

```
undef $bw;
@Standard_Orientation =();

$bw = File::ReadBackwards->new( $logfile ) or die "can’t read $logfile" ;
while( defined( $log_line = $bw->readline ) )
{

push(@lines,$log_line);
}

while ($line = shift (@lines))
{
last if ($line =~ /\sRotational/)
}



while ($line = shift (@lines))
{

last if ($line =~ /\sNumber/);
if ($line !~ /\s----------/)
{
push(@Standard_Orientation,$line);
}
}
while($line = shift (@lines))
{
#do nothing until eof
}

return @Standard_Orientation;
}
```

B.3 Kick-freq

```
#!/usr/bin/perl -s
###
#### Author: Matt Addicoat
###
#
## Script to run frequencies on all discrete geometries from a kick run
#
$Input="Kick.in";
$Header="Header_freq.in";
$Submit="Submit_freq.in";
```

```
$Pseudo="Pseudo_freq.in";
$Geometries_File="Geometries.out";

# This is all we need for the frequencies run
open(KICK,"$Input") or die "Unable to open initial input file: $Input";
@lines = <KICK>;
$Num_of_geometries = $lines[1];
$Submit_guff = $lines[4];
@Submit_parameters = split(/,/, $Submit_guff);
$ncpus = @Submit_parameters[0];
$mem = @Submit_parameters[1];
$Time =@Submit_parameters[2];
chop $Time;
$Charge = $lines[16];
chop $Charge;   #remove newline character
$Multiplicity = $lines[19];
chop $Multiplicity;     #remove newline character
close KICK;



open(GEOM,"$Geometries_File") or die "Unable to open file containing the geometries from Kick-parse: $Geometries_File";
@GeomLines = <GEOM>;
while($GeomLine = shift (@GeomLines))
{
if ($GeomLine =~ /^-/)#an energy will start with a - sign
{
($E,$Filename) = split ’\s+’,$GeomLine; # first line
$FileBase = $Filename;
$FileBase =~ s/(\w+)(\.)(log)/\1/;
open(COMFILE,">$FileBase-freq.com");
read_dump_headers($Header);
print COMFILE "\n";
print COMFILE "$Charge $Multiplicity\n";

}
elsif ($GeomLine !~ /^$/)
{
print COMFILE "$GeomLine";
}
else #should be a blank line
{
print COMFILE "\n";
if  (-e $Pseudo) #Test to see if a pseudo file exists
{
read_dump_pseudo($Pseudo);
}
close COMFILE;
submit_files("$FileBase-freq");
}



}



# Read / Dump headers

sub read_dump_headers
{
```

```
$Headerfile = $_[0];
open(HEADER,"$Headerfile") or die "Unable to open $Header";
@HeaderLines = <HEADER>;
while ($HLine = shift (@HeaderLines))
{
if ($HLine =~ /chk/) #find the checkpoint file line
{
chop $HLine; #remove newline char
print COMFILE "$HLine$FileBase.chk\n";
}
else
{
print COMFILE "$HLine";
}
}
print COMFILE "\n$FileBase Frequency\n";
close HEADER;
}


#read / dump pseudo

sub read_dump_pseudo
{
$Pseudofile = $_[0];
open(PSEUDO,"$Pseudofile") or die "Unable to open $Pseudo";
@PseudoLines = <PSEUDO>;
while ($HLine = shift (@PseudoLines))
{
print COMFILE "$HLine";
}
close PSEUDO;
}
#submit stuff to queue

sub submit_files
{
$FileBase = $_[0];
$SubmitFile = "$FileBase.submit";
open(SUBFILE,">$SubmitFile");
#read the Submit_freq.in file
open(SUBMIT,"$Submit") or die "Unable to open $Submit";
@SubmitLines = <SUBMIT>;

while ($SLine = shift (@SubmitLines))
{
if ($SLine =~ /walltime=/) #Time should be taken from Kick.in
{
print SUBFILE "$`walltime=$Time:00:00\n"; #print whatever's on the line before walltime
}
elsif ($SLine =~ /PBS -N/) #Job name
{
print SUBFILE "#PBS -N $FileBase\n";
}
else
{
print SUBFILE "$SLine";
}
```

```
}
print SUBFILE "g03 <$FileBase.com >& $FileBase.log \n";
close SUBFILE;
close SUBMIT;


‘qsub $FileBase.submit‘;

}
```

Appendix C

Supplementary Information

APPENDIX C is included on CD. For Chapters 1 and 6 cartesian coordinates and absolute energies of all structures mentioned in the text is provided. In the case of Chapters 4 and 5, the output from Kick-parse is given for each stoichiometry, which also provides cartesian coordinates and absolute energies.

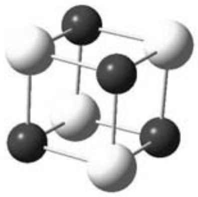

References

[1] Jortner, J. *Physics and Chemistry of Finite Systems: From Clusters to Crystals* **1995**, *1*, 1–17.

[2] Mwakapumba, J.; Ervin, K. M. *Mass Spect. Ion Proc.* **1997**, *161*, 161–174.

[3] Blyholder, G. *J. Phys. Chem.* **1964**, *68*, 2772–2778.

[4] Purcell, K. F. *Inorganic Chemistry;* W. B. Saunders Company, 1977.

[5] Gröenbeck, H.; Rosen, A.; Andreoni, W. *Z. Phys. D* **1997**, *40*, 206–209.

[6] Toyoshima, I.; Somorjai, G. A. *Catal. Rev. Sci. Eng.* **1979**, *19*, 101–159.

[7] Berces, A.; Hackett, P. A.; Lian, L.; Mitchell, S. A.; Rayner, D. M. *J. Chem. Phys.* **1998**, *108*, 5476–5490.

[8] Whetten, R. L.; Zakin, M. R.; Cox, D. M.; Trevor, D. J.; Kaldor, A. *J. Chem. Phys.* **1986**, *85*, 1697–1698.

[9] Brucat, P. J.; Pettiette, C. L.; Yang, S.; Zheng, L.-S.; Craycraft, M. J.; Smalley, R. E. *J. Chem. Phys.* **1968**, *85*, 4747–4748.

[10] Zakin, M. R.; Brickman, R. O.; Cox, D. M.; Kaldor, A. *J. Chem. Phys.* **1988**, *88*, 3555–3560.

[11] Hamrick, Y.; Taylor, S.; Lemire, G. W.; Fu, Z. W.; Shui, J. C.; Morse, M. D. *J. Chem. Phys.* **1988**, *88*(6), 4095–4098.

[12] Elkind, J. L.; Wiess, F. D.; Alford, J. M.; Laaksonen, R. T.; Smalley, R. E. *J. Chem. Phys.* **1988**, *88*, 5215–5224.

[13] Shi, Y.; Ervin, K. M. *J. Chem. Phys.* **1998**, *108*, 1757–1760.

[14] Heiz, U.; Sanchez, A.; Abbet, S.; Schneider, W.-D. *Eur. Phys. J. D.* **1999**, *9*, 35–39.

[15] Worz, A. S.; Judal, K.; Abbet, S.; Heiz, U. *J. Am. Chem. Soc.* **2003**, *125*, 7964–7970.

[16] Heiz, U.; Sanchez, A.; Abbet, S.; Schneider, W.-D. *J. Am. Chem. Soc.* **1999**, *121*, 3214–3217.

[17] Heiz, U.; Sanchez, A.; Abbet, S.; Schneider, W.-D. *Chemical Physics* **2000**, *262*, 189–200.

[18] Knickelbein, M. B. *Annu. Rev. Phys. Chem.* **1999**, *50*, 79–115.

[19] Fowler, J. E.; Garcia, A.; Ugalde, J. M. *Phys. Rev. A* **1999**, *60*, 3058–3070.

[20] Das, K. K.; Balasubramanian, K. *J. Chem. Phys.* **1990**, *93*(1), 625–632.

[21] Yang, D.; Zgierski, M. Z.; Bérces, A.; Hackett, P. A.; Martinez, A.; Salahub, D. R.; Roy, P.-N.; Jr., T. C.; Fournier, R.; Pang, T.; Chen, C. *J. Chem. Phys.* **1996**, *105*, 10663–10672.

[22] Yang, D. S.; Zgierski, M. Z.; Rayner, D. M.; Hackett, P. A.; Martinez, A.; Salahub, D. R.; Roy, P.-N.; Jr., T. C. *J. Chem. Phys.* **1995**, *103*, 5335–5342.

[23] Yang, D.-S.; Zgierski, M. Z.; Bérces, A.; Hackett, P. A.; Martinez, A.; Salahub, D. R. *Chem. Phys. Lett.* **1997**, *227*, 71–78.

[24] Yang, D.-S.; Hackett, P. A. *J. Elec. Spect. and Rel. Phen.* **2000**, *106*, 153–169.

[25] Addicoat, M.; Metha, G.; Buntine, M.; Pedersen, D. B.; Simard, B.; Rayner, D. M.; Fielicke, A. *J. Phys. Chem. A* **2004**, *108*, 964–970.

[26] Fielicke, A.; von Helden, G.; Meijer, G.; Pedersen, D. B.; Simard, B.; Rayner, D. M. *J. Phys. Chem. B* **2004**, *108*, 14591–14598.

[27] Schoone, K.; Smets, J.; Ramaekers, R.; Houben, L.; Adamowicx, L.; Maes, G. *Journal of Molecular Structure* **2003**, *649*, 61–68.

[28] Duncan, M. A. *Int. Rev. Phys. Chem.* **2003**, *22*(2), 407–435.

[29] Thomas, L. H. *Proc. Cam. Phil. Soc.* **1927**, *23*, 542–548.

[30] Fermi, E. *Rend. Accad. Lincei.* **1927**, *6*, 602–607.

[31] Fermi, E. *Z. Phys.* **1928**, *48*, 73–79.

[32] Fermi, E. *Rend. Accad., Lincei* **1928**, *7*, 342–346.

[33] Hohenberg, P.; Kohn, W. *Phys. Rev.* **1964**, *136*, 864–871.

[34] Kohn, W.; Sham, L. J. *Phys. Rev.* **1965**, *140*, 1133–1138.

[35] Kohn, W.; Sham, L. J. *Phys. Rev.* **1965**, *137*, 1697–1705.

[36] Koch, W.; Holthausen, M. C. *A Chemist's Guide to Density Functional Theory;* Wiley-VCH, 2 ed., 2001.

[37] Kohn, W. *Rev. Mod. Phys.* **1999**, *71*, 1253–1266.

[38] Becke, A. D. *J. Chem. Phys.* **1992**, *96*, 2155–2160.

[39] Becke, A. D. *J. Chem. Phys.* **1992**, *97*, 9173–9177.

[40] Becke, A. D. *J. Chem. Phys.* **1993**, *98*, 5648–5652.

[41] Lieb, E. H. *Rev. Mod. Phys.* **1981**, *53*, 603–641.

[42] Delley, B. *J. Chem. Phys.* **1990**, *92*, 508–517.

[43] Schuchardt, K.; Didier, B.; Elsethagen, T.; Sun, L.; Gurumoorthi, V.; Chase, J.; Li, J.; Windus, T. *J. Chem. Inf. Model.* **2007**, *47*, 1045–1052.

[44] Hay, P. J.; Wadt, W. R. *J. Chem. Phys.* **1985**, *82*, 270–283.

[45] Hay, P. J.; Wadt, W. R. *J. Chem. Phys.* **1985**, *82*, 284–298.

[46] Hay, P. J.; Wadt, W. R. *J. Chem. Phys.* **1985**, *82*, 299–298.

[47] Dolg, M.; Wedig, U.; Stoll, H.; Preuss, H. *J. Chem. Phys.* **1987**, *86*, 866–872.

[48] Andrae, D.; Huermann, U.; M. Dolg, H. S.; Preu, H. *Theor. Chim. Acta.* **1990**, *77*, 123–141.

[49] Andrae, D.; Haubermann, U.; Dolg, M.; Stoll, H.; Preub, H. *Theoretica Chimica Acta* **1990**, *77*, 123–141.

[50] Becke, A. D. *J. Chem. Phys.* **1996**, *104*, 1040–1046.

[51] Perdew, J. P. *Phys. Rev. B* **1986**, *33*, 8822–8824.

[52] Weinberg, W. H. *Langmuir* **1993**, *9*(3), 655–662.

[53] Somorjai, G. A. *Introduction to Surface Science and Catalysis;* Wiley: New York, 1994.

[54] Hintz, P. A.; Ervin, K. M. *J. Chem. Phys.* **1994**, *100*(8), 5715–5725.

[55] Ren, X. L.; Hintz, P. A.; Ervin, K. M. *J. Chem. Phys.* **1993**, *99*(5), 3575–3587.

[56] Cox, D. M.; Reichmann, K. C.; Trevor, D. J.; Kaldor, A. *J. Chem. Phys.* **1988**, *88*(1), 111–119.

[57] Kapiloff, E.; Ervin, K. M. *J. Phys. Chem. A* **1997**, *101*(45), 8460–8469.

[58] Morse, M. D.; Geusic, M. E.; Heath, J. R.; Smalley, R. E. *J. Chem. Phys.* **1985**, *83*(5), 2293–2304.

[59] Lee, T. H.; Ervin, K. M. *J. Phys. Chem.* **1994**, *98*(40), 10023–10031.

[60] Mwakapumba, J.; Ervin, K. N. *Int. J. Mass Spec. Ion Proc.* **1997**, *161*(1-3), 161–174.

[61] Wallace, W. T.; Whetten, R. L. *J. Phys. Chem. B* **2000**, *104*(47), 10964–10968.

[62] Fielicke, A.; von Helden, G.; Meijer, G.; Pedersen, D. B.; Simard, B.; Rayner, D. M. *J. Chem. Phys.* **2006**, *124*(19), 194305.

[63] Fielicke, A.; von Helden, G.; Meijer, G.; Simard, B.; Denommee, S.; Rayner, D. M. *J. Am. Chem. Soc.* **2003**, *125*(37), 11184–11185.

[64] Fielicke, A.; von Helden, G.; Meijer, G.; Pedersen, D. B.; Simard, B.; Rayner, D. M. *J. Am. Chem. Soc.* **2005**, *127*(23), 8416–8423.

[65] BrodEn, G.; Rhodin, T. N.; Brucker, C.; Benbow, R.; Hurych, Z. *Surf. Sci.* **1976**, *59*(2), 593–611.

[66] Leskiw, B. D.; Castleman, A. W. *Compt. Rend. Phys.* **2002**, *3*(3), 251–272.

[67] Loock, H. P.; Simard, B.; Wallin, S.; Linton, C. *J. Chem. Phys.* **1998**, *109*(20), 8980–8992.

[68] Simard, B.; Presunka, P. I.; Loock, H. P.; Berces, A.; Launila, O. *J. Chem. Phys.* **1997**, *107*(2), 307–318.

[69] Brucat, P. J.; Pettiette, C. L.; Yang, S.; Zheng, L. S.; Craycraft, M. J.; Smalley, R. E. *J. Chem. Phys.* **1986**, *85*(8), 4747–4748.

[70] Sievers, M. R.; Armentrout, P. B. *Int. J. Mass Spec.* **1998**, *180*, 103–115.

[71] Chen, M. H.; Wang, X. F.; Zhang, L. N.; Qin, Q. Z. *J. Phys. Chem. A* **2000**, *104*(30), 7010–7015.

[72] Pedersen, D. B.; Rayner, D. M.; Simard, B.; Addicoat, M. A.; Buntine, M. A.; Metha, G. F.; Fielicke, A. *J. Phys. Chem. A* **2004**, *108*(6), 964–970.

[73] Majumdar, D.; Balasubramanian, K. *J. Chem. Phys.* **1997**, *106*(17), 7215–7222.

[74] Tan, H.; Liao, M. Z.; Dai, D. G.; Balasubramanian, K. *J. Phys. Chem. A* **1999**, *103*(18), 3495–3504.

[75] Goursot, A.; Papai, I.; Salahub, D. R. *Stud. Surf. Sci. Cat.* **1993**, *75*, 1547–1550.

[76] Mineva, T.; Russo, N.; Freund, H. J. *J. Phys. Chem. A* **2001**, *105*(47), 10723–10730.

[77] Koukounas, C.; Kardahakis, S.; Mavridis, A. *J. Chem. Phys.* **2005**, *123*(7), 074327.

[78] Gaussian 03, Revision D.01. Frisch, M. J.; Trucks, G. W.; Schlegel, H. B.; Scuseria, G. E.; Robb, M. A.; Cheeseman, J. R.; Montgomery, Jr., J. A.; Vreven, T.; Kudin, K. N.; Burant, J. C.; Millam, J. M.; Iyengar, S. S.; Tomasi, J.; Barone, V.; Mennucci, B.; Cossi, M.; Scalmani, G.; Rega, N.; Petersson, G. A.; Nakatsuji, H.; Hada, M.; Ehara, M.; Toyota, K.; Fukuda, R.; Hasegawa, J.; Ishida, M.; Nakajima, T.; Honda, Y.; Kitao, O.; Nakai, H.; Klene, M.; Li, X.; Knox, J. E.; Hratchian, H. P.; Cross, J. B.; Bakken, V.; Adamo, C.; Jaramillo, J.; Gomperts, R.; Stratmann, R. E.; Yazyev, O.; Austin, A. J.; Cammi, R.; Pomelli, C.; Ochterski, J. W.; Ayala, P. Y.; Morokuma, K.; Voth, G. A.; Salvador, P.; Dannenberg, J. J.; Zakrzewski, V. G.; Dapprich, S.; Daniels, A. D.; Strain, M. C.; Farkas, O.; Malick, D. K.; Rabuck, A. D.; Raghavachari, K.; Foresman, J. B.; Ortiz, J. V.; Cui, Q.; Baboul, A. G.; Clifford, S.; Cioslowski, J.; Stefanov, B. B.; Liu, G.; Liashenko, A.; Piskorz, P.; Komaromi, I.; Martin, R. L.; Fox, D. J.; Keith, T.; Al-Laham, M. A.; Peng, C. Y.; Nanayakkara, A.; Challacombe, M.; Gill, P. M. W.; Johnson, B.; Chen, W.; Wong, M. W.; Gonzalez, C.; Pople, J. A.

[79] Huber, K. P.; Herzberg, G. *Constants of Diatomic Molecules;* Van Nostrand Reinhold: New York, 1979.

[80] Harvey, J. N.; Aschi, M.; Schwarz, H.; Koch, W. *Theor. Chem. Acc.* **1998**, *99*(2), 95–99.

[81] Goodwin, L.; Salahub, D. R. *Phys. Rev. A* **1993**, *47*(2), R774–R777.

[82] Gronbeck, H.; Rosen, A.; Andreoni, W. *Z. Phys. D.* **1997**, *40*(1-4), 206–209.

[83] Fowler, J. E.; Garcia, A.; Ugalde, J. M. *Phys. Rev. A* **1999**, *60*(4), 3058–3070.

[84] Wang, H. M.; Craig, R.; Haouari, H.; Liu, Y. F.; Lombardi, J. R.; Lindsay, D. M. *J. Chem. Phys.* **1996**, *105*(13), 5355–5357.

[85] Diez, R. P. *Int. J. Quant. Chem.* **2000**, *76*(1), 105–112.

[86] Fang, L.; Davis, B.; Lu, H. Y.; Chen, X. Y.; Shen, X. L.; Lombardi, J. R. *Chem. Phys. Lett.* **2002**, *352*(1-2), 70–74.

[87] Guo, R.; Balasubramanian, K. *J. Chem. Phys.* **2003**, *118*(1), 142–148.

[88] Fang, L.; Shen, X. L.; Chen, X. Y.; Lombardi, J. R. *Chem. Phys. Lett.* **2000**, *332*(3-4), 299–302.

[89] Dai, D.; Balasubramanian, K. *Chem. Phys. Lett.* **1992**, *195*(2-3), 207–213.

[90] Van Zee, R. J.; Hamrick, Y. M.; Li, S.; Weltner, W. *Chem. Phys. Lett.* **1992**, *195*(2-3), 214–220.

[91] Goursot, A.; Papai, I.; Salahub, D. R. *J. Am. Chem. Soc.* **1992**, *114*(19), 7452–7458.

[92] Fielicke, A.; von Helden, G.; Meijer, G.; Pedersen, D. B.; Simard, B.; Rayner, D. M. *J. Phys. Chem. B* **2004**, *108*(38), 14591–14598.

[93] Ervin, K. M.; Ho, J.; Lineberger, W. C. *J. Chem. Phys.* **1988**, *89*(8), 4514–4521.

[94] Balasubramanian, K. *J. Chem. Phys.* **1989**, *91*(1), 307–313.

[95] Zacarias, A. G.; Castro, M.; Tour, J. M.; Seminario, J. M. *J. Phys. Chem. A* **1999**, *103*(38), 7692–7700.

[96] Seminario, J. M.; Zacarias, A. G.; Castro, M. *Int. J. Quant. Chem.* **1997**, *61*(3), 515–523.

[97] Zhou, J.; Li, Z. H.; Wang, W. N.; Fan, K. N. *J. Phys. Chem. A* **2006**, *110*(22), 7167–7172.

[98] Cheng, P. Y.; Duncan, M. A. *Chem. Phys. Lett.* **1988**, *152*(4-5), 341–346.

[99] Wallimann, F.; Frey, H. M.; Leutwyler, S.; Riley, M. *Z. Phys. D* **1997**, *40*(1-4), 30–35.

[100] Srinivas, S.; Salian, U. A.; Jellinek, J. In *Metal-Ligand Interactions in Chemistry, Physics and Biology*; Salahub, N. R., D.., Eds.; Kluwer: Dordrecht, 2000; pages 295–324.

[101] Rayner, D. M.; Lian, L.; Fournier, R.; Mitchell, S. A.; Hackett, P. A. *Phys. Rev. Lett.* **1995**, *74*(11), 2070–2073.

[102] Lide, D. *CRC Handbook of Chemistry and Physics;* Chemical Rubber Company: Florida, 84 ed., 2003.

[103] Pedley, J. B.; Marshall, E. M. *J. Phys. Chem. Ref. Dat.* **1983**, *12*(4), 967–1031.

[104] Brugh, D. J.; Ronningen, T. J.; Morse, M. D. *J. Chem. Phys.* **1998**, *109*(18), 7851–7862.

[105] Langenberg, J. D.; DaBell, R. S.; Shao, L.; Dreessen, D.; Morse, M. D. *J. Chem. Phys.* **1998**, *109*(18), 7863–7875.

[106] Blyholder, G. *J. Phys. Chem.* **1964**, *68*(10), 2772–2777.

[107] Majumdar, D.; Balasubramanian, K. *J. Chem. Phys.* **2003**, *119*, 12866–12877.

[108] Majumdar, D.; Balasubramanian, K. *J. Chem. Phys* **2004**, *121*, 4014–4032.

[109] Majumdar, D.; Balasubramanian, K. *J. Chem. Phys.* **2001**, *115*.

[110] Guo, R.; Balasubramanian, K. *J. Chem. Phys.* **2003**, *118*, 142–148.

[111] Balasubramanian, K.; Liao, M. Z. *Chem. Phys.* **1988**, *127*, 313–324.

[112] Knowles, P. J.; Werner, H.-J. *J. Chem. Phys.* **1985**, *82*, 5053–5063.

[113] Knowles, P. J.; Werner, H.-J. *Chem. Phys. Lett.* **1985**, *115*, 259–267.

[114] LaJohn, L. A.; Christiansen, P. A.; Ross, R. B.; Atashroo, T.; Ermler, W. C. *J. Chem. Phys.* **1987**, *87*(5), 2812–2824.

[115] Kietzmann, H.; Morenzin, J.; Bechthold, P. S.; Ganteför, G.; Eberhardt, W.; Yang, D.-S.; Hackett, P. A.; Fournier, R.; Pang, T.; Chen, C. *Phys. Rev. Lett.* **1996**, *77*, 4528–4531.

[116] Knickelbein, M.; Yang, S. *J. Chem. Phys.* **1990**, *93*, 5760–5767.

[117] Peterson, K.; Figgen, D.; Dolg, M.; Stoll, H. *J. Chem. Phys.* **2007**, *126*, 124101.

[118] Knowles, P. J.; Werner, H.-J. *J. Chem. Phys.* **1988**, *89*, 5803–5814.

[119] Knowles, P. J.; Werner, H.-J. *Chem. Phys. Lett.* **1988**, *145*, 514–522.

[120] Langhoff, S. R.; Davidson, E. R. *Int. J. Quant. Chem.* **1974**, *8*, 61–72.

[121] Denis, P. A.; Balasubramanian, K. *J. Chem. Phys.* **2005**, *123*, 054318.

[122] Jr, T. D. *J. Chem. Phys.* **1989**, *90*, 1007.

[123] Dryza, V.; Addicoat, M. A.; Gascooke, J. R.; Buntine, M. A.; Metha, G. F. *J. Phys. Chem. A* **2008**, *112*, 5582.

[124] Dryza, V.; Addicoat, M. A.; Gascooke, J. R.; Buntine, M. A.; Metha, G. F. *J. Chem. Phys. A* **2005**, *109*, 11180–11190.

[125] Duncan, M. A., Ed. *Spectroscopy and Dynamics;* Jai Press Inc.: Greenwich CT, 1993.

[126] Duncan, M. A., Ed. *Cluster Reactions;* Jai Press Inc.: Greenwich CT, 1994.

[127] Duncan, M. A., Ed. *Spectroscopy and Structure;* Jai Press Inc.: Greenwich CT, 1995.

[128] Duncan, M. A., Ed. *Cluster Materials;* Jai Press Inc.: Greenwich CT, 1998.

[129] Duncan, M. A. *Int. Rev. Phys. Chem.* **2003**, *22*, 407–435.

[130] Simard, B.; Mitchell, S. A.; Rayner, D. M.; Yang, D.-S. In *Metal-Ligand Interactions in Chemistry Physics and Biology*; Russo, N., Salahub, R., Eds.; Kluwer Academic Publishers: Dordrecht, 2000; chapter Structures Energetics and Reactivity of Metal Clusters and Metal-Ligand Species in the Gas Phase, pages 239–294.

[131] Jena, P.; A. W. Castleman, J. *Proc. Natl. Acad. Sci. USA* **2006**, *103*, 10560 – 10569.

[132] Wrz, A. S.; K. Judai, S. A.; Heiz, U. *J. Am. Chem. Soc.* **2003**, *125*, 7964–7970.

[133] Yoon, B.; Hakkinen, H.; Landman, U.; Worz, A. S.; Antonietti, J.-M.; Abbet, S.; Judai, K.; Heiz, U. *Science* **2005**, *307*(5708), 403–407.

[134] Srinivas, S.; Salian, U. A.; Jellinek, J. In *Metal-Ligand Interactions in Chemistry, Physics and Biology*; Russo, N., Salahub, R., Eds.; Kluwer Academic Publishers, 2000; pages 295–324.

[135] Addicoat, M.; Metha, G.; Buntine, M.; Pedersen, D. B.; Simard, B.; Rayner, D. M.; Fielicke, A. *J. Phys. Chem* **2003**, *108*, 964–970.

[136] Majumdar, D.; Balasubramanian, K. *J. Chem. Phys.* **2003**, *119*, 12866–12877.

[137] Stephens, P. J.; Devlin, F. J.; Chabalowski, C. F.; Frisch, M. J. *J. Phys. Chem.* **1994**, *98*, 11623–11627.

[138] Fock, V. *Z. Phys* **1930**, *31*, 126.

[139] Dirac, P. A. M. *Proc. Cambridge Phil. Soc.* **1930**, *26*, 376–385.

[140] Vosko, S. H.; Wilk, L.; Nusair, M. *Can. J. Phys* **1980**, *58*, 1200.

[141] Lee, C.; Yang, W.; Parr, R. G. *Phys. Rev. B* **1988**, *37*, 785–789.

[142] Adamson, R. D.; Gill, P. M. W.; Pople, J. A. *Chem. Phys. Lett.* **1996**, *284*, 6–11.

[143] Lin, C. Y.; George, M. W.; Gill, P. M. W. *Aust. J. Chem.* **2004**, *57*, 365–370.

[144] Curtiss, L. A.; Raghavachari, K.; Trucks, G. W.; Pople, J. A. *J. Chem. Phys.* **1991**, *94*, 7221–7230.

[145] Perdew, J. P.; Chevary, J. A.; Vosko, S. H.; Jackson, K. A.; Pederson, M. R.; Singh, D. J.; Fiolhais, C. *Phys. Rev. B* **1992**, *46*, 6671–6687.

[146] Gill, P. M. W. *Mol. Phys.* **1996**, *89*, 433 – 445.

[147] Perdew, J. P.; Zunger, A. *Phys. Rev. B* **1981**, *23*, 5048–5079.

[148] Wigner, E. *Trans. Faraday. Soc.* **1938**, *34*, 678–685.

[149] Shao, Y.; Molnar, L. F.; Jung, Y.; Kussmann, J.; Ochsenfeld, C.; Brown, S. T.; Gilbert, A. T.; Slipchenko, L. V.; Levchenko, S. V.; Neill, D. P. O.; Jr, R. A. D.; Lochan, R. C.; Wang, T.; Beran, G. J.; Besley, N. A.; Herbert, J. M.; Lin, C. Y.; Voorhis, T. V.; Chien, S. H.; Sodt, A.; Steele, R. P.; Rassolov, V. A.; Maslen, P. E.; Korambath, P. P.; Adamson, R. D.; Austin, B.; Baker, J.; Byrd, E. F. C.; Dachsel, H.; Doerksen, R. J.; Dreuw, A.; Dunietz, B. D.; Dutoi, A. D.; Furlani, T. R.; Gwaltney, S. R.; Heyden, A.; Hirata, S.; Hsu, C.-P.; Kedziora, G.; Khalliulin, R. Z.; Klunzinger, P.; Lee, A. M.; Lee, M. S.; Liang, W.; Lotan, I.; Nair, N.; Peters, B.; Proynov, E. I.; Pieniazek, P. A.; Rhee, Y. M.; Ritchie, J.; Rosta, E.; Sherrill, C. D.; Simmonett, A. C.; Subotnik, J. E.; III, H. L. W.; Zhang, W.; Bell, A. T.; Chakraborty, A. K. *Phys. Chem. Chem. Phys.* **2006**, *8*, 3172 – 3191.

[150] Nelder, J. A.; Mead, R. *Computer Journal* **1964**, *7*, 308–313.

[151] Stewart, P. A.; Gill, P. M. W. *J. Chem. Soc., Faraday Trans.* **1995**, *91*, 4337 – 4341.

[152] Besley, A. G. N.; Gill, P. *J. Phys. Chem. A* **2008**, *112*, 13164–13171.

[153] Wang, H.; Craig, R.; Haouari, H.; Liu, Y.; Lombardi, J. R.; Lindsay, D. M. *J. Chem. Phys.* **1996**, *105*, 5355–5357.

[154] Haouari, H.; Wang, H.; Craig, R.; Lombardi, J. R.; Lindsay, D. M. *J. Chem. Phys.* **1995**, *103*, 9527–9529.

[155] Martin, W. C.; Wiese, W. L. In *Atomic Molecular and Optical Physics Handbook*; Drake, G., Ed.; AIP, Woodbury NY, 1996; pages 135–153.

[156] Bernath, P. F.; McLeod, S. *J. Mol. Spec.* **2001**, *207*, 287–.

[157] Bera, P. P.; Sattelmeyer, K. W.; Saunders, M.; III, H. F. S.; v. R. Schleyer, P. *J. Phys. Chem. A* **2006**, *110*, 4287–4290.

[158] Vlachos, D. G.; Schmidt, L. D.; Aris, R. *Z. Phys. D* **1993**, *26*, S156–158.

[159] Hsu, P. J.; Lai, S. K. *J. Chem. Phys.* **2006**, *124*, 044711.

[160] Harding, D.; Mackenzie, S. R.; Walsh, T. *J. Phys. Chem. B* **2006**, *110*, 18272–18277.

[161] Derepas, A. L.; Soudan, J.; Brenner, V.; Dognon, J.; Millie, P. *J. Comput. Chem.* **2002**, *22*, 1013–1030.

[162] Maeda, S.; Ohno, K. *J. Phys. CHem. A* **2008**, *112*, 2962–2968.

[163] Saunders, M. *J. Comput. Chem.* **2004**, *25*, 4287–4290.

[164] Forda, M. S.; Andersona, M. L.; Barrowa, M. P.; Woodruffb, D. P.; Drewelloa, T.; Derricka, P. J.; Mackenzie, S. R. *Phys. Chem. Chem. Phys.* **2005**, *7*, 975–980.

[165] Cox, A. J.; Louderback, J. G.; Apsel, S. E.; Bloomfield, L. A. *Phys. Rev. B* **1994**, *49*(17), 12295–12298.

[166] Cox, A. J.; Louderback, J. G.; Bloomfield, L. A. *Phys. Rev. Lett.* **1993**, *71*(6), 923–926.

[167] Chien, C.-H.; Blaisten-Barojas, E.; Pederson, M. R. *Phys. Rev. A* **1998**, *58*(3), 2196–2202.

[168] Reddy, B. V.; Nayak, S. K.; Khanna, S. N.; Rao, B. K.; Jena, P. *Phys. Rev. B* **1999**, *59*(7), 5214–5222.

[169] Bae, Y.-C.; Osanai, H.; Kumar, V.; Kawazoe, Y. *Phys. Rev. B* **2004**, *70*(19), 195413.

[170] Wang, L.; Ge, Q. *Chem. Phys. Lett.* **2002**, *366*, 368–376.

[171] Bae, Y.-C.; Osanai, H.; Kumar, V.; Kawazoe, Y. *Phys. Rev. B* **2004**, *70*, 195413.

[172] Hagen, J.; Socaciu, L. D.; Elijazyfer, M.; Heiz, U.; Bernhardt, T. M.; Woste, L. *Phys. Chem. Chem. Phys.* **2002**, *4*, 1707–1709.

[173] Neumaier, M.; Weigend, F.; Hampe, O.; Kappes, M. M. *J. Chem. Phys.* **2006**, *125*, 104308.

[174] Heiz, U.; Sanchez, A.; Abbet, S.; Schneider, W.-D. *Eur. Phys. D* **1999**, *9*, 35–39.

[175] Landman, U.; Yoon, B.; Zhang, C.; Heiz, U.; Arenz, M. *Topics in Catalysis* **2007**, *44*, 145–158.

[176] Wang, J.; Wang, G.; Zhao, J. *Phys. Rev. B* **2002**, *66*(3), 035418.

[177] Dong, Y.; Springborg, M. *Eur. Phys. D.* **2007**, *43*, 15–18.

[178] Hakkinen, H.; Abbet, S.; Sanchez, A.; Heiz, U.; Landman, U. *Angew. Chem. Int. Ed.* **2003**, *42*, 1297–1300.

[179] Majumder, C.; Kandalam, A. K.; Jena, P. *Phys. Rev. B* **2006**, *74*, 205437.

[180] Bus, E.; van Bokhoven, J. A. *Phys. Chem. Chem. Phys.* **2007**, *9*, 2894–2902.

[181] Joshi, A. M.; Delgass, W. N.; Thomson, K. T. *J. Phys. Chem. B* **2006**, *110*, 23373–23387.

[182] Rao, J. L.; Chaitanya, G. K.; Basavaraja, S.; Bhanuprakash, K.; Venkataramana, A. *J. Mol. Struct: THEOCHEM* **2007**, *803*, 89–93.

[183] Tian, W. Q.; Ge, M.; Gu, F.; Yamada, T.; Aoki, Y. *J. Phys. Chem. A* **2006**, *110*, 6285–6293.

[184] Luo, C.; Zhou, C.; Wu, J.; Kumar, T. J. D.; Balakrishnan, N.; Forrey, R. C.; Cheng, H. *Int. J. Quant. Chem.* **2007**, *107*, 1632–1641.

[185] Moseler, M.; Hakkinen, H.; Barnett, R. N.; Landman, U. *Phys. Rev. Lett.* **2001**, *86*, 2545–2548.

[186] Kumar, V.; Kawazoe, Y. *Phys. Rev. B* **2002**, *65*, 125403.

[187] Bae, Y.-C.; Osanai, H.; Kumar, V.; Kawazoe, Y. *Phys. Rev. B* **2004**, *70*, 195413.

[188] Chen, J.; Tan, K.; Lin, M.-H.; Zhang, Q.-E. *Huaxue Xuebao* **2005**, *63*, 1957–1961.

[189] Bera, P. P.; Schleyer, P. v. R.; Schaefer III, H. F. *Int. J. Quant. Chem.* **2007**, *107*, 2220–2223.

[190] Häkkinen, H.; Landman, U. *Phys. Rev. B* **2000**, *62*, R2287–R2290.

[191] Zhao, J.; Yang, J.; Hou, J. G. *Phys. Rev. B* **2003**, *67*, 085404.

[192] Zhai, H.-J.; Kiran, B.; Dai, B.; Li, J.; Wang, L.-S. *J. Am. Chem. Soc.* **2005**, *127*, 12098–12106.

[193] Fernández, E. M.; Ordejón, P.; Bálbas, L. C. *Chem. Phys. Lett.* **2005**, *408*, 252–257.

[194] Yoon, B.; Häkkinen, H.; Landman, U. *J. Phys. Chem. A* **2003**, *107*, 4066–4071.

[195] Häkkinen, H.; Landman, U. *J. Am. Chem. Soc.* **2001**, *123*, 9704–9705.

[196] Socaciu, L. D.; Hagen, J.; Bernhardt, T. M.; Woste, L.; Heiz, U.; Häkkinen, H.; Landman, U. *J. Am. Chem. Soc.* **2003**, *125*, 10437–10445.

[197] Wallace, W. T.; Whetten, R. L. *J. Am. Chem. Soc.* **2002**, *124*, 7499–7505.

[198] Zwier, T. S. *J. Phys. Chem. A* **2001**, *105*, 8827–8839.

[199] Hunig, I.; Kleinermanns, K. *Phys. Chem. Chem. Phys.* **2004**, *6*, 2650–2658.

[200] Andrews, L.; Zhou, M. *J. Phys. Chem. A* **1999**, *103*, 7773–7784.

[201] Andrews, L.; Zhou, M. *J. Phys. Chem. A* **1999**, *103*, 5259–5268.

[202] Andrews, L.; Zhou, M.; Jr., C. W. B. *Chem. Rev.* **2001**, *101*, 1931–1961.

[203] Wu, Z.; Li, H.; Zhang, H.; Meng, J. *J. Phys. Chem. A* **2004**, *108*(49), 10906–10910.

[204] Broden, G.; Rhodin, T. N.; Brucker, C. *Surf. Sci.* **1976**, *59*, 593–611.

[205] Addicoat, M. A.; Buntine, M. A.; Yates, B.; Metha, G. F. *J. Comput. Chem.* **2008**, *29*, 1497–1506.

[206] Janssens, E.; Tanaka, H.; Neukermans, S.; Silverans, R. E.; Lievens, P. *Phys. Rev. B* **2004**, *69*, 085402.

[207] Tanaka, H.; Neukermans, S.; Janssens, E.; Silverans, R.; Lievens, P. *J. Am. Chem. Soc.* **2003**, *125*, 2862–2863.

[208] Koyasua, K.; Mitsuia, M.; Nakajima, A.; Kaya, K. *Chem. Phys. Lett.* **2002**, *358*, 224–230.

[209] Li, X.; Kiran, B.; Cui, L.-F.; Wang, L.-S. *Phys. Rev. Lett.* **2005**, *95*, 253401.

[210] Sahu, B. R.; Maofa, G.; Kleinman, L. *Phys. Rev. B* **2003**, *67*, 115420.

[211] Torres, M. B.; Fernandez, E. M.; Balbas, L. C. *Phys. Rev. B* **2005**, *71*(15), 155412.

[212] Yuan, D. W.; Wang, Y.; Zeng, Z. *J. Chem. Phys.* **2005**, *122*(11), 114310.

[213] Torres, M. B.; Fernndez, E. M.; Balbs, L. C. *Phys. Stat. Sol. B* **2005**, *242*, 819–821.

[214] Nonose, S.; Sone, Y.; Onodera, K.; Sudo, S.; Kaya, K. *Chem. Phys. Lett* **1989**, *164*, 427–432.

[215] Hakkinen, H.; Abbet, S.; Sanchez, A.; Heiz, U.; Landman, U. *Angew. Chem.* **2003**, *42*, 1297–1300.

[216] Pavão, A. C.; Soto, M. M.; Lester, W. A.; Lie, S. K.; Hammond, B. L.; Taft, C. A. *Phys. Rev. B* **1994**, *50*, 1868–1873.

[217] Swart, I.; Fielicke, A.; Redlich, B.; Meijer, G.; Weckhuysen, B. M.; de Groot, F. M. F. *J. Am. Chem. Soc* **2007**, *129*, 2516–2520.

[218] Goodwin, L.; Salahub, D. R. *Phys. Rev. A* **1993**, *47*, R774–R777.

[219] Addicoat, M. A.; Metha, G. F. *J. Comput. Chem.* **2008**, *Early View*.

[220] K. P. Huber, G. H., Ed. *Constants of Diatomic Molecules;* Van Nostrand Reinhold: New York, 1979.

[221] Kietzmann, H.; Morenzin, J.; Bechthold, P. S.; Ganteför, G.; Eberhardt, W.; Yang, D.-S.; Hackett, P. A.; Fournier, R.; Pang, T.; Chen, C. *Phys. Rev. Lett.* **1996**, *77*, 4528.